On the dynamics of thermohaline circulation based on the expansion in terms of diffusive vertical modes

(拡散鉛直モード展開に基づく海洋熱塩循環の力学)

上 原 克 人

On the dynamics of thermohaline circulation based on the expansion in terms of diffusive vertical modes

A dissertation submitted for the degree of Doctor of Science

BY

Katsuto Uehara

February 24, 1995

Abstract

Ocean thermohaline circulation is essentially three-dimensional motion of sea water. This feature has long prevented oceanographers from understanding the dynamics of thermohaline circulation well. This difficulty can be partly bypassed by expanding the circulation field in terms of *diffusive* vertical modes, which are characterized by the terms representing the horizontal and vertical diffusion of density. The thesis is intended to present this new perspective of ocean thermohaline circulation, where simplest situations are preferred in order to concentrate our effort on fundamental dynamics.

After a general introduction in the first chapter, the second chapter investigates the dynamics of the *diffusive* reduced-gravity model, a single-mode version of the multi-mode model discussed in the third chapter. As a model for the gravest baroclinic mode, it is applied to abyssal circulations driven by a prescribed supply of deep water. It is confirmed that the circulations follow the Stommel-Arons pattern as a whole. The introduction of horizontal diffusion, however, turns out to change the structure of boundary layers so radically that even downwelling is possible in boundary layers either near the western boundary or in the internal region. It is shown that, only when horizontal diffusion is incorporated, the reduced-gravity model is capable of reproducing the complicated distribution of vertical velocity in the abyssal layer which has often been referred to in various three-dimensional experiments. The seemingly curious downwelling is explained well dynamically in terms of the notion of *diffusive* stretching proposed here.

In the third chapter the *diffusive* reduced-gravity model of the second chapter is generalized to a multi-mode model that is composed of a number of diffusive vertical modes. Detailed formulation is provided to the framework of the multi-mode model. Also a direct method is developed to obtain the steady solution of each mode numerically. The method turns out accurate and efficient compared with the ordinary procedure to achieve the steady solution by time integration.

Then the fourth chapter combines the dynamics of a single mode argued in the second chapter with the synthesis of multiple modes formulated in the third chapter. The three-dimensional structure of two examples of thermohaline circulations is investigated in detail. One is a circulation driven by surface cooling localized at the center of a basin. The other is a circulation driven by surface heating at low latitudes and cooling at high latitudes, a schematic thermal forcing of the real ocean. In both cases, the multi-mode synthesis reproduces well the thermohaline circulation realized in the ordinary multi-level experiments. Though complicated, the former circulation is shown to be understood quite well if we consider it as the synthesis of the responses of diffusive vertical modes to a concentrated surface cooling due to convection.

The second circulation, however, appears still more involved. Nevertheless it is understood well by resolving it into *component* circulations, each of which is driven by the thermal forcing in the region specified for the component. By virtue of this localization of forcing, any of the component circulations is explained as the synthesis of diffusive vertical modes. As a result, it is understood why the circulation in the second experiment resembles that in the southern or southeastern area in the first experiment.

The thesis concludes that diffusive vertical modes and their synthesis surely provide a perspective that could not be obtained *only* by the multi-level description; the dynamics of thermohaline circulation becomes quite comprehensive from the viewpoint of the multi-mode model.

Acknowledgments

I would like to thank Professor A. Masuda of the Research Institute for Applied Mechanics, Kyushu University, for his sincere guidance, discussion, and encouragement throughout the thesis. The thesis has been accomplished in cooperative research with Professor Masuda. I am much indebted to Professor T. Kusaba, Professor S. Imawaki, and Professor J.-H. Yoon of the Research Institute for Applied Mechanics, and Professor K. Taira, Professor M. Kawabe, and Mr. G. Mizuta of the Ocean Research Institute, University of Tokyo, for their stimulating discussion. Thanks are due to Mr. K. Marubayashi, Mr. M. Ishibashi, and Ms. A. Ikesue of the Research Institute for Applied Mechanics for drawing figures, arranging the computer environment, and preparing the draft, respectively.

Contents

Chapter 1

General Introduction

A concise summary of the thesis is given together with its backgrounds and purposes. First, the study of thermohaline circulation is oriented in the research of ocean general circulation and the earth's climate. Next a short overview is given of works that are intimately related with the contents of the thesis. The purposes and approaches of the thesis follow that review. Finally Chapters 2 to 4 are surveyed to show the constitution and principal results of the thesis,

1.1 THERMOHALINE CIRCULATION AS AN OCEAN GENERAL CIRCULATION

Ocean general circulation has long been a subject of highest importance not only in physical oceanography but also in the other fields of oceanography, because all the physical, chemical, or biological processes in the sea take place in this background of ocean general circulation. Moreover, importance of the scientific research into this field is increasing, as global environmental issues become serious. It is well recognized now that the long-term variability of climate is controlled by the general circulation of the ocean rather than by that of the atmosphere. In this context the social need to understand the behavior of the climate system of our aqua-planet adds a first-class priority to the research into the ocean general circulation.

Traditionally, the ocean general circulation has been classified into two categories: the wind-driven circulation prevalent in the surface layer and the thermohaline circulation dominant at depths. The latter circulation, however, is less familiar to us for several reasons. First of all, the deep circulation has been more difficult to study than the surface circulation. For instance, measurement itself is difficult at depths. It requires much effort to moor measurement instruments and to recover them safely in the deep ocean. The efficient means of probing the earth by electromagnetic waves is not available in the ocean interior, although a wide range of wavelengths of microwaves to visible light have come into active use for monitoring the ocean surface via satellites.

Second, the spatial scale of thermohaline circulation is tremendous both horizontally and vertically. Thermohaline circulation is indeed a global circulation, carrying sea water from surface to bottom, from the North Atlantic to the North Pacific via the Southern Ocean. Moreover, deep currents flow slowly and fluctuate with longer periods, while properties of deep water are spatially rather homogeneous. Accordingly careful and long-term measurement must be made to detect weak flows and slight change of water properties. The time scale of thermohaline circulation is as large as 1000 years, which is to be compared with 10 years at most for subtropical gyres of the wind-driven circulation, or 3–5 years for the tropical variability of the ocean coupled with the atmosphere called El Niño and the Southern Oscillation (Philander, 1990). In addition, human activities have been concerned with phenomena in the upper layer of the ocean such as wind waves, tides, surface currents, or sea surface temperature. It is reasonable that our interest has been oriented predominantly toward the wind-driven circulation in the surface layer.

Thermohaline circulation thus has been less understood, confronting us with much more and harder problems to be solved either observationally, experimentally, or theoretically. It must be noted, however, that thermohaline circulation has had a tight relation to the classical oceanographic problem of the formation and maintenance of various *water masses* distributed in the world ocean (Sverdrup et al., 1942). The census of water masses shows that deep cold water occupies about 75 % of the whole sea water in the ocean (Worthington, 1981). In addition, recent highlight from environmental issues makes the research into the thermohaline circulation a major target of global scientific projects such as WOCE (World Ocean Circulation Experiment). For example, thermohaline circulation is supposed to play a major role in redistributing heat to the atmosphere and ocean, moderating the climate of our planet. Evidence of various sorts suggests that the climate of the last ice age about 18,000 years ago had a weaker thermohaline circulation than the present interglacial climate (Berger et al., 1989). The subject of the present thesis is this category of circulation—thermohaline circulation, which is worthy of intensive and extensive study for its profound importance in the research of climate.

1.2 OVERVIEW OF RELATED STUDIES

The subject of the present thesis is the dynamics of thermohaline circulation as a synthesis of vertical diffusive modes, each of which forms a kind of reduced-gravity model. In association with the contents of the thesis, therefore, a brief review is given below on articles that are related with the reduced-gravity model or the expansion in terms of barotropic and baroclinic modes.

The classical model of Stommel and Arons (1960) has long been the only effective theory on the abyssal circulation for the world ocean. Recently, however, theoretical or numerical study

has begun to increase, presumably stimulated by observational progress and by increasing interest in the long-term variability of the earth environmental system. The most straightforward approach is to use a multi-level model based on the primitive equations (Holland, 1971; Cox and Bryan, 1984; Bryan, 1987; Suginohara and Fukasawa, 1988; Semtner and Chervin, 1992). These powerful models can and usually do incorporate almost all necessary elements of fluid mechanics. The dynamics, however, tends to be concealed behind the many complexities of computers. Another approach is to use a simplified model such as a reduced-gravity model, sometimes at the risk of oversimplification.

Talley (1979) introduced Newtonian cooling into the study of abyssal circulation of a homogeneous bottom layer. She also assumed Rayleigh drag, perhaps the simplest form of momentum dissipation. Kawase (1987) extended Talley's study to the case on an equatorial β-plane and investigated the set-up process in detail. Kubota and Ono (1992) carried out a numerical experiment of the abyssal circulation with particular interest in the Philippine Sea. They adopted the harmonic form of viscosity instead of Rayleigh drag; the former represents horizontal mixing, while the latter represents vertical mixing. In their simulations, the western boundary current assumes a flow accompanied by recirculation (Munk 1950).

In all the reduced-gravity models mentioned above, cooling (warming) was of Newtonian type, which corresponds to vertical diffusion, so that no horizontal mixing of mass was taken into account. Chapter 2 of the thesis is intended to analyze a model which incorporates horizontal mixing of the interface elevation. It is of much interest to study how horizontal mixing affects deep circulation, as a fundamental problem in geophysical fluid dynamics. Another motivation comes from the desire to understand the physics of ocean general circulation produced by numerical models. The numerically simulated ocean is governed by primitive equations with parametrized subgrid-scale processes, so that, *in principle*, it should be possible to trace what occurs in the model. In reality, however, the numerically generated ocean is another ocean, the complexity of which can hardly be overcome even when the model ocean is steady and laminar with no mesoscale eddies. Numerical modelers have raised questions why different experiments generate features some common and others different, arguing model-and-parameter sensitivity (Bryan, 1987; Collin de Verdière, 1989; Holland, 1989).

There is a need to interpret the numerically obtained result in addition to accomplishing a sophisticated numerical simulation. The reduced-gravity model is one such tool for comprehension of the dynamics of ocean general circulation. We should remember, however, that no detailed investigation has been given even to the effect of horizontal viscosity in the previous studies based on a reduced-gravity model, though it was incorporated in the numerical experiments of Kubota and Ono (1992). It is necessary to study especially the role of diffusion of mass in addition to horizontal viscosity, in order to relate the reduced-gravity model more

closely with three-dimensional numerical experiments.

Chapter 2 of the thesis introduces the *diffusive* reduced-gravity model characterized by interfacial diffusion. This model represents the gravest baroclinic mode. In this chapter it is shown that horizontal diffusion together with horizontal viscosity causes a considerable change in the boundary layer structure and the vertical velocity field, which has been overlooked in the studies mentioned above. In particular, the diffusive reduced-gravity model is capable of explaining the seemingly curious distribution of downwelling found in various numerical simulations based on the primitive equations. Since the vertical velocity is of crucial importance both to ocean dynamics and to tracer distributions, it is to be emphasized that the diffusive reduced-gravity model reproduces the vertical motion in accord with elaborate numerical simulations.

As regard to the horizontal mixing, we should note that it has been incorporated in multilevel numerical models, and that it was considered by Warren (1976) in his study on the abyssal broad western boundary current in the South Pacific. He disregarded vertical mixing, however, and did not discuss the interior or the eastern flow at all. His analysis was confined only to the *local* structure of the western boundary. We may say that the diffusive reduced-gravity model is partly an extension of Talley (1979) or others with respect to Newtonian cooling and the global investigation and partly an extension of Warren (1976) with respect to horizontal mixing. As will be shown in the second chapter, the whole set of diffusive parameters are useful to discuss the deep circulations observed in various numerical experiments.

The diffusive reduced-gravity model, however, represents only a single mode, so that the circulation within that model cannot have a vertical structure other than that of the first baroclinic mode. It is the synthesis of many vertical modes that enables us to approach the three-dimensional distribution of circulation. Therefore we now refer to articles that concern how the circulation field is expanded in terms of vertical modes.

Thermohaline circulation is an essentially three-dimensional feature. It is a global convection, in which water sinks down to depths in restricted polar regions, moves along deep western boundary layers, and spreads toward the interior ocean, upwelling to the upper layer. This three-dimensional nature makes it difficult to understand the mechanism that maintains the thermohaline circulation of the ocean. One way to bypass that difficulty is to reduce the number of the space coordinates by expanding the field variables in terms of vertical modes, the lowest of which is called the barotropic mode (0th mode) and the others are called as baroclinic modes (nth mode, $n > 0$). In this sense, a number of oceanographic researches have so far been concerned with vertical modes relevant to long gravity waves (Krauss, 1966; Mork, 1972; McCreary, 1981; Wajsowicz and Gill, 1986; Pedlosky, 1992). In particular, the monograph of Gill (1982) seems to prefer the method of vertical-mode expansion in studying the adjustment

process of the ocean.

So far as we know, however, few oceanographic works have concerned vertical modes (especially modes with diffusive effects included) in studying the steady thermohaline circulation; most have dealt with the wave-mechanical response. Chapter 3 of the thesis therefore gives details about the expansion in terms of *diffusive* vertical modes with focus on slow dissipative dynamics of stratified oceans: the governing equations of each diffusive vertical mode, the boundary conditions including the surface thermal and mechanical forcing, and the transformation of physical variables to modal variables and *vice versa*. The resulting model is called as a multi-mode model, since it is composed of a number of vertical modes. This terminology is used to distinguish the model from the ordinary multi-level model (based on the level formulation) or from the diffusive reduced-gravity model (for a single mode).

1.3 PURPOSE OF THE THESIS

We nowadays see a flooding increase in observational studies based on hydrographic stations, mooring systems, and neutral buoys, prompted by various world-wide projects for climate research. Hydrographic reports of various sites are being published, revealing finer structure and providing more reliable information of deep circulation. Also there have been published a great many number of papers based on three-dimensional numerical experiments, supported by the advance of numerical techniques and electronic computers. Numerical codes of ocean general circulation at various research institutes are producing a vast amount of computer outputs on currents and water properties (e.g., Cox and Bryan, 1984; Bryan, 1987; Suginohara and Aoki, 1991; Semtner and Chervin, 1992; England, 1993). There is a diversity in resolution, accuracy, or target oceans. There is a diversity of experimental purpose as well: parameter sensitivity, multiple solutions of thermohaline circulation, evolution of deep circulation, simulation of deep circulation in a specified basin, simulation of the formation of various water masses, and so on. Even at this moment numerical models are being evolved. Some researchers are inclined to OGCMs with smaller grid sizes that can resolve oceanic finer mesoscale eddies (Bönig and Budich, 1992; Semtner and Chervin, 1992); some devise sigma or isopycnal coordinates to suppress unrealistic numerical effects of topography or to represent better dynamical processes near the thermocline (Haidvogel et al., 1991; Gerdes, 1993) ; and others attempt different parameterization of subgrid scales including a biharmonic form of viscosity or isopycnal mixing to reproduce well the observed distribution of salinity (Wolff et al., 1991; England, 1993). Also various subjects of papers are being published in recent journals, concerning some novel aspects of ocean thermohaline circulation: multiple steady states and their alteration in the glacial cycle (Stommel, 1961; Broecker, et al., 1988; Manabe and Stouffer, 1988; Power and Kleeman, 1993), interdecadal oscillation of circulation patterns (Weaver and Sarachik, 1991; Delworth, et

al., 1993; Greatbatch and Zhang, 1995), deep boundary currents near the equator (McCartney and Curry, 1993), hypsometric steering by topography (Rhines and MacCready, 1989; Ishizaki, 1994).

Despite those great progress achieved in order to know what the thermohaline circulation becomes like in each sophisticated situation of numerical modeling, however, our *understanding* of fundamental dynamics of thermohaline ocean general circulation remains rather poor and does not seem to have advanced much beyond that of Stommel and Arons (1960). Without understanding the fundamental dynamics of thermohaline circulation, it is impossible to anticipate or interpret what happens to the ocean thermohaline circulation for situations that have not been examined observationally or experimentally. Numerical experiments based on multi-level models compile up a formidable amount of numerical outputs, but they do not directly lead to the progress in either our understanding of the mechanism of thermohaline circulation or our ability to predict the variation of thermohaline circulation. It has been quite hard to understand even the steady thermohaline circulation free from mesoscale eddies. The three-dimensional structure of thermohaline circulation seems to refuse simple dynamical interpretation, if we rely upon only numerical simulations, which often lead to controversy and contradiction. It is necessary and desirable to study the dynamics in a simplified mathematical model in addition to realistic numerical experiments. In fact, box models have been applied successfully to oscillation and multiple steady states of thermohaline circulation (Stommel, 1961; Huang et al., 1992). Also abyssal circulation has often been argued well on reduced-gravity models (Kawase, 1987; Kubota and Ono, 1992).

With the context mentioned above, the thesis is intended to present a new perspective of ocean thermohaline circulation in order to clarify its complicated dynamics. For this purpose thermohaline circulation is expanded in terms of *diffusive* vertical modes. In this framework, thermohaline circulation is viewed in a kind of wavenumber space corresponding to the vertical axis, but still in physical space in the horizontal plane. Although such an approach has been made frequently so far in many other topics, most papers in oceanography have been related with wave mechanics or rapid response of the ocean. We therefore attempt an approach to thermohaline circulation on the basis of the expansion in terms of *diffusive* vertical modes, which are characterized by the diffusion of density, and which turn out quite useful in studying the slow or steady circulation of *stratified* oceans.

The stance or the basic principle of the thesis should be stated here. Our strategy is to advance step by step our knowledge and understanding of the complicated dynamics of thermohaline circulation. We do not intend to explain the whole dynamical aspects of thermohaline circulation at once in this thesis. Since our primary purpose is to understand the fundamental mechanism, we do not wish to reproduce every detailed feature of thermohaline circulation.

Rather, we simplify the situation as much as possible to concentrate our efforts on the essential mechanism that maintains the three-dimensional structure of thermohaline circulation. We disregard many realistic factors necessary to represent the observed thermohaline circulation, such as wind stress, meso-scale eddies, topography, the nonlinear equation of state, different surface conditions for temperature and salinity, and so on. Each of them is put aside not because it is insignificant, but because it is supposed less fundamental. It is worthwhile to ask how those complicating ingredients modify or alter the fundamental dynamics of thermohaline circulation investigated in our simplest sort of model. Those problems, however, are left for future research.

In any case, we always assume the Boussinesq approximation and hydrostatic balance. The salinity contribution to density is disregarded, so that temperature is identified with density. We consider a simplest geometry unless stated otherwise: a rectangular basin with a constant depth on a β-plane. Simple and typical distributions of cooling are exerted with no wind applied to the sea surface. We deal with steady thermohaline circulation, which allows no generation of mesoscale eddies by use of large viscosity and diffusivity.

It is to be noted that the approach based on the expansion in terms of vertical modes is not closed in itself. First, in order to determine the profile of each vertical mode, the basic stratification is specified or assumed as what is observed in the actual ocean or realized in numerical experiments. Also the forcing must be given to each vertical mode in order to calculate its response. This forcing, however, is contributed to by various terms such as convective adjustment, or nonlinear advection of density and momentum. These processes are beyond the scope of the linearized multi-mode model here, so that the exact forcing to each mode must be determined from the circulation of numerical experiments. That is, the method of the expansion in terms of vertical modes needs to be supplemented partly by data of the real circulation obtained from observation or experiment.

According to our principle, we put aside strong nonlinear processes such as the formation of deep water, which is supposed to occur in confined regions in the real ocean. We simply deal them as data or black boxes, unless the overall dynamics is sensitive to their details. It must be noted that, even for the other passive regions, there has been no satisfactory explanation about the mechanism that maintains the spatial structure of thermohaline circulation beyond the theory of Stommel and Arons (1960), who also disregarded the detailed process of deep water formation. It will be a great step therefore if we can understand the mechanism that maintains thermohaline circulation in the passive areas, which effectively occupy the whole ocean. In any case, detailed processes of deep water formation cannot be reliable, even on the multi-level model that is based on various physically doubtful assumptions such as convective adjustment, eddy diffusivity and viscosity, or the absence of variability like the baroclinic instability. It is thus reasonable to consider such processes as a kind of black box; necessary and reliable information

to the other passive areas is simply where and what amount of deep water is produced.

In this thesis we are content if we can understand how the thermohaline circulation is maintained in the passive areas. In this sense, our restricted purpose is to understand the dynamics of thermohaline circulation with those ambiguous processes provided as external conditions. It is the next step to clarify how purely external conditions determine the basic stratification, the forcing to each mode, the intensity or penetration depth of convective adjustment, and so on.

1.4 CONSTITUTION OF THE FOLLOWING CHAPTERS

The thesis substantially begins with Chapter 2, which introduces a *diffusive* reduced-gravity model, which takes into account horizontal diffusion of interfacial displacement in addition to Newtonian cooling. The model is shown later to be a single-mode version of the multi-mode model of diffusive vertical modes discussed in Chapter 3. It represents the first baroclinic mode or the overall circulation at depths. The model is applied to two situations of abyssal circulations driven by a prescribed supply of deep water. The horizontal diffusion and viscosity included in this model turn out to change the structure of boundary layers and the field of vertical velocity both on f- and β-planes. The dynamics of western boundary layers is classified into the *viscous* and *diffusive* regimes. In either regime, horizontal diffusion dominates the distribution of vertical velocity. Downwelling prevails in the western offshore boundary current flowing equatorward, while upwelling is always found in the poleward current. A more intense, opposite vertical motion occurs in a narrower boundary layer adjacent to the western coast. Downwelling is often distributed in a broad interior region, where horizontal diffusion again plays a crucial role in determining both horizontal and vertical velocities. The present model explains this downwelling in terms of *diffusive* stretching or the diffusion of the thickness term in potential vorticity. It is shown that, only when the horizontal diffusion is incorporated, the reduced-gravity model is capable of reproducing the complicated distribution of vertical velocity in the abyssal layer which has been repeatedly reported in various three-dimensional experiments.

Chapter 3 is devoted to the methodology of the thesis. Generalizing the diffusive reduced-gravity model in Chapter 2, Chapter 3 develops a multi-mode model (MMM) that is composed of a number of diffusive vertical modes. First, the three-dimensional field of ocean general circulation is shown to be expanded in terms of diffusive vertical modes. Then, a direct method of solution is developed to obtain the steady state of each mode numerically. The direct method turns out accurate and efficient compared with the conventional procedure to achieve the steady state by time integration, through application to the calculation of the first mode of thermohaline circulation in an idealized ocean similar to the Pacific. The same thermohaline circulation

is used also to illustrate how the multi-mode model synthesizes multiple vertical modes to construct the three-dimensional field and how it is interpreted as the synthesis of multiple diffusive modes.

Finally in Chapter 4, the three-dimensional structure of thermohaline circulations in two idealized situations is investigated with the multi-mode model prepared in Chapter 3 combined with the dynamics of a single mode discussed in Chapter 2. The modes calculated by the direct method are synthesized to yield the steady circulation to be compared with that achieved through time-integration with an ordinary multi-level model (MLM).

In the first experiment the ocean is driven by surface cooling localized near the center of the basin. The circulation realized by the MLM turned out to be reproduced well by the MMM synthesis where the response of modes is calculated to a simplified cooling *modeled* on convective adjustment. Moreover the response of each diffusive mode is explained well in terms of the dynamics of a single mode in Chapter 2. Thus, the three-dimensional structure of the circulation is understood as a composite of such diffusive vertical modes. The second circulation examined is driven by meridional differential cooling over the whole sea surface, yielding such a complicated three-dimensional field that simple decomposition into diffusive modes is of little use for dynamical interpretation. Nevertheless the result is understood well by resolving the circulation into component circulations each of which is driven by the thermal forcing in the region specified for the component: atmosphere-cooled convection in the northern basin, boundary-forced downwelling along the eastern boundary, and upwelling and downwelling along and near the western boundary. By virtue of the localization of the forcing, each component circulation is still explained as the synthesis of diffusive modes as well as in the first experiment. In particular, the MLM experiment is shown in good agreement with the MMM synthesis of the response to the distributed cooling near and along the northern boundary, where active convection takes place and boundary-forced sinking prevails. Thus, the circulation in the second experiment resembles that in the southern or southeastern basin in the first experiment.

At the end of the thesis, concluding remarks are added to describe the relations among the chapters more clearly by summarizing Chapters 2 to 4. Associated problems that are left for future are discussed also though briefly.

REFERENCES

Berger, A., S. Schneider, and J. Cl. Duplessy, 1989: Climate and Geo-Sciences: A Challenge for Science and Society in the 21st century. Kluwer Academic Publishers, 724pp.

Bleck, R. and D. B. Boudra, 1990: A Wind-Driven Isopycnic Coordinate Model of the North and Equatorial Atlantic Ocean 1. Model Development and Supporting Experiments. *J. Geophys. Res.*, **95**, 3273–3286.

Bönig, C. W. and R. G. Budich, 1992: Eddy Dynamics in a Primitive Equation Model: Sensitivity to Horizontal Resolution and Friction. *J. Phys. Oceanogr.*, **22**, 361–381.

Broecker, W. S., M. Andreae, W. Wolfli, H. Oescher, G. Bonani, J. Kennett, and D. Pettet, 1988: The chronology of the last deglaciation: Implications to the cause of the Younger Dryas event. *Paleoceanography*, **3**, 1–19.

Bryan, F. O., 1987: Parameter sensitivity of primitive equation ocean general circulation models. *J. Phys. Oceanogr.*, **17**, 970–985.

Collin de Verdière, A., 1989: On the interaction of wind and buoyancy driven gyres. *J. Marine Res.*, **47**, 595–633.

Cox, M. D. and K. Bryan, 1984: A numerical model of the ventilated thermocline. *J. Phys. Oceanogr.*, **14**, 674–687.

Delworth, T., S. Manabe, and R. J. Stouffer, 1993: Interdecadal Variations of the Thermohaline Circulation in a Coupled Ocean-Atmosphere Model. *J. Climate*, **6**, 1993–2011.

England, M. H., 1993: Representing the global-scale water masses in the ocean general circulation model. *J. Phys. Oceanogr.*, **23**, 1525–1552.

Gerdes, R., 1993: A Primitive Equation Ocean Circulation Model Using a General Vertical Coordinate Transformation 1. Description and Testing of the Model. *J. Geophys. Res.*, **98**, 14683–14701.

Gill, A. E., 1982: Atmosphere-Ocean Dynamics. Academic Press, 662pp.

Greatbatch, R. J. and S. Zhang, 1995: An Interdecadal Oscillation in an Idealized Ocean Basin Forced by Constant Heat Flux. *J. Climate*, **8**, 81–91.

Haidvogel, D. B., J. L. Wilkin, and R. E. Young, 1991: A semispectral primitive equation ocean circulation model using vertical sigma and orthogonal curvilinear horizontal coordinates. *J. Comput. Phys.*, **94**, 151–185.

Hirst, A. C., W. Cai, 1994: Sensitivity of a World Ocean GCM to Changes in Subsurface Mixing Parameterization. *J. Phys. Oceanogr.*, **24**, 1256–1279.

Holland, W. R., 1971: Ocean tracer distributions. Part I. A preliminary numerical experiment. *Tellus*, **23**, 371–392.

Holland, W. R., 1989: Experiences with various parametrizations of sub-grid scale dissipation and diffusion in numerical models of ocean circulation. In: *Parametrization of small-scale processes*, P. Müller and D. Henderson, eds., Hawaii Institute of Geophysics Special Publication 1989, 1–9.

Huang, R. X., Luyten, J. R. and Stommel, H., 1992: Multiple equilibrium states in combined thermal and saline circulation. *J. Phys. Oceanogr.*, **22**, 231–246.

Ishizaki, H., 1994: A Simulation of the Abyssal Circulation in the North Pacific Ocean. Part II: Theoretical rationale. *J. Phys. Oceanogr.*, **24**, 1941–1954.

Kawase, M., 1987: Establishment of mass-driven abyssal circulation. *J. Phys. Oceanogr.*, **17**, 2294–2317.

Kubota, M. and H. Ono, 1992: Abyssal circulation model of the Philippine Sea. *Deep-Sea Res.*, **39**, 1439–1452.

Krauss, W., 1966: Interne Wellen. Methoden und Ergebnisse der Theroetischen Ozeanographie, Band II. Gebrüder Borntraeger, 248pp.

Manabe, S. and R. J. Stouffer, 1988: Two Stable Equilibria of a Coupled Ocean-Atmosphere Model. *J. Climate* , **1**, 841–866.

McCartney, M. S. and R. C. Curry, 1993: Transequatorial flow of Antarctic Bottom Water in the Western Atlantic Ocean: Abyssal geostrophy at the equator. *J. Phys. Oceanogr*, **23**, 1264–1276.

McCreary, J. P., 1981: A linear stratified model of the Equatorial Undercurrent. *Phil. Trans. R. Soc. Lond.*, **A298**, 603–635.

Mork, M., 1972: On the time-dependent motion induced by wind and atmospheric pressure in a continuously stratified ocean of varying depth. Geophys. Inst., Div. A, Phys. Oceanogr., Univ. of Bergen, 43pp.

Munk, W. H., 1950: On the wind-driven ocean circulation. *J. Meteorol.*, **7**, 79–93.

Pedlosky, J., 1992: The Baroclinic Structure of the Abyssal Circulation. *J. Phys. Oceanogr.*, **22**, 652–659.

Philander, S. G., 1990: El Niño, La Niña, and the Southern Oscillation. Academic Press, 283pp.

Power, S. B. and R. Kleeman, 1993: Multiple Equilibria in a Global Ocean Circulation Model. *J. Phys. Oceanogr.*, **23**, 1670–1681.

Rhines, P. B. and P. M. MacCready, 1989: Boundary control over the large-scale circulation. In: *Parametrization of small-scale processes*, P. Müller and D. Henderson, eds., Hawaii Institute of Geophysics Special Publication 1989, 75–99.

Semtner, A. J., Jr. and R. M. Chervin, 1992: Ocean general circulation from a global eddy-resolving model. *J. Geophys. Res.*, **97**(C), 5493–5550.

Stommel, H., 1961: Thermohaline convection with two stable regimes of flow. *Tellus*, **13**, 224–230.

Stommel, H. and A. B. Arons, 1960: On the abyssal circulation of a world ocean—II. An idealized model of the circulation pattern and amplitude in oceanic basins. *Deep-Sea Res.*, **6**, 217–244.

Suginohara, N. and S. Aoki, 1991: Buoyancy-driven circulation as horizontal convection on β-plane. *J. Marine Res.*, **49**, 295–320.

Suginohara, N. and M. Fukasawa, 1988: Set-up of deep circulation in multilevel numerical models. *J. Oceanogr. Soc. Japan*, **44**, 315–336.

Sverdrup, H. U., M. W. Johnson, and R. H. Fleming, 1942: The Oceans: Their Physics, Chemistry, and General Biology. Prentice-Hall, 1087pp.

Talley, L., 1979: Steady two-layer source-sink flow. *1979 summer Study Program in Geophysical Fluid Dynamics at the Woods Hole Oceanographic Institution: Notes on Polar Oceanography,* Vol. 2, Woods Hole Oceanographic Institution, 97–118.

Wajsowicz, R. C., and A. E. Gill, 1986: Adjustment of the Ocean under Buoyancy Forces. Part I: The Role of Kelvin Waves. *J. Phys. Oceanogr.*, **16**, 2097–2114.

Warren, B. A., 1976: Structure of deep western boundary currents. *Deep-Sea Res.*, **23**, 129–142.

Weaver, A. J. and E. S. Sarachik, 1991: The role of mixed boundary conditions in numerical models of the ocean's climate. *J. Phys. Oceanogr.*, **21**, 1470–1493.

Wolff, J. -O., E. Maier-Reimer, and D. J. Olbers, 1991: Wind-Driven Flow over Topography in a Zonal β-Plane Channel: A Quasi-geostrophic Model of the Antarctic Circumpolar Current. *J. Phys. Oceanogr.*, **21**, 236–264.

Worthington, L. V., 1981: The deep water masses of the World Ocean: Some results of a fine-scale census. Evolution of Physical Oceanography, B. A. Warren and C. Wunsch eds., MIT Press, 42–49.

Chapter 2

A reduced-gravity model of the abyssal circulation with Newtonian cooling and horizontal diffusion

Abstract

Steady abyssal circulation is investigated with a simple model called a *diffusive* reduced-gravity model where horizontal diffusion of interfacial displacement is taken into account in addition to ordinary vertical diffusion of Newtonian cooling. The horizontal diffusion and viscosity included in this model turn out to change the structure of boundary layers and the field of vertical velocity both on f- and β-planes. The dynamics of western boundary layers is classified into the viscous and diffusive regimes. In either regime, horizontal diffusion dominates the distribution of vertical velocity. Downwelling prevails in the western offshore boundary current flowing equatorward, while upwelling is always found in the poleward current. A more intense, opposite vertical motion occurs in a narrower boundary layer adjacent to the western coast. Downwelling is often distributed in a broad interior region, where horizontal diffusion again plays a crucial role in determining both horizontal and vertical velocities. The present model explains this downwelling in terms of the diffusion of the thickness term in potential vorticity. It is shown that, only when the horizontal diffusion is incorporated, the reduced-gravity model is capable of reproducing the complicated distribution of vertical velocity in the abyssal layer which has been repeatedly reported in various three-dimensional experiments. The present model is also applicable to the surface layer, extending the Sverdrup-Stommel-Munk theory of the homogeneous ocean to that more suitable for the stratified ocean.

2.1 INTRODUCTION

Deep layers below thermocline suffer no direct effect of wind stress, so that they are believed to be driven primarily by the thermohaline forcing. A dynamical picture of deep circulation was presented by Stommel and Arons (1960). Applying the vorticity dynamics on a β plane, they showed that deep water must flow poleward in the interior region, if it upwells into the upper layer at a prescribed uniform rate.

Since then, remarkable progress has been achieved for thermohaline circulation both observationally and experimentally. The increasing data of hydrographic or current measurements have revealed more and more detailed distributions in the ocean (Bainbridge, 1981; Mantyla and Reid, 1983); observations have stimulated a deep interest in the three-dimensional structure of thermohaline circulation (Fiadeiro, 1982). At the same time another powerful means has become available. Numerical models for ocean general circulation have been developed to become an indispensable tool for oceanographers. Numerical experiments can give sufficient information on what occurs for thermohaline circulation simulated in a particular situation. Applied to various subjects of thermohaline circulation, they have proven their great ability to advance the study of thermohaline circulation. (Cox and Bryan, 1984; Bryan, 1987; Collin de Verdière, 1989; Suginohara and Aoki, 1991; England, 1993).

Nevertheless, even the most recent paper such as Toggweiler (1994) or Ishizaki (1994). still returns and refers to the classical theory of Stommel and Arons when arguing or interpreting the dynamics of thermohaline circulation. It is probably because there are no other available theory for the basic dynamics of abyssal circulation. It must be remembered that only by numerical experiments neither dynamical interpretation nor explanation can be obtained.

The model of Stommel and Arons (1960), however, is too limited to be useful for some advanced problems. For instance, how are the stacked water masses of different origins maintained in the Southern Atlantic? What is the structure of boundary layers expected along the western and northern boundary in Stommel and Arons (1960)? What mechanism is responsible for the strange downwelling found in the abyssal layer for the circulation realized in a lot of numerical multi-level experiments (Holland, 1971, Suginohara and Fukasawa, 1988)? Apparently, neither of them cannot be accessed to by the model of Stommel and Arons. We thus need further study with models of comprehensive dynamics, in order to answer those questions.

Among such simple models as are required is a reduced-gravity model with Newtonian cooling. Talley (1979) first introduced this model into the study of thermohaline circulation. By virtue of Newtonian cooling, she could determine the rate of upwelling, which had to be prescribed in Stommel and Arons (1960). In addition the Rayleigh drag is included in the balance of momentum to close the circulation in the western boundary layer. Using the same model,

Kawase (1987) examined the set-up process of the abyssal circulation in detail. Kubota and Ono (1992) investigated the abyssal circulation in the Philippine Sea with a similar model that has a harmonic form of viscosity instead of the Rayleigh drag. The success of the above models is due to Newtonian cooling as a substitute for the vertical diffusion of density. None of them, however, has investigated the model with horizontal mixing of density. Though Warren (1976) argued the effect of horizontal diffusion, his analysis was restricted to the western boundary layer and the vertical mixing was not considered at all.

In this chapter, the dynamics of the abyssal circulation is investigated with a reduced-gravity model with Newtonian cooling and horizontal diffusion incorporated. An emphasis is put on examining how the circulation is altered by the addition of horizontal diffusion to the other dissipative mechanisms. It will be shown later that horizontal diffusion plays an essential role in producing the strange distribution of upwelling and downwelling which has been reported often in multi-level numerical experiments.

The next section describes the formulation of the model. In the third section, the model with and without horizontal diffusion is applied to abyssal circulations driven by a prescribed supply of deep water. The circulations obtained numerically with this model are compared with those by similar studies based on multi-level experiments. Detailed analysis of the steady state follows in the fourth section, where the structure of boundary layers and the presence of downwelling regions are explained dynamically well in terms of *diffusive* stretching. A summary and discussion are given in the final section.

2.2 FORMULATION

Our purpose is to provide a simple model by which to obtain insight into the fundamental dynamics of abyssal circulations. We therefore ignore various important realities such as topography, vertical density profiles, nonlinearity, and detailed mechanisms of sinking or inflow. Let us start from the linearized equations of motion for a bottom homogeneous layer of uniform depth H:

$$\frac{\partial u}{\partial t} - fv = -g'\frac{\partial \eta}{\partial x} - Ru + \nu\nabla^2 u \tag{2.1}$$

$$\frac{\partial v}{\partial t} + fu = -g'\frac{\partial \eta}{\partial y} - Rv + \nu\nabla^2 v \tag{2.2}$$

$$\frac{\partial \eta}{\partial t} + H\left\{\frac{\partial u}{\partial x} + \frac{\partial v}{\partial y}\right\} = -\lambda\eta + \kappa\nabla^2\eta + Q \tag{2.3}$$

where t is time, (x, y) are the (eastward, northward) coordinates, (u, v) the corresponding velocities, f the Coriolis parameter, g' the reduced gravity due to the small density difference between the bottom and the upper inactive layer, η the interfacial displacement of the bottom

layer, and Q the rate of external mass addition. Here R denotes the coefficient of Rayleigh drag and λ the coefficient of Newtonian cooling (warming). It is to be noted that the Newtonian cooling is needed in our model for maintaining steady state by absorbing the water supplied from the outer ocean or by the upper layer. Our model is identical with the model of Talley (1979) or Kawase (1987) if ν and κ are neglected; it is identical with the model of Kubota and Ono (1992), when R and κ are dropped.

A somewhat curious expression for the upwelling velocity w_u at the interface follows from (2.3):

$$\begin{aligned} w_u = H\left(\frac{\partial w}{\partial z}\right) &= -H\left(\frac{\partial u}{\partial x} + \frac{\partial v}{\partial y}\right) \\ &= \lambda\eta - \kappa\nabla^2\eta + (-Q) \end{aligned} \tag{2.4}$$

for steady state. If horizontal mixing κ is not incorporated, w_u is proportional to η and consequently to the perturbation pressure $p = g'\eta$.

The equations (2.1)–(2.3) must be supplemented by adequate boundary conditions. Talley (1979) and Kawase (1987) needed zero normal velocity only, since they discarded the horizontal viscosity ν and diffusion κ. Using the horizontal viscosity, Kubota and Ono (1992) put an additional condition of no tangential velocity. On the other hand, our model contains a Laplacian term for (2.3), which needs two more conditions for η. We require its normal derivative to vanish at each lateral boundary, which is equivalent to no mass-flux condition.

There are two dissipative terms on the right hand side of the continuity equation (2.3), which may appear strange at a glance. The first of them was discussed already by Talley (1979) and Kawase (1987) as a substitute for the interfacial mixing. One might feel less familiar with the second term (horizontal diffusion of the interfacial displacement), which is introduced in the present model. It is an extension of the notion of the Newtonian cooling (diapycnal mixing), and in fact, is interpreted as the horizontal mixing of mass (isopycnal mixing). A cursory derivation of (2.3) is given below, in a manner similar to McCreary (1981) or Kawase (1987).

Consider the linearized equations of motion for a continuously stratified ocean:

$$\frac{\partial u}{\partial t} - fv = -\frac{1}{\rho_0}\frac{\partial p}{\partial x} + \nu_V\frac{\partial^2 u}{\partial z^2} + \nu_H\nabla^2 u \tag{2.5}$$

$$\frac{\partial v}{\partial t} + fu = -\frac{1}{\rho_0}\frac{\partial p}{\partial y} + \nu_V\frac{\partial^2 v}{\partial z^2} + \nu_H\nabla^2 v \tag{2.6}$$

$$0 = -\frac{1}{\rho_0}\frac{\partial p}{\partial z} - g\rho \tag{2.7}$$

$$\frac{\partial u}{\partial x} + \frac{\partial v}{\partial y} + \frac{\partial w}{\partial z} = 0 \tag{2.8}$$

$$\frac{\partial \rho}{\partial t} + \left(\frac{d\bar{\rho}_0}{dz}\right) w = \kappa_V \frac{\partial^2 \rho}{\partial z^2} + \kappa_H \nabla^2 \rho \tag{2.9}$$

where z denotes the vertical coordinate, $\bar{\rho}_0(z)$ the basic density field, ρ its perturbation, and suffixes V and H respectively indicate the values corresponding to the vertical and horizontal directions; the coefficients have been assumed constant. Let us show that the continuity equation (2.3) in the reduced-gravity model is a contracted expression of the three equations (2.7)–(2.9) in the continuous model, and thereby determine the boundary condition for η in (2.3).

It has been widely accepted that the reduced-gravity model represents a kind of first baroclinic mode. For simplicity of the analysis, let us assume the Boussinesq approximation and a uniform stratification; the realistic stratification does not alter the following result, if the vertical mixing depends on the static stability suitably as in McCreary (1981). Then the mth baroclinic mode has a vertical distribution

$$p \sim \cos\left(\frac{m\pi z}{D}\right) \tag{2.10}$$

where m is the vertical mode number and D the total depth. Eliminating w and ρ from (2.7)–(2.9), we have

$$\left(\frac{\partial u}{\partial x} + \frac{\partial v}{\partial y}\right) + \left(\frac{\partial}{\partial t} + \lambda_m - \kappa_H \nabla^2\right) \frac{p}{c_m^2 \rho_0} = 0 \tag{2.11}$$

where c_m is the phase velocity of the mth mode gravity waves and $\lambda_m = \kappa_V (m^2\pi^2)/D^2$. If c^2 and p/ρ_0 are replaced by $g'H$ and $g'\eta$, respectively, (2.11) turns out to be (2.3) except for slight differences in notation.

Since η is equivalent to the perturbation density in the sense mentioned above, we should require the normal derivative to vanish as the boundary condition for the interfacial displacement η. The vertical viscosity takes a form of the Rayleigh drag, for the specific baroclinic mode as well, of course. It is to be remarked that λ increases with the vertical mode number m as $\lambda \propto m^2$, while κ is independent of m.

Let us proceed with the above forms of dissipation without further discussion. It must be kept in mind, however, that all of these dissipative formulations are simply *assumed* both in their functional forms and in their coefficient values; justifiable parametrization for the turbulent mixing in the ocean is impossible at present. Note also that our model includes all the dissipative formalisms used in ordinary numerical experiments.

2.3 NUMERICAL RESULTS

The results in this section are designed partly in order to visualize typical abyssal circulation realized in our model and partly in order to make use of our model to interpret the

complicated abyssal field produced by three-dimensional numerical experiments. We will encounter phenomena which may appear curious at a glance. Their interpretation is postponed till the next section, so that this and the next sections are to be referred to each other.

Some parameter values used in the following may appear exaggerated for the real ocean. This is to see more clearly the effect of various parameters in concern. See the caption of each figure for detailed conditions.

2.3.1 *The Philippine Sea*

Little has been known about the abyssal circulation of the Philippine Sea, the bathymetry of which is shown in Fig.2.1. Although the classical model of Stommel and Arons (1960) is concerned with the world-wide deep circulation, it disregards the Philippine Sea as a marginal sea. Moreover the deep current in the Philippine Sea is difficult to infer from hydrographic data, since water properties are rather uniform there as is the case for the North Pacific. The Philippine Sea therefore has been a missing part of our knowledge on deep circulation. Observational progress, however, such as an extensive study of physical and chemical distribution (Kaneko, 1984; Uehara and Taira, 1990) or long-term current measurements (Fukasawa et al., 1986; Yoshioka et al., 1988) began to clarify the abyssal circulation in the Philippine Sea, though the present amount of data still are neither satisfactory nor conclusive. At the same time, a numerical simulation based on a reduced-gravity model was started by Kubota and Ono (1992) with focus on the Philippine Sea. The present investigation has also begun from an attempt to understand the basic physics of the deep circulation there.

We model the Philippine Sea as a square flat basin. It includes the Kyushu-Palau Ridge as a wall which has a break at about 18°N, in contrast with the model of Kubota and Ono (1992). The circulation is driven by an inflow through the Yap-Mariana Junction located at the southeast corner. Figure 2.2 shows the fields when κ is absent: (a) η together with (u, v), and (b) w_u in the model Philippine Sea. It is to be compared with Fig.2.3, where the conditions are the same except that horizontal diffusion $\kappa = 10^7 \mathrm{cm}^2\,\mathrm{s}^{-1}$. Both figures show the classical flow pattern of Stommel and Arons (1960). Also the Philippine Basin has an equatorward western boundary current without a stagnation point as was pointed out by Kubota and Ono (1992). A significant difference is observed in the distribution of vertical velocity w_u. We find much more complicated contours in Fig.2.3(b) than in Fig.2.2(b). In particular, the equatorward western boundary current is associated with downwelling. From the previous reduced-gravity models, one would expect upwelling everywhere. The equatorward western boundary current, however, is not inconsistent with the recent hydrographic data of Uehara and Taira (1990) along 12°N and 13°N in the Philippine Sea; the equatorward western boundary current is not so wide as their data suggested though, at least for the parameters chosen here. Another downwelling

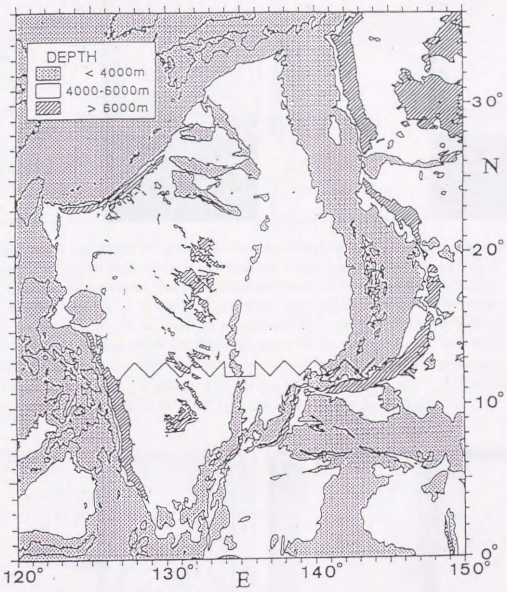

Fig.2.1 The bathymetry of the Philippine Sea cited from Uehara and Taira (1990).

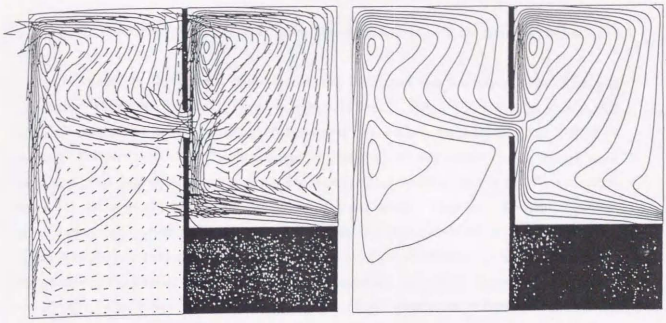

Fig.2.2 Abyssal field in the model Philippine Sea when horizontal diffusion κ is absent: (a) contours for the interfacial displacement η and vector arrows for horizontal velocities (u, v); (b) contours for vertical velocity w. The contour intervals are 6.0×10^1 cm and 4.0×10^{-6}cm$\cdot$s^{-1} for (a) and (b), respectively. Contours for extensively high and lower values will be omitted often in the following figures, to avoid too concentrated contours. The circulation is driven by the inflow through the gap at the southeast corner at the rate of volume transport of 1×10^6m$^3\cdot$s^{-1}. The zonal width $X = 2000$ km , meridional width $Y = 2000$ km, phase speed c due to the reduced-gravity $= 200\,\mathrm{cm}\cdot\mathrm{s}^{-1}$, $\nu = 1 \times 10^7\mathrm{cm}^2\mathrm{s}^{-1}$, $\kappa = 0\,\mathrm{cm}^2\mathrm{s}^{-1}$, $1/R = 100$ days, $1/\lambda = 200$ days, $\beta = 2.3 \times 10^{-13}\mathrm{cm}^{-1}\mathrm{s}^{-1}$, $\Delta x = 20$ km, and $\Delta y = 20$ km.

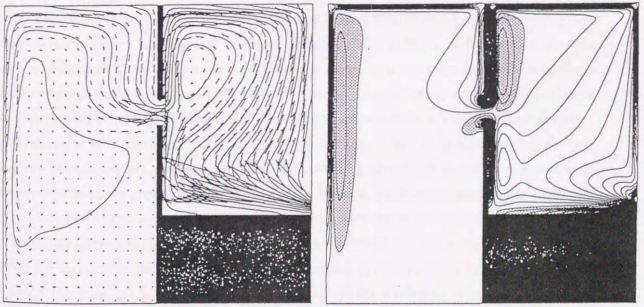

Fig.2.3 Abyssal field in the model Philippine Sea when $\kappa = 1 \times 10^7\mathrm{cm}^2\mathrm{s}^{-1}$. The contour intervals are 2.0×10^2 cm and 3.0×10^{-5}cm$\cdot$s^{-1} for (a) and (b), respectively. Dotted region indicates downwelling. See legend of Fig.2.2 for the other detailed conditions.

region lies in the narrow boundary layer where the current flows with the coast to the left-hand side.

According to the present crude model, the Philippine Sea has three gyres of abyssal circulation, while a previous study suggested one cell (Kaneko, 1984). The abyssal flow measured with moored-current meters at several stations near the northern boundaries of the Philippine Sea (e.g., Fukasawa et al., 1986) does not seem to disagree with the present model, though there remains a great deal of uncertainty. A similar measurement on a flat floor in the West Mariana Basin (Yoshioka et al,, 1988) does not agree with our result. Their measurement, however, shows large year-to-year variability of the *mean* abyssal flow (Yoshioka et al., 1990, private communication), so that we must wait for further conclusive observation. It is to be noted that our picture of the abyssal flow in the Philippine Sea totally depends on the model geometry of the Kyushu-Palau Ridge. The conclusion may be altered when more realistic simulations are carried out.

2.3.2 *The Pacific Ocean*

In relation to the strange distribution of downwelling in the model Philippine Sea, let us refer to an example from a numerical experiment which was carried out to study the purely thermohaline circulation in the Pacific by Suginohara and Fukasawa (1988). They simulated the set-up process to the steady state in the ocean which extends over both hemispheres. The body cooling near the southern boundary drives the ocean and no deep water is produced in the northern hemisphere.

Figure 2.4 cited from their paper shows the abyssal field of density, which roughly corresponds to pressure, and vertical velocity. Obviously the pressure and current follow the so-called Stommel-Arons pattern. A notable feature, though not very apparent in this figure, is the presence of the meandering of the eastward current near the equator. On the other hand, the distribution of vertical velocity differs from what one may expect from the classical theory. Although most of the interior is characterized by upwelling, downwelling is interwoven not only near the boundaries but also in the interior. We did not observe such a curious distribution in the previous reduced-gravity models (Talley, 1979; Kawase, 1987; Kubota and Ono, 1992).

Downwelling is not surprising within 500 km from the southern boundary, where the body cooling forces sinking. Why, however, does the downwelling occur over so broad an interior region tilting northwestward? What determines the area and shape of the interior downwelling region? Why does this downwelling region shrink back to the south near the western boundary? There is a strange sequence of upwelling and downwelling along the western boundary extending over both hemispheres. What determines the pattern and the scale? What is the mechanism of the meandering near the equator? Is it an equatorial analogue of the mid-latitude nonlinear

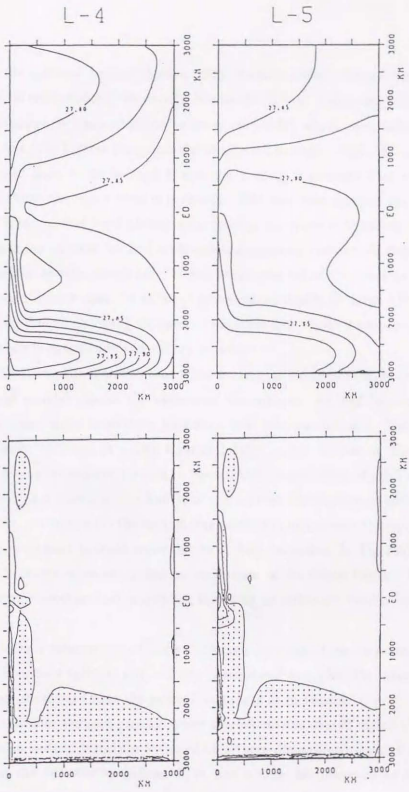

Fig.2.4 Abyssal field in the model Pacific Ocean driven by body cooling near the southern boundary, cited from Suginohara and Fukasawa (1988). Stronger cooling is assumed near the western corner and no wind stress is used in this three-dimensional experiment. The upper figures show contours of σ_t at the second lowest level (left) and the lowest level (right), while the lower figures contours of w at the corresponding levels. The dotted region indicates downwelling.

meandering of the eastward current (Moore, 1963; Masuda, 1989)? What is responsible for the intensified vertical motion along the eastern boundary? In which scale does this occur?

Let us examine the same situation by use of our model, where we substitute body cooling by mass addition to the bottom layer near the southern boundary. Note that zonally sinusoidal forcing is imposed here, while in Fig.2.4, stronger cooling is assumed near the southwestern corner. Fig.2.5 shows the result when κ is absent. The flow field assumes the Stommel-Arons pattern in the interior, and recirculation accompanies the western boundary current. In the western part near the equator, we find a meandering eastward current. As regards the vertical velocity, deep water upwells everywhere, as has been observed in the previous reduced-gravity models. We should remark that, for different parameters (usually for large $\lambda f^2/c^2$), water may downwell near the boundary owing to viscosity (Section 2.4). Even when downwelling occurs, however, it is weak in magnitude and narrow in area.

Figure 2.6 shows the opposite case when horizontal diffusion is large ($\kappa = 10^8 \mathrm{cm}^2\mathrm{s}^{-1}$). The current field remains almost the same near the equator. At high latitude, however, recirculation disappears and the western boundary layer becomes broader. This flow pattern is favorably compared with that in a deep layer of density driven circulation (Fig.2.7) cited from Bryan (1986), where the surface cooling in the northern part drives abyssal circulation. Reversing the meridional direction, we find that the current distribution is almost the same as ours. In particular, we notice (1) the meandering eastward current near the equator and (2) the western boundary current without recirculation at high latitudes. In Fig.2.6(b), downwelling appears along the western boundary and in the interior of the South Pacific. The distribution of vertical velocity resembles that in Fig.2.3, including an enhanced vertical motion along the eastern boundary.

For a moderate value of $\kappa = 10^7 \mathrm{cm}^2\mathrm{s}^{-1}$, though not shown here, recirculation is observed in the western boundary layer at any latitude. Associated with this, the interior downwelling region turns back southward near the western boundary as in Fig.2.4.

Thus the present reduced-gravity model reproduces the overall distribution of not only horizontal but also vertical velocities obtained by a three-dimensional simulation. It should be emphasized that the diffusive formalisms λ, κ, and ν must be incorporated for the reduced-gravity model to give the characteristic abyssal field mentioned above.

2.3.3 *Response to an isolated forcing*

In Figs.2.4 and 2.6, downwelling occurs in the interior South Pacific. To investigate the dynamics of the interior downwelling, let us cite Fig.2.8 from Holland (1971), where the wind forcing at the surface and the symmetry condition about the equator complicates the field somewhat. He had two features in common with Figs.2.4 and 2.6: (1) the equatorward western

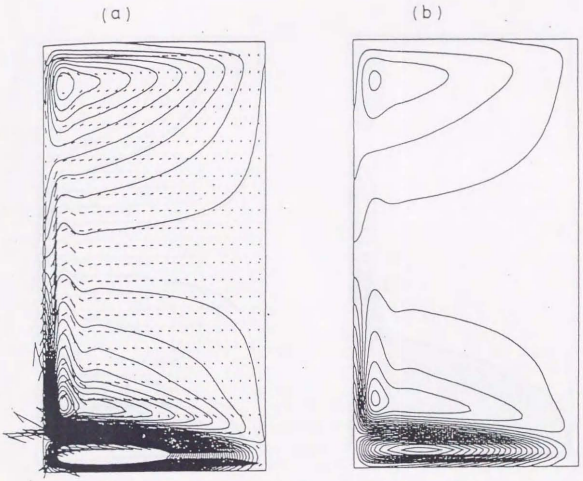

Fig.2.5 Abyssal field in the model Pacific Ocean when κ is absent, where mass is added to the deep layer near the southern boundary: (a) contours for interfacial displacement η and vector arrows for horizontal velocities (u, v); (b) contours for vertical velocity w. The contour intervals are 3.88×10^{1}cm and $5.82 \times 10^{-7}\mathrm{cm}^{-1}\mathrm{s}^{-1}$, for (a) and (b) respectively. The circulation is driven by mass addition of sinusoidal form near the southern boundary with the characteristic meridional scale 420 km and the characteristic zonal scale of the zonal width of the basin. The rate of mass addition is $1 \times 10^{6}\mathrm{m}^{3}\cdot\mathrm{s}^{-1}$. The zonal width $X = 3000$ km, meridional width $Y = 6000$ km, phase speed c due to the reduced-gravity$= 200\ \mathrm{cm}\cdot\mathrm{s}^{-1}$, $\nu = 1 \times 10^{8}\mathrm{cm}^{2}\mathrm{s}^{-1}$, $\kappa = 0\ \mathrm{cm}^{2}\mathrm{s}^{-1}$, $1/R = 100$ days, $1/\lambda = 2000$ days, $\beta = 2.3 \times 10^{-13}\mathrm{cm}^{-1}\mathrm{s}^{-1}$, $\triangle x = 30$ km, and $\triangle y = 60$ km.

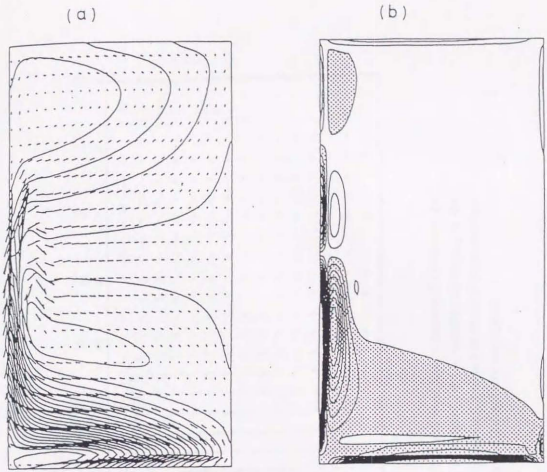

Fig.2.6 The same as Fig.2.5 except that $\kappa = 1 \times 10^{6} \mathrm{cm}^{2}\mathrm{s}^{-1}$. The contour intervals are 3.88×10^{1} cm and $1.16 \times 10^{-6} \mathrm{cm} \cdot \mathrm{s}^{-1}$ for (a) and (b), respectively. Dotted area indicates downwelling. See legend of Fig.2.5 for the other detailed conditions.

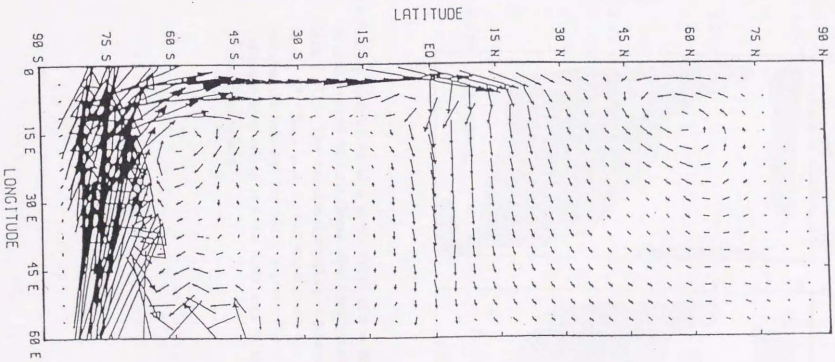

Fig.2.7 Abyssal current field in the model Atlantic Ocean cited from a numerical experiment by Bryan (1986). Though the original figure is designed for the situation of cooling in the northern hemishphere like the Atlantic, the meridional direction is reversed for comparison with the situation of the Pacific that is cooled in the southern hemisphere.

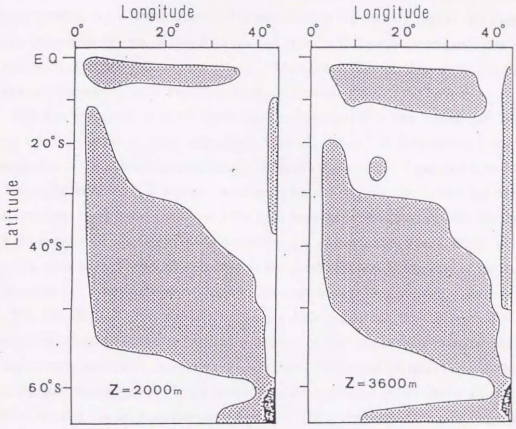

Fig.2.8 Deep distribution of w at the depth of $z = 2000$ m (left) and $z = 3600$ m in the model Atlantic Ocean cited from a numerical experiment by Holland (1971). The meridional direction is reversed for the same reason as in Fig.2.7. Note that, in this experiment, the realistic wind-stress complicates the field and symmetry is posed about the equator. Dotted area indicates downwelling and the black area at the southeast corner shows intense downwelling.

boundary current composed of offshore downwelling and inshore upwelling sublayers, and (2) the broad interior region extending northwestward from the sinking region. Of course, there are some differences between Holland's work and ours. In Holland's experiment, sinking occurs in a confined region at the northeast corner of the basin. That is, there is an isolated source rather than a line source as in Fig.2.3 or 2.5 for the model Pacific.

This has prompted us to use an isolated source located in the central part of a square basin on a β-plane in the northern hemisphere, where the equator is the southern boundary. It is an idealization of the concentrated sinking in Holland's experiment. Figure 2.9 shows the result when horizontal diffusion κ is absent. We observe an anticyclonic circulation, surrounding the source area from northwest to southeast; the high pressure is elongated zonally due to β-effect. A cyclonic counter circulation exists just outside of it. Upwelling is found almost everywhere, except in a small area of weak downwelling to the northwest and to the east of the source. We see that water can downwell even without κ, but that downwelling is weak when κ is absent.

The introduction of κ, however, alters the distribution not only of vertical but also of horizontal velocities, as shown in Fig.2.10. Contours of pressure become more circular, though zonal asymmetry and latitude-dependence are evident. Horizontal diffusion removes the cyclonic counter circulation observed in Fig.2.9, simplifying the horizontal current field. The distribution of vertical velocity becomes complicated, however. First, the magnitude gets larger (note the different contour intervals). Second, deep water downwells in a large interior area located to the northwest, southwest, and east of the source. On the other hand, deep water upwells at an intensified rate to the west of the source. A characteristic pattern of vertical velocity appears near the coastal boundary. In particular, the western boundary layer has a poleward current, which includes an offshore upwelling and an inshore downwelling sublayer. This feature is common with the previous case of Fig.2.6.

Figure 2.10 is to be compared with Fig.2.8 by Holland, with respect to the isolated source of deep water, though the latter source lies near the corner, not in the central portion. We confirm downwelling to the northwest and southwest and upwelling to the west of the sinking region. The interior distributions of vertical velocity in the two models are thus quite similar to each other. Once the response to an isolated source is obtained, it would be easy to infer what would occur when point sources are distributed along the southern boundary (see Figs.2.5 and 2.6).

2.4 ANALYSIS OF THE STEADY STATE

Since the transience toward the steady state is insensitive to the individual parametrization of (small) dissipative terms except at the final stage, it is the same as in Kawase (1987), who studied the set-up process much in detail. We therefore concentrate ourselves on the steady

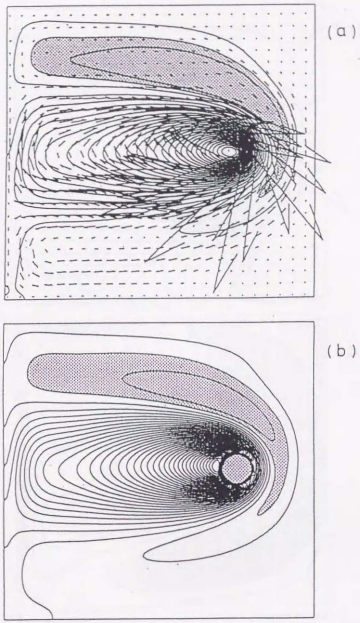

Fig.2.9 Steady response to an isolated source in the interior of a basin in the northern hemisphere when κ is absent: (a) contours for interfacial displacement η and vector arrows for horizontal velocities (u, v); (b) contours for vertical velocity w. The contour intervals are 2.2×10^2 cm and 6.4×10^{-6}cm$\cdot$s^{-1} for (a) and (b), respectively. Dotted area indicates negative values. The circulation is driven by mass addition at the central latitude in the eastern part of the basin in the form of Gaussian distribution with the characteristic radius 40 km; the rate of mass addition is 1×10^6m$^3 \cdot$s^{-1}. The dotted circle in (b) indicates strong downwelling due to the mass addition Q, though we omit the detailed contours there. The southern boundary is the equator. The zonal width $X = 2000$ km, meridional width $Y = 2000$ km, phase speed c due to the reduced-gravity $= 200\,\mathrm{cm} \cdot \mathrm{s}^{-1}$, $\nu = 1 \times 10^8 \mathrm{cm}^2\mathrm{s}^{-1}$, $\kappa = 0\mathrm{cm}^2\mathrm{s}^{-1}$, $1/R = 300$ days, $1/\lambda = 300$ days, $\beta = 2.3 \times 10^{-13}\mathrm{cm}^{-1}\mathrm{s}^{-1}$, $\Delta x = 20$ km, and $\Delta y = 20$ km,

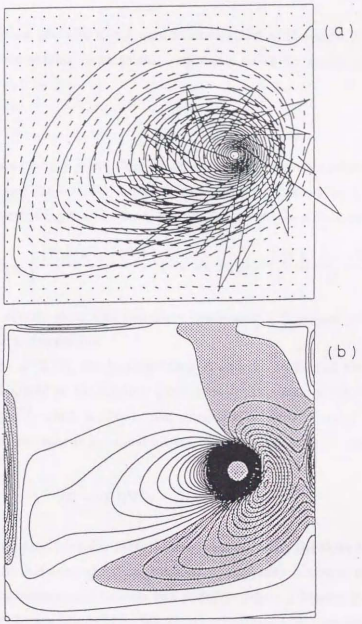

Fig.2.10 The same as Fig.2.9 except that κ is $1 \times 10^8 \mathrm{cm}^2\mathrm{s}^{-1}$. The contour intervals are 1.16×10^2 cm and $1.59 \times 10^{-5} \mathrm{cm} \cdot \mathrm{s}^{-1}$ for (a) and (b), respectively. See legend of Fig.2.9 for the other detailed conditions.

state. Even this linear problem is not easy to understand as it stands, so that we introduce further reasonable simplifying assumptions: sufficiently small dissipation and quasi-geostrophy for most cases.

2.4.1 *f-plane*

Let us begin with an f-plane. The phase velocity of shallow water internal gravity waves equals $c = \sqrt{g'H}$ and the internal radius of deformation is defined by $l_d = c/f$. Assuming steady state and eliminating u and v from (2.1)–(2.3), we obtain a sixth-order equation

$$(R - \nu\nabla^2)\nabla^2\eta - \left\{\frac{f^2 + (R - \nu\nabla^2)^2}{c^2}\right\}(\lambda - \kappa\nabla^2)\eta = -\left\{\frac{f^2 + (R - \nu\nabla^2)^2}{c^2}\right\}Q. \qquad (2.12)$$

We can and must specify *three* zero boundary conditions: (1) normal velocity, (2)tangential velocity, and (3) normal mass-flux.

In the braces of (2.12), the Rayleigh drag R and the horizontal viscosity ν usually are negligibly small compared to the Coriolis parameter f. The scale at which ν is significant is estimated as $l \sim \sqrt{\nu/f}$, which is about 3 km when $\nu = 10^7 \mathrm{cm}^2\mathrm{s}^{-1}$ and $f = 10^{-4}\mathrm{s}^{-1}$. Such a scale is too small to be realistic in actual oceans. Thus we neglect this term and approximate (2.12) by

$$(R - \nu\nabla^2)\nabla^2\eta - \frac{1}{l_d^2}(\lambda - \kappa\nabla^2)\eta = -\frac{Q}{l_d^2}. \qquad (2.13)$$

This fourth-order equation (singular perturbation) cannot satisfy the three boundary conditions mentioned above. In this approximation, however, the velocity is almost geostrophic, and the tangential velocity is proportional to mass flux $\propto \partial\eta/\partial s$, where s denotes the distance from the boundary. Thereby the conditions of no tangential velocity and no mass-flux have degenerated into one and the same condition.

Before proceeding further, let us discuss the physical meaning of (2.13) in relation to the conservation of potential vorticity:

$$\frac{d}{dt}\left\{\zeta + f - \left(\frac{f}{H}\right)\eta\right\} = \text{diffusion terms} + \text{forcing terms}, \qquad (2.14)$$

where d/dt is the material derivative. Because we are concerned with linear problems on an f-plane, the left-hand side of (2.14) vanishes, while the right-hand side is composed of the dissipations of the relative vorticity and the thickness term:

$$0 = (-R + \nu\nabla^2)\zeta - (-\lambda + \kappa\nabla^2)\left\{\left(\frac{f}{H}\right)\eta\right\} + \text{forcing terms}. \qquad (2.15)$$

If $(g'/f)\nabla^2\eta$ is substituted for ζ (quasi-geostrophic approximation), we find that (2.15) is no other than (2.13).

Henceforth we always assume $R \sim \lambda$. Our principal analytical tool is the scale of boundary layers, so that the forcing term is not written explicitly. Let $l_s = (l_d\nabla)^{-1}$ be a *symbolic* characteristic scale measured by the radius of deformation l_d. Then, (2.13) becomes

$$1 - \left(\frac{R}{\lambda} + \frac{\kappa}{\lambda l_d^2}\right) l_s^{-2} + \frac{\nu}{\lambda l_d^2} l_s^{-4} = 0. \tag{2.16}$$

First, consider a situation of very small ν (Case I), which is fundamental in the sense that κ appears in a simplest form. We have two characteristic scales:

$$l_s^{moderate} \simeq \sqrt{\frac{R}{\lambda} + \frac{\kappa}{\lambda l_d^2}} \geq \sqrt{\frac{R}{\lambda}} \sim 1 \tag{2.17}$$

and

$$l_s^{short} \simeq \sqrt{\frac{\nu}{Rl_d^2 + \kappa}} \ll 1. \tag{2.18}$$

It is possible for $l_s^{moderate}$ to be much greater than 1. The small scale (2.18) is to assure the no-slip (and no mass-flux) condition, but it is too small to be realistic. In the singular limit of $\nu \to 0$, (2.13) becomes a second-order equation.

$$\lambda\eta - (Rl_d^2 + \kappa)\nabla^2\eta = 0, \tag{2.19}$$

where we can require only one boundary condition, i.e., zero normal velocity. The inner narrower layer is ignored in this approximation. The characteristic scale (2.17) becomes wider than when κ is absent at all as in Talley (1979). The vertical velocity is estimated to be

$$w_u = Rl_d^2\nabla^2\eta = \frac{\lambda Rl_d^2}{Rl_d^2 + \kappa}\eta \tag{2.20}$$

from (2.4) and (2.19). When water is supplied from the outer ocean, η should be positive; note that (2.19) is a Poisson equation; upwelling occurs everywhere, and it is stronger near the boundary. Thus the dynamics governed by λ, R, and κ does not produce downwelling on an f-plane.

Secondly, we put $\kappa \sim \nu$. There are two subregimes according as $\kappa/\lambda l_d^2 \ll 1$ (Case IIa) or $\kappa/\lambda l_d^2 \gg 1$ (Case IIb). The former is similar to Case I just above; the only realistic scale is

$$l_s \simeq \sqrt{\frac{R}{\lambda}} \sim 1 \tag{2.21}$$

in agreement with Talley (1979).

In Case IIb, however, we have

$$l_s^{moderate} \simeq \sqrt{\frac{\nu}{\kappa}} \sim 1 \tag{2.22}$$

and

$$l_s^{long} \simeq \sqrt{\frac{\kappa}{\lambda l_d^2}} \gg 1. \tag{2.23}$$

In the broader layer (2.23), where the vertical and the horizontal diffusions of the thickness term are dominant, $w_u = (\lambda - \kappa\nabla^2)\eta = l_d^2(R - \nu\nabla^2)\nabla^2\eta$ takes the same sign that $(R/\lambda - \nu/\kappa)\nabla^2\eta$, while in the narrow layer, $w_u = l_d^2(R - \nu\nabla^2)\nabla^2\eta$ has the same sign that $-\nabla^4\eta$. In other words, w_u is positive near the boundary, but can be even negative though weak in the broader layer when $R/\lambda - \nu/\kappa$ is negative, i.e., when ν is large relative to κ.

Thirdly let us neglect κ, while we still assume $R \sim \lambda$ and $\nu \gg \lambda l_d^2$ (Case III). The characteristic scales become complex:

$$l_s \sim \left(\frac{\pm 1 \pm i}{\sqrt{2}}\right)\left(\frac{\nu}{\lambda l_d^2}\right)^{\frac{1}{4}} \gg 1 \qquad \text{(in magnitude)}, \tag{2.24}$$

which is narrower than the scale (2.23) due to κ. We find a distribution

$$w_u \propto \eta \sim exp\{-p_r s\}\cos\left(p_i s - \frac{\pi}{4}\right). \tag{2.25}$$

like the Ekman layer, and

$$v_t \sim exp\{-p_r s\}\sin(p_i s). \tag{2.26}$$

near the boundary, where $p = -p_r + ip_i = l_s^{-1}$ with positive p_r and p_i, s the distance from the coast, v_t the velocity along the boundary. Thus the boundary layer completely differs from that in the other cases, not only in scale but also in structure.

We remark that downwelling can occur (1) when $\kappa\nabla^2\eta$ is positive even though η is positive, or (2) when η becomes negative even though $\kappa = 0$. Case IIb corresponds to the former, while Case III to the latter. It is concluded that, on an f-plane, only the horizontal viscosity ν can downwell deep water in the present model.

2.4.2 *β-plane*

In the fundamental case of $\nu = 0$, we have, like (2.12),

$$\beta\frac{\partial\eta}{\partial x}+R\nabla^2\eta-\left\{\frac{f^2+R^2}{c^2}\right\}(\lambda-\kappa\nabla^2)\eta-2\beta\left\{\frac{R^2}{f^2+R^2}\frac{\partial\eta}{\partial x}+\frac{fR}{f^2+R^2}\frac{\partial\eta}{\partial y}\right\}$$

$$=-\left\{\frac{f^2+R^2}{c^2}\right\}Q. \tag{2.27}$$

Neglecting R compared with f except very near the equator, we obtain

$$\beta\frac{\partial\eta}{\partial x}+R\nabla^2\eta-\left(\frac{f^2}{c^2}\right)(\lambda-\kappa\nabla^2)\eta=-\left(\frac{f^2}{c^2}\right)Q, \tag{2.28}$$

which is rewritten, within the quasi-geostrophic approximation, as an expression of the conservation of potential vorticity:

$$\beta v=-R\zeta-(-\lambda+\kappa\nabla^2)\left\{\left(\frac{f}{H}\right)\eta\right\}-\frac{f}{H}Q \tag{2.29}$$

which is to be compared with (2.15). When ν is incorporated, we have

$$\beta\frac{\partial\eta}{\partial x}+(R-\nu\nabla^2)\nabla^2\eta-\left(\frac{f^2}{c^2}\right)(\lambda-\kappa\nabla^2)\eta=-\left(\frac{f^2}{c^2}\right)Q \tag{2.30}$$

as an adequate extension of (2.28) and (2.29).

On a β-plane, we are interested most in the scales of western (and eastern) boundary layers; the boundary layer along the zonal coast is the same as on an f-plane. The fourth-order algebraic equation for the characteristic exponent l_s^{-1} near the western and eastern boundaries becomes

$$1-\left(\frac{R}{\lambda}+\frac{\kappa}{\lambda l_d^2}\right)l_s^{-2}+\frac{\nu}{\lambda l_d^2}l_s^{-4}=\frac{\beta l_d}{\lambda}l_s^{-1}. \tag{2.31}$$

We note that l_s^{-1} with a negative real part corresponds to the western boundary layer and with a positive real part corresponds to the eastern boundary layer. The left-hand side is composed of: (1) a constant term due to λ, which is dominant when $l_s^{-1}\simeq 0$, (2) a quadratic term, which determines the convexity at $l_s^{-1}\simeq 0$, and (3) a quartic term proportional to ν, which determines the behavior for large l_s^{-1}. The right-hand side denotes a straight line which passes the origin and has a slope proportional to β. Qualitative discussion is made as follows on the basis of Fig.2.11 expressing (2.31).

When λ is absent, one root is located always at 0 and only one positive eastern scale is possible. This small scale of the order of

$$l_s^{narrow}\sim\min\left\{\left(\frac{\nu}{\beta}\right)^{1/3},\sqrt{\frac{\nu}{\frac{c^2}{f^2}R+\kappa}}\left(\frac{c}{f}\right)\right\} \tag{2.32}$$

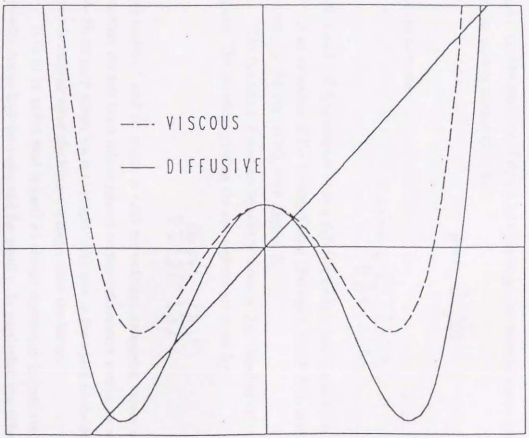

Fig.2.11 Schematic figure by which to determine the eastern and western scales in a geometrical way. The abscissa denotes the inverse of the characteristic scale. The solid (dashed) curve shows the situation of the diffusive (viscous) regime, where the western scales have two real (complex conjugate) roots.

is required for vanishing v_t at the boundary. Hence the eastern coast does not assume the usual form of a boundary layer. The other two roots have negative real parts representing the scales adequate for the western boundary layer. When the quadratic coefficient of (2.31) is small, the western boundary scales become complex and recirculation would occur; we call this type of layer a *viscous* western layer, because ν is essential for the presence of complex l_s. This situation is the same as that of Munk (1950) except for the modification by diffusion of the thickness term due to λ and κ. It is also considered as a modification of Case III on an f-plane discussed before. On the contrary, if $R/\lambda + \kappa/\lambda l_d^2$ is large, the western scales are real; the (dimensional) broader scale is estimated to be

$$l_s^{broad} \simeq \frac{R + \frac{f^2}{c^2}\kappa}{\beta} \tag{2.33}$$

and the narrower

$$l_s^{narrow} \simeq \sqrt{\frac{\nu}{\frac{c^2}{f^2}R + \kappa}}\left(\frac{c}{f}\right) \tag{2.34}$$

This case of real l_s is referred to as a *diffusive* western layer, where κ is important. We see that l_s^{broad} is an extension of the Stommel layer (Stommel, 1948). It is essentially the same as that discussed by Warren (1976), if we neglect R.

The dynamics of western boundary layers is thus classified into the viscous and diffusive regimes. The criterion dividing the two regimes are given by

$$\sqrt{\frac{3\nu}{\kappa}}\left(\frac{c}{f}\right) = \left(\frac{2\nu}{\beta}\right)^{\frac{1}{3}}, \tag{2.35}$$

if we neglect λ and R, which is valid for ordinary parameter values used in ocean modeling. Note that the left hand side is related to the deformation radius, or to the moderate scale in Case IIb on an f-plane, while the right hand side is the width of the Munk-layer. The viscous regime is realized when the former is larger than the latter.

It is to be noted that κ (and λ) always appears in a form combined with f^2/c^2; κ is more effective at high latitudes and for small c. In particular, the diffusive regime tends to be realized at high latitudes. Near the equator, where an eastward flow prevails and the interior meridional velocity is weak, the western boundary layer belongs to the viscous regime. As a consequence, multiple recirculation tends to be observed. That is, the eastward (or even the westward) current meanders about the equator with the wave length of $4\pi(\nu/\beta)^{1/3}/\sqrt{3}$. Since this equatorial meander is independent of the eastward velocity of the current, it cannot be an analogue of the mid-latitude steady meander, to which the advective effect is essential. We also remark that, when the coast is not exactly the meridional one, the *effective* β becomes smaller and the diffusive regime is liable to be observed.

When non-zero λ is introduced, the 0 root becomes positive. It expresses the eastern (or rather *interior*) very broad scale

$$l_s^{eastern\ broad} \simeq \frac{\beta c^2}{\lambda f^2} + \left[\text{correction term } \frac{R + \frac{f^2}{c^2}\kappa}{\beta}\right], \tag{2.36}$$

as was discussed by Talley (1979). The potential vorticity balance there is

$$\beta\frac{\partial \eta}{\partial x} - \left(\frac{f^2}{c^2}\right)\lambda\eta + \left[\text{correction term } \left(R + \frac{f^2}{c^2}\kappa\right)\nabla^2\eta\right] \simeq 0, \tag{2.37}$$

which governs the interior dynamics, where higher-derivatives are insignificant usually. It must be noted that $l_s^{eastern\ broad}$ becomes longer when we take κ into account.

Now let us consider the distribution of w_u. It must be remembered that, on a β-plane, the interior η has considerable magnitude (Stommel and Arons, 1960; Kawase, 1987), in contrast with that on an f-plane. In the interior, $w_u \simeq \lambda\eta$ is positive, i.e., upwelling (the interior dynamics should not be affected by the introduction of κ or ν, of course). Also near the eastern coast, we expect an intensified upwelling, within the eastern small scale due to the non-slip or no mass-flux condition. In the following we examine w_u in the western boundary layer only.

When ν is small, we have the diffusive regime corresponding to (2.33) and (2.34). In the broader layer, we find

$$\begin{aligned} w_u &= \frac{c^2}{f^2}\left(\beta\frac{\partial\eta}{\partial x} + R\nabla^2\eta\right). \\ &\simeq -\triangle\eta\frac{c^2}{f^2}\left(\frac{\beta}{l_s} - \frac{R}{l_s^2}\right)exp\{-\frac{s}{l_s}\} + \lambda\eta_{interior} \end{aligned} \tag{2.38}$$

like (2.25), where $l_s = l_s^{broad}$, $\eta_{interior}$ the interior value and $\triangle\eta$ the difference between the western boundary and the interior. The coefficient of $\triangle\eta$ is approximately given by $(\beta^2 c^4)/(\kappa f^4)$. Although $\eta_{interior}$ is not necessarily small, we first investigate the contribution from $\triangle\eta$ only.

Since κ diffuses and widens the boundary layer beyond that of the Stommel layer (see (2.33)), $\beta\partial\eta/\partial x$ dominates over $R\nabla^2\eta$. Hence w_u has the same sign as $\beta H(v/f)$, where $v \simeq (g'/f)(\partial\eta/\partial x)$ has been used. Because v/f means the poleward velocity, we conclude that *upwelling* is found for *poleward* western boundary currents, while *downwelling* for *equatorward* ones (provided that the boundary term dominates over the interior one). In other words, the widened western boundary layer makes the viscous dissipation of ζ ineffective, so that the change of the planetary vorticity βv should be compensated with vortex stretching; shrinking (downwelling) for equatorward movement, while stretching (upwelling) for poleward flows. In contrast to the case on an f-plane, horizontal diffusion can produce downwelling in the western boundary layer even without horizontal viscosity.

In the inshore sublayer of (2.34), $\partial\eta/\partial x$ is adjusted to vanish at the boundary. That causes $-\kappa\nabla^2\eta$ to take the sign opposite to that in the broader layer. We therefore expect the opposite vertical motion w_u in the narrower western boundary current. The vertical motion there is explained in terms of potential vorticity as well. As is evident from (2.34), the inshore layer is narrower than the Munk-layer on account of κ, so that the vorticity is diffused excessively by horizontal viscosity. Thus the stretching must compensate this over diffusion, resulting in vertical velocity opposite to that in the offshore layer. This narrow layer may be too narrow and vertical motion there may be too strong to be realistic in the actual ocean, as was pointed out by Warren (1976). It is certain, however, that this structure appears clearly and repeatedly in various numerical experiments of the ocean general circulation.

When $(f^2/c^2)\kappa + R \simeq (f^2/c^2)\kappa$ is small, we have the viscous regime similar to the Munk layer, The surface displacement becomes

$$\eta \sim \frac{2\triangle\eta}{\sqrt{3}} e^{-p_r s} \cos\left(p_i s - \frac{\pi}{6}\right) + \eta_{interior} \tag{2.39}$$

where $-p_r + ip_i \simeq (\beta/\nu)^{\frac{1}{3}}(-1 \pm \sqrt{3}i)/2$. The meridional (poleward) velocity is

$$\frac{v}{f} \sim -\frac{2\triangle\eta}{\sqrt{3}} \frac{g'}{f^2} \left(\frac{\beta}{\nu}\right)^{\frac{1}{3}} e^{-p_r s} \sin(p_i s). \tag{2.40}$$

The boundary layer scales are less sensitive to λ and κ, but the distribution of w_u totally depends on them. It follows from (2.4) and (2.39) that

$$w_u \sim \frac{2\triangle\eta}{\sqrt{3}} \sqrt{\lambda^2 + \lambda\kappa \mid p \mid^2 + \kappa^2 \mid p \mid^4} e^{-p_r s} \cos(p_i s + \alpha) + \lambda\eta_{interior} \tag{2.41}$$

where the phase α approaches $\pi/6$ and $-\pi/6$ for $(\kappa/\lambda)(\beta/\nu)^{\frac{2}{3}} \gg 1$ and $\ll 1$, respectively. For *equatorward* western boundary currents, for which (2.40) takes negative values for $s \simeq 0$ in both hemispheres ($\triangle\eta \geq 0$), we find upwelling in a layer close to the western boundary and downwelling in a wider layer a little offshore (provided $\triangle\eta$ term dominates over $\lambda\eta_{interior}$). When the horizontal diffusion κ gets larger compared to the vertical diffusion λ, the phase α increases and the upwelling region adjacent to the boundary becomes narrower.

Thus the distribution of w_u is quite similar to that of the diffusive regime (large κ and real l_s). The potential vorticity balance, however, differs from that in the diffusive regime. The advection of the planetary vorticity is almost canceled by the viscous dissipation; the stretching term plays a rather passive role in the potential vorticity budget. The vertical velocity is determined from a simpler physics than in the diffusive regime. In short, water must upwell (downwell) to maintain high (low) pressure through an approximate relation $w_u = \lambda\eta - \kappa\nabla^2\eta$.

We note that downwelling would occur even when $\kappa = 0$. This is because η itself can be negative due to the complex structure in the viscous regime. For the ordinary parameter values of ocean modeling, however, κ is predominant, so that the amplitude is proportional to $\kappa(\beta/\nu)^{2/3}\triangle\eta$ and the phase $\alpha \simeq \pi/6$ in (2.41). Thus, horizontal diffusion is important in the distribution of the vertical velocity even in the viscous regime.

The above arguments on w_u have been based on the assumption that the contribution from $\triangle\eta$ exceeds that from $\eta_{interior}$. We must inquire into this supposition. It is obvious that, when the zonal width of the basin is larger than or comparable with the eastern scale (2.36), $\eta_{interior}$ attenuates greatly near the western boundary, resulting in the prevalence of the $\triangle\eta$ term over the interior w_u. In the opposite case, however, the interior $w_u \sim \lambda\eta_{interior}$ may exceed w_u due to $\triangle\eta$, and consequently downwelling region may disappear in the whole basin. It demands a closer examination.

As usual, consider the limit of small dissipation (λ etc.) and take the situation studied in Section 2.3.2 as an example. For the diffusive western layer, we have

$$\frac{\kappa\triangle\eta}{l_s^2\lambda\eta_{interior}} \simeq \frac{1}{\lambda}\frac{\kappa}{l_s^2}\frac{\lambda f^2 X}{\beta c^2}\frac{Y-2y}{\beta y} \simeq \frac{c^2}{\beta\kappa Y}\frac{XY(Y-2y)}{y^3} \tag{2.42}$$

where Y is the latitude of the northern boundary, and we have assumed $Rl_d^2 \ll \kappa$. We see that (2.42) is small where the western boundary current changes its direction ($y = Y/2$).

In the viscous regime, where l_s is complex, we find

$$\frac{\kappa\triangle\eta}{l_s^2\lambda\eta_{interior}} \simeq \frac{\kappa\beta XY^2}{c^2(\frac{\nu}{\beta})^{\frac{2}{3}}}\frac{y(Y-2y)}{Y^2} \tag{2.43}$$

in the same way as for the diffusive regime. Because the viscous regime occurs at low latitudes and (2.43) is proportional to y, we expect $\eta_{interior}$ is dominant near the equator as well as around $y = Y/2$.

For realistic values of parameters, (2.42) and (2.43) is much larger than unity; $c^2/(\beta\kappa Y) \simeq 100$ and $(\kappa\beta XY^2)/(c^2(\nu/\beta)^{2/3}) \simeq 30$ when $c = 2\times10^2\mathrm{cm\,s^{-1}}, \beta = 2\times10^{-13}\mathrm{cm^{-1}\,s^{-1}}, X = Y = 2000\,\mathrm{km}, \kappa = 10^7\mathrm{cm^2\,s^{-1}}$ and $\nu = 10^8\mathrm{cm^2\,s^{-1}}$. It is important to note that the vertical velocity w_u is not determined solely by the structure of the western boundary layer, but depends on the global dynamics; it is sufficient to point out that both (2.42) and (2.43) are proportional to the zonal scale X of the basin in concern.

2.4.3 *Response to an isolated source*

Finally in this section let us examine a flow in an unbounded region. Consider a concentrated source on a mid-latitude β-plane. The situation is described by

$$\beta\frac{\partial\eta}{\partial x}+R\nabla^2\eta-\nu\nabla^4\eta-\left(\frac{f^2}{c^2}\right)(\lambda-\kappa\nabla^2)\eta=-\frac{f^2}{c^2}\delta(x-x_0,y-y_0), \tag{2.44}$$

where δ denotes the delta function, and f is assumed constant in this approximation. We first consider the diffusive case and discard ν. The solution becomes

$$\eta=\frac{2\pi\frac{f^2}{c^2}}{R+\frac{f^2}{c^2}\kappa}\exp\left\{-\frac{\beta}{2(R+\frac{f^2}{c^2}\kappa)}(x-x_0)\right\}K_0(\mu r), \tag{2.45}$$

where K_0 is the zeroth-order modified Bessel function of the second kind, $r^2=(x-x_0)^2+(y-y_0)^2$, and

$$\mu^2=\frac{\beta^2}{4(R+\frac{f^2}{c^2}\kappa)^2}+\frac{f^2\lambda}{(R+\frac{f^2}{c^2}\kappa)c^2}\geq\frac{\beta^2}{4(R+\frac{f^2}{c^2}\kappa)^2}. \tag{2.46}$$

The flow is similar to the case when $\kappa=\nu=0$ (not shown here); pressure is positive everywhere. A feature is that κ enhances the dissipation and consequently makes the region of influence more circular. The intensity and the distribution of vertical motion, however, is strongly affected by κ. It follows from (2.45) that

$$w_u=-\left(AK_0(\mu r)+BK_1(\mu r)\frac{x-x_0}{r}\right)\exp\left\{-\frac{\beta}{2(R+\frac{f^2}{c^2}\kappa)}(x-x_0)\right\}, \tag{2.47}$$

where

$$A=\frac{\pi\frac{f^2}{c^2}\kappa\beta^2}{(R+\frac{f^2}{c^2}\kappa)^3}\left\{1-\frac{2R\lambda(R+\frac{f^2}{c^2}\kappa)}{\kappa\beta^2}\right\} \tag{2.48}$$

and

$$B=\frac{\pi\frac{f^2}{c^2}\kappa\beta^2}{(R+\frac{f^2}{c^2}\kappa)^3}\sqrt{1+\frac{4}{\beta^2}\frac{f^2}{c^2}\lambda(R+\frac{f^2}{c^2}\kappa)}. \tag{2.49}$$

When κ is absent, A is negative and B vanishes identically, so that water upwells everywhere except at the source. Thus downwelling is totally due to the $\kappa\nabla^2\eta$ term in this case. For realistic parameters of non-zero κ, A and B are positive constants and A is smaller than B.

Far from the source, upwelling occurs only in the western sector determined from

$$\frac{x-x_0}{r}<-\frac{A}{B}. \tag{2.50}$$

while the downwelling occurs elsewhere. The *critical angles* defined by (2.50) are oriented almost westward when β is dominant, but become more northwestward or southwestward as $\kappa f^2/c^2$ increases. The equatorward current is accompanied by downwelling and the poleward one by upwelling, in accordance with the argument on the balance between the planetary vorticity

advection and the vortex stretching within the offshore western boundary layer. It must be kept in mind that the intensity is much smaller in the eastern direction, so that the downwelling there is weak in general. Upwelling due to other sources or due to the boundary effects will easily mask the above downwelling in the eastern side.

When we drop κ (and R) instead of ν, we have a different dynamics similar to the viscous regime. The uniformly valid analytic solution is not easy on a β-plane, but on an f-plane we find the solution to be

$$\eta = \frac{\pi f}{2c}\sqrt{\frac{1}{\nu\lambda}}\left\{iK_0\left(\left(\frac{1+i}{\sqrt{2}}\right)\left(\frac{\lambda f^2}{\nu c^2}\right)^{\frac{1}{4}} r\right) + *\right\}, \tag{2.51}$$

where * denotes the complex conjugate. The characteristic scale is the same that in Case III on an f-plane. It should be noticed that η and w_u can be negative because of the complex oscillatory structure. The β-effect deforms the symmetric field (2.51) to be elongated westward and confined eastward. In the eastern side of the source, we have a western boundary layer in the viscous regime. It has a complex structure with a scale proportional to $(\nu/\beta)^{1/3}$. Downwelling occurs where $\lambda\eta - \kappa\nabla^2\eta$ is negative. The κ term, however, is usually dominant also in this case. A poleward counter current is found in the eastern part of this downwelling region. The sign of vertical velocity is out of phase with the meridional velocity in contrast to the diffusive regime.

To the west from the source $x < x_0$, the governing equation is approximated by

$$\beta\frac{\partial\eta}{\partial x} - \nu\frac{\partial^4\eta}{\partial y^4} - \left(\frac{f^2}{c^2}\right)\lambda\eta = 0 \tag{2.52}$$

with a singularity at (x_0, y_0). It is to be noted that if we put $\eta(x,y) = \bar{\eta}(x,y)\exp\{(\lambda f^2)(x - x_0)/(\beta c^2)\}$, we can rewrite (2.52) into the equation for the slow viscous motion in a stratified fluid (Martin and Long, 1968). A similarity solution valid for $x < x_0$ is obtained under the condition $\eta(y, x_0) = \delta(y - y_0)$. By use of Fourier transforms, we find

$$\eta(x,y) = \frac{1}{2\pi}\int_{-\infty}^{\infty}\exp(-i\sigma(y-y_0) - (\lambda f^2/c^2 + \sigma^4\nu)(x_0 - x)/\beta)d\sigma,$$

$$= \left(\frac{\beta}{\nu(x_0-x)}\right)^{\frac{1}{4}}\exp\left\{\frac{\lambda f^2(x-x_0)}{\beta c^2}\right\}\sum_{n=0}^{\infty}\left(\frac{\beta(y-y_0)^4}{\nu(x_0-x)}\right)^{\frac{n}{2}}\frac{(-1)^n\Gamma(\frac{n}{2}+\frac{1}{4})}{4\pi(2n)!}$$

$$\sim \left(\frac{\beta}{\nu(x_0-x)}\right)^{\frac{1}{4}}\frac{1}{\sqrt{6\pi}}\tau^{-\frac{1}{4}}\exp\left(-\frac{\lambda f^2(x_0-x)}{\beta c^2} - \frac{3\sqrt{3}\tau}{2}\right)\sin\left(\frac{3\tau}{2}+\frac{\pi}{3}\right), \tag{2.53}$$

where Γ denotes the gamma function and $\tau = \{(\beta/\nu(x_0 - x))^{1/4}(y - y_0)/4\}^{4/3}$. The former equation gives the Taylor expansion valid near $y - y_0 \simeq 0$ and the latter the asymptotic approximation to the lowest order valid in the far field.

The meridional width spreads westward as $\{(x_0 - x)\nu/\beta\}^{\frac{1}{4}}$, so that the field is more elongated than the one dominated by κ. The field assumes a form of damped oscillation as indicated by the asymptotic formula. We therefore find alternating positive and negative η (or w_u) to the northwest (southwest) of the source area. When a moderate value of κ is introduced, the second-order diffusive derivative dominates over the fourth-order viscous one in the far western field. Therefore the oscillatory feature due to viscosity tends to be masked.

The above analyses are used for understanding the figure presented in the previous section, though the detailed interpretation is omitted.

2.5 SUMMARY AND DISCUSSION

A reduced-gravity model is developed for studying abyssal circulations. In addition to the ordinary Newtonian cooling (Talley, 1977; Kawase, 1987; Kubota and Ono, 1992), horizontal diffusion is introduced into the reduced-gravity model, though it was once argued also by Warren (1976) in his study of the broad deep western boundary current in the South Pacific. The effect of horizontal diffusion is investigated here in a global context, within the reduced-gravity model on f- and β- planes. The horizontal diffusion turns out to produce abundant flow structures exemplified in Section 2.3 and analyzed in Section 2.4. They are not merely interesting in view of geophysical fluid dynamics, but also important in view of physical interpretation of ocean dynamics simulated by various numerical models based on the primitive equations.

First, the model is applied to the Philippine Sea with a schematic topography. Our model shows features that are partially in common with and partially different from previous studies based on hydrographic data analysis or a reduced-gravity numerical model. The inflow through the Yap-Mariana Junction and the Kyushu-Palau Ridge with a gap around 18°N caused three abyssal gyres in the Philippine Sea; one in the West Mariana and two in the Philippine Basin. An equatorward western boundary current was accompanied by downwelling in the western part of the Philippine Basin. These characteristics are not inconsistent with the recent hydrographic analysis by Uehara and Taira (1990). The southward current, however, is associated with downwelling, in contrast with the result of Kubota and Ono (1992).

Second, bearing the Pacific in mind, we consider a situation similar to that of the three-dimensional numerical experiment by Suginohara and Fukasawa (1988). Mass addition near the southern boundary drives the abyssal circulation in both hemispheres. The horizontal flow naturally resembles that envisioned by Stommel and Arons (1960) and also that in the deep layer simulated by Suginohara and Fukasawa (1988). The most striking feature is the distribution of vertical motion. Our model reproduces the complicated distribution of vertical velocity in the numerical experiment based on the primitive equations, along the western boundary layer

and in the interior region. Recalling previous numerical experiments by, e.g., Holland (1971), or Bryan (1987), we note that this distribution of vertical motion has been ubiquitous. Such a distribution has raised questions, but only a *physical feeling*, in his own words, was given by Veronis (1975). A recipe provided by Veronis to avoid a wide downwelling region was to choose κ *much* smaller than ν; no discussion was given how small κ should be, or how it should be related with f or stratification. Succeeding researchers also have ascribed it to sharp fronts and too large horizontal diffusion relative to horizontal viscosity after Veronis. (Collin de Verdière, 1989; Holland, 1989). To the authors' knowledge, no further development has been attempted with respect to this strange feature, even though it is familiar to numerical modelers. The analysis in Section 2.4, however, explains in a quantitative way how wide the western and eastern layers are, and how the structure depends on the local and global parameters; β, viscosity, diffusion, density stratification, and area of the basin.

Third, the response is examined to an isolated mass source in a square basin at mid-latitudes. Horizontal and vertical motions are compared between the models with and without κ. The horizontal diffusion weakens the effect of β and greatly alters the distribution of vertical motion. Whereas the model without κ shows the upwelling almost everywhere, the introduction of κ induces downwelling of enhanced intensity in an expanded area. In the interior, we have neither steep fronts nor too strong horizontal diffusion compared with horizontal viscosity. Nevertheless there occurs a wide area of downwelling.

An important concept presented in this paper is the diffusion of the thickness term in potential vorticity. Under the presence of diffusion, the quasi-geostrophic equation would be represented better by

$$\frac{\partial}{\partial t}(\nabla^2\eta - \frac{f^2}{c^2}\eta) + J(\eta, \nabla^2\eta - \frac{f^2}{c^2}\eta) + \beta\frac{\partial\eta}{\partial x}$$
$$= -(R - \nu\nabla^2)\nabla^2\eta + (\lambda - \kappa\nabla^2)\frac{f^2}{c^2}\eta, \tag{2.54}$$

where f is regarded constant and J is the Jacobian. When simulations based on the quasi-geostrophic equation are compared with those based on the primitive equations with mass diffusion, the last term of (2.54) would be important especially for slow motions associated with boundary layers or the quasi-steady state in response to the external forcing.

Although motivated by the abyssal circulation of the Philippine Sea, the present study, we believe, gives a wide perspective of ocean dynamics. It is applicable also to the upper circulation, if only we replace the abyssal layer with the surface layer. For instance, (2.30) or (2.54) gives a significant generalization of the Sverdrup-Stommel-Munk dynamics. Let the upper layer be driven by the wind-induced Ekman suction. We then obtain a surface circulation similar to those of Stommel and Munk; the almost Sverdrup region in the interior and the

western boundary layer. A notable difference lies in the structure of (both the eastern and the western) boundary layers and the vertical motion there. The western boundary layer depends also on the stratification in the *diffusive* regime, where recirculations disappear.

In reality, an example is found in a paper of Bryan (1987), who investigated the κ-sensitivity of the wind-driven and thermohaline ocean general circulation. He pointed out that the increase in κ made recirculation disappear completely in the surface western boundary current. This is interpreted as the transition between the viscous and diffusive regimes. It is not difficult to notice that, in his Fig.16, the warm core is accompanied by downwelling, stronger than that expected from the Ekman suction; the isotherm there is pushed downward relative to those in the interior. Thus the surface western boundary layer in the subtropical gyre is composed of strong coastal upwelling and weak offshore downwelling, either in the viscous or in the diffusive regime. These phenomena are to be understood just in the same way as in the abyssal layer.

A better example of the theory was obtained in a recent numerical study carried out by Yoon (1990, private communication). He simulated the East Korean Current driven by an inflow through the Tsushima Strait and investigated its seasonal variation with a fixed value of κ. Let us remember that the effective κ is measured by $\kappa f^2/c^2$. It was narrow and was accompanied by recirculation in summer, when the density stratification is strong or c is large. In the opposite situation of winter, however, it became broader and no recirculation was observed. The current was associated with inshore narrow upwelling and offshore wider downwelling. All of these results agree well with the theory here, if only we reverse the vertical direction.

The effect of the bottom topography is entirely disregarded for simplicity in this paper. Since the bottom configuration crucially affects the abyssal flow, its theoretical investigation is desirable. Also this study is concerned only with a reduced-gravity model, which corresponds to the first baroclinic mode. We are now preparing a paper dealing with multiple vertical modes in order to study three-dimensional thermohaline circulations. The vertical structure of the flow field will be discussed and compared with observations and three-dimensional (multi-level) numerical simulations, though with limitations inherent to a linear model. The present investigation of a *single* vertical mode provides the basis for such a multi-mode solution, since the latter is a synthesis of all the vertical modes.

The present model is conceptual and linear, so that the details of formation of abyssal water and set-up of density stratification are beyond its scope. Such problems must be studied by numerical means or by more sophisticated conceptual models. We would like to emphasize, however, that the overall pattern of deep circulation found in the complicated three-dimensional simulation can be understood in terms of such a simplified model as the present.

western boundary layer. A notable difference lies in the structure of (both the eastern and the western) boundary layers and the vertical motion there. The western boundary layer depends also on the stratification in the *diffusive* regime, where recirculations disappear.

In reality, an example is found in a paper of Bryan (1987), who investigated the κ-sensitivity of the wind-driven and thermohaline ocean general circulation. He pointed out that the increase in κ made recirculation disappear completely in the surface western boundary current. This is interpreted as the transition between the viscous and diffusive regimes. It is not difficult to notice that, in his Fig.16, the warm core is accompanied by downwelling, stronger than that expected from the Ekman suction; the isotherm there is pushed downward relative to those in the interior. Thus the surface western boundary layer in the subtropical gyre is composed of strong coastal upwelling and weak offshore downwelling, either in the viscous or in the diffusive regime. These phenomena are to be understood just in the same way as in the abyssal layer.

A better example of the theory was obtained in a recent numerical study carried out by Yoon (1990, private communication). He simulated the East Korean Current driven by an inflow through the Tsushima Strait and investigated its seasonal variation with a fixed value of κ. Let us remember that the effective κ is measured by $\kappa f^2/c^2$. It was narrow and was accompanied by recirculation in summer, when the density stratification is strong or c is large. In the opposite situation of winter, however, it became broader and no recirculation was observed. The current was associated with inshore narrow upwelling and offshore wider downwelling. All of these results agree well with the theory here, if only we reverse the vertical direction.

The effect of the bottom topography is entirely disregarded for simplicity in this paper. Since the bottom configuration crucially affects the abyssal flow, its theoretical investigation is desirable. Also this study is concerned only with a reduced-gravity model, which corresponds to the first baroclinic mode. We are now preparing a paper dealing with multiple vertical modes in order to study three-dimensional thermohaline circulations. The vertical structure of the flow field will be discussed and compared with observations and three-dimensional (multi-level) numerical simulations, though with limitations inherent to a linear model. The present investigation of a *single* vertical mode provides the basis for such a multi-mode solution, since the latter is a synthesis of all the vertical modes.

The present model is conceptual and linear, so that the details of formation of abyssal water and set-up of density stratification are beyond its scope. Such problems must be studied by numerical means or by more sophisticated conceptual models. We would like to emphasize, however, that the overall pattern of deep circulation found in the complicated three-dimensional simulation can be understood in terms of such a simplified model as the present.

western boundary layer. A notable difference lies in the structure of (both the eastern and the western) boundary layers and the vertical motion there. The western boundary layer depends also on the stratification in the *diffusive* regime, where recirculations disappear.

In reality, an example is found in a paper of Bryan (1987), who investigated the κ-sensitivity of the wind-driven and thermohaline ocean general circulation. He pointed out that the increase in κ made recirculation disappear completely in the surface western boundary current. This is interpreted as the transition between the viscous and diffusive regimes. It is not difficult to notice that, in his Fig.16, the warm core is accompanied by downwelling, stronger than that expected from the Ekman suction; the isotherm there is pushed downward relative to those in the interior. Thus the surface western boundary layer in the subtropical gyre is composed of strong coastal upwelling and weak offshore downwelling, either in the viscous or in the diffusive regime. These phenomena are to be understood just in the same way as in the abyssal layer.

A better example of the theory was obtained in a recent numerical study carried out by Yoon (1990, private communication). He simulated the East Korean Current driven by an inflow through the Tsushima Strait and investigated its seasonal variation with a fixed value of κ. Let us remember that the effective κ is measured by $\kappa f^2/c^2$. It was narrow and was accompanied by recirculation in summer, when the density stratification is strong or c is large. In the opposite situation of winter, however, it became broader and no recirculation was observed. The current was associated with inshore narrow upwelling and offshore wider downwelling. All of these results agree well with the theory here, if only we reverse the vertical direction.

The effect of the bottom topography is entirely disregarded for simplicity in this paper. Since the bottom configuration crucially affects the abyssal flow, its theoretical investigation is desirable. Also this study is concerned only with a reduced-gravity model, which corresponds to the first baroclinic mode. We are now preparing a paper dealing with multiple vertical modes in order to study three-dimensional thermohaline circulations. The vertical structure of the flow field will be discussed and compared with observations and three-dimensional (multi-level) numerical simulations, though with limitations inherent to a linear model. The present investigation of a *single* vertical mode provides the basis for such a multi-mode solution, since the latter is a synthesis of all the vertical modes.

The present model is conceptual and linear, so that the details of formation of abyssal water and set-up of density stratification are beyond its scope. Such problems must be studied by numerical means or by more sophisticated conceptual models. We would like to emphasize, however, that the overall pattern of deep circulation found in the complicated three-dimensional simulation can be understood in terms of such a simplified model as the present.

REFERENCES

Bainbridge, A. E., 1981: GEOSECS Atlantic expedition, Vol. 2: Sections and Profiles. U.S. Govt. Printing Office, 198pp.

Bryan, F., 1986: Maintenance and variability of the thermohaline circulation. Ph.D. thesis, Princeton University, Princeton, 254pp.

Bryan, F., 1987: Parameter sensitivity of primitive equation ocean general circulation models. *J. Phys. Oceanogr.*, **17**, 970–985.

Collin de Verdière, A., 1989: On the interaction of wind and buoyancy driven gyres. *J. Marine Res.*, **47**, 595–633.

Cox, M. D. and K. Bryan, 1984: A numerical model of the ventilated thermocline. *J. Phys. Oceanogr.*, **14**, 674–687.

England, M. H., 1993: Representing the global-scale water masses in the ocean general circulation model. *J. Phys. Oceanogr.*, **23**, 1525–1552.

Fiadeiro, M. E., 1982: Three-dimensional modeling of tracers in the deep Pacific Ocean: II. Radiocarbon and the circulation. *J. Mar. Res.*, **40**, 537–550.

Fukasawa, M., T. Teramoto, and K. Taira, 1986: Abyssal current along the northern periphery of Shikoku Basin. *J. Oceanogr. Soc. Japan*, **42**, 459–472.

Holland, W. R., 1971: Ocean tracer distributions. Part I. A preliminary numerical experiment. *Tellus*, **23**, 371–392.

Holland, W. R. 1989: Experiences with various parametrizations of sub-grid scale dissipation and diffusion in numerical models of ocean circulation, In: *Parametrization of small-scale processes*, P. Müller and D. Henderson, eds., Hawaii Institute of Geophysics Special Publication 1989, pp. 1–9.

Ishizaki, H., 1994: A Simulation of the Abyssal Circulation in the North Pacific Ocean. Part I: Flow Field and Comparison with Observations. *J. Phys. Oceanogr.*, **24**, 1921–1939.

Kaneko, I., 1984: Structure of mid-depth water in the Philippine Sea. Doctor's thesis, University of Tokyo, Tokyo, 97pp.

Kawase, M., 1987: Establishment of mass-driven abyssal circulation. *J. Phys. Oceanogr.*, **17**, 2294–2317.

Kubota, M. and H. Ono, 1992: Abyssal circulation model of the Philippine Sea. *Deep-Sea Res.*, **39**, 1439–1452.

Mantyla, A. W. and J. L. Reid, 1983: Abyssal characteristics of the world ocean waters, *Deep-Sea Research*, **30**, 805–833.

Martin, S. and R. R. Long, 1968: The slow motion of a flat plate in a viscous stratified

fluid. *J. Fluid Mech.*, **31**, 669–688.

Masuda, A., 1989: A laboratory experiment on the Kuroshio meander. *Deep-Sea Res.*, **36**, 1067–1081.

McCreary, J. P., 1981: A linear stratified model of the Equatorial Undercurrent. *Phil. Trans. R. Soc. London*, **A298**, 603–635.

Moore, D. W., 1963: Rossby waves in ocean circulation. *Deep-Sea Res.*, **10**, 724–747.

Munk, W. H., 1950: On the wind-driven ocean circulation. *J. Meteorol.*, **7**, 79–93.

Stommel, H., 1948: The westward intensification of wind-driven ocean currents. *Trans. Amer. Geophys. Union*, **29**, 202–206.

Stommel, H. and A. B. Arons, 1960: On the abyssal circulation of a world ocean—II. An idealized model of the circulation pattern and amplitude in oceanic basins. *Deep-Sea Res.*, **6**, 217–244.

Suginohara, N. and S. Aoki, 1991: Buoyancy-driven circulation as horizontal convection on β-plane. *J. Mar. Res.*, **49**, 295–320.

Suginohara, N. and M. Fukasawa, 1988: Set-up of deep circulation in multilevel numerical models. *J. Oceanogr. Soc. Japan*, **44**, 315–336.

Talley, L., 1979: Steady two-layer source-sink flow. *1979 summer Study Program in Geophysical Fluid Dynamics at the Woods Hole Oceanographic Institution: Notes on Polar Oceanography,* Vol. 2, Woods Hole Oceanographic Institution, 97–118.

Toggweiler, J. R., 1994: The Ocean's Overturning Circulation. *Physics Today,* No. 11, 45–50.

Uehara, K. and K. Taira, 1990: Deep hydrographic structure along 12°N and 13°N in the Philippine Sea. *J. Oceanogr. Soc. Japan*, **46**, 167–176.

Veronis, G., 1975: The role of models in tracer studies. In: *Numerical Models of the Ocean Circulation*, Natl. Acad. Sci., Washington, D.C., pp. 133–146.

Warren, B. A., 1976: Structure of deep western boundary currents. *Deep-Sea Res.*, **23**, 129–142.

Yoshioka, N., M. Endoh, and H. Ishizaki, 1988: Observation of the abyssal current in the West Mariana Basin. *J. Oceanogr. Soc. Japan*, **44**, 33–39.

Chapter 3

Expansion of the ocean thermohaline circulation in terms of diffusive vertical modes and their solution by a direct method

Abstract

The diffusive reduced-gravity model developed in Chapter 2 for the gravest baroclinic mode of thermohaline circulation is generalized to a multi-mode model that is composed of a number of diffusive vertical modes. First, the three-dimensional field of ocean general circulation is shown to be expanded in terms of diffusive vertical modes. Then, a direct method of solution is developed to obtain the steady state of each mode numerically. The direct method turns out accurate and efficient compared with the conventional procedure to achieve the steady state by time integration, through application to the calculation of the first mode of thermohaline circulation in an idealized ocean similar to the Pacific. The same thermohaline circulation is used also to illustrate how the multi-mode model synthesizes multiple vertical modes to construct the three-dimensional field and how it is interpreted as the synthesis of multiple diffusive modes.

3.1 INTRODUCTION

Ocean general circulation is so difficult to understand that it is worthwhile to view it from various angles. As such an attempt, the diffusive reduced-gravity model was developed in Chapter 2 which succeeded in clarifying many gross features of the abyssal circulation realized in numerical experiments based on OGCMs (Ocean General Circulation Models). In particular, this model explained the strange distribution of upwelling and downwelling in the abyssal layer and the structure of various boundary layers not only near the western boundary but also in the internal region. The model was applied also to the abyssal flow in the ocean of variable depth to reveal characteristic circulations around an isolated bottom feature that are totally due to viscosity of momentum and diffusion of density (Masuda and Mizuta, 1995).

The diffusive reduced-gravity model, however, was oriented to the study of the first baroclinic mode, the dominant component of the abyssal circulation. Since a number of vertical modes must contribute to the real circulation, any model of a single mode cannot answer how other modes modify the circulation. In other words, the diffusive reduced-gravity model cannot determine the three-dimensional current field, because the vertical distribution is prescribed beforehand in that model.

It therefore is necessary to develop a framework along which the three-dimensional field of ocean general circulation is approached in a more systematic way than in the diffusive reduced-gravity model. Since this framework is rather complicated and requires involved procedures for numerical solution, we confine the purpose of this article to this preparation. An example is presented here to examine how the present methodology works. Further application to thermohaline circulation and comparison with experiments based on an ordinary OGCM will be made in another paper.

Diffusive vertical modes are formulated in the next section. It is argued how to expand the three-dimensional field in terms of diffusive vertical modes and how to synthesize the circulation field in the modal domain to give the circulation in the physical domain. As an efficient means to obtain the steady state solution of each mode equation, a direct method is developed in the third section. The accuracy and efficiency are compared with those of the method to obtain the steady state by time integration for the first baroclinic mode of thermohaline circulation in an idealized ocean similar to the Pacific. Then the fourth section illustrates how the multi-mode model synthesizes a number of diffusive vertical modes to build up the three-dimensional structure of thermohaline circulation. A summary and discussion is given in the final section.

3.2 DIFFUSIVE VERTICAL MODES

As is the case for most phenomena of the ocean, thermohaline circulation is essentially three-dimensional. This three-dimensional nature makes it difficult to understand the mecha-

nism that maintains the thermohaline circulation of the ocean. One way to bypass that difficulty is to reduce the dimension of independent variables by expanding the field variables in terms of vertical modes. In this sense, a number of oceanographic researches have been concerned with vertical modes relevant to long gravity waves (Krauss, 1966; McCreary, 1981; Wajsowicz and Gill, 1986; Pedlosky, 1992; Masuda and Uehara, personal communication). So far as we know, however, few oceanographic works have dealt with the expansion in vertical modes in relation to the steady thermohaline circulation; most have been concerned with the wave-mechanical response or the surface current. We therefore go into details about the governing equations of each diffusive vertical mode, the boundary conditions including the thermal and mechanical forcing, and the transformation of physical variables to modal variables and *vice versa*. We call the resulting model as a multi-mode model, since it is composed of a number of diffusive vertical modes. This terminology is used to distinguish the present model from the ordinary multi-level model (based on the level formulation) or from the diffusive reduced-gravity model (for a single mode).

We start with the primitive equations in which hydrostatic and Boussinesq approximations are assumed:

$$\frac{\partial u}{\partial t} + u\frac{\partial u}{\partial x} + v\frac{\partial u}{\partial y} + w\frac{\partial u}{\partial z} - fv = -\frac{1}{\rho_c}\frac{\partial p}{\partial x} + \frac{\partial}{\partial z}\left(\nu_V \frac{\partial u}{\partial z}\right) + \nabla_H \cdot (\nu_H \nabla_H u), \tag{3.1}$$

$$\frac{\partial v}{\partial t} + u\frac{\partial v}{\partial x} + v\frac{\partial v}{\partial y} + w\frac{\partial v}{\partial z} + fu = -\frac{1}{\rho_c}\frac{\partial p}{\partial y} + \frac{\partial}{\partial z}\left(\nu_V \frac{\partial v}{\partial z}\right) + \nabla_H \cdot (\nu_H \nabla_H v), \tag{3.2}$$

$$0 = -\frac{\partial p}{\partial z} - g\rho, \tag{3.3}$$

$$\frac{\partial u}{\partial x} + \frac{\partial v}{\partial y} + \frac{\partial w}{\partial z} = 0, \tag{3.4}$$

$$\frac{\partial \rho}{\partial t} + u\frac{\partial \rho}{\partial x} + v\frac{\partial \rho}{\partial y} + w\frac{\partial \rho}{\partial z} = \frac{\partial}{\partial z}\left\{(\kappa_V + \kappa_{ca})\frac{\partial \rho}{\partial z}\right\} + \nabla_H \cdot (\kappa_H \nabla_H \rho), \tag{3.5}$$

where $(x,\ y,\ z)$ are (eastward, northward, upward) coordinates, $(u,\ v,\ w)$ the corresponding velocity components, $\nabla_H = (\partial/\partial x,\ \partial/\partial y,\ 0)$, t time, p pressure, ρ density, ρ_c (constant) characteristic density, g the acceleration of gravity, f the Coriolis parameter. Also $(\nu_H,\ \nu_V)$ and $(\kappa_H,\ \kappa_V)$ denote (horizontal, vertical) viscosity and diffusion coefficients, respectively. Parameter κ_{ca} in (3.5) represents the effect of convective adjustment (Bryan, 1969) to remove static instability:

$$\kappa_{ca} = \begin{cases} \infty & \frac{\partial \rho}{\partial z} > 0, \\ 0 & \text{otherwise.} \end{cases} \tag{3.6}$$

For simplicity, we regard density to be a linear function of temperature only. Also the depth of the basin D is assumed constant to avoid the interference between different vertical modes via bottom topography.

Now we modify (3.1)–(3.5) into equations suitable for the multi-mode model. First, we divide each field variable into a reference value denoted by an overbar and its deviation denoted by a prime:

$$(u,\ v,\ w) = (\bar{u}(z),\ \bar{v}(z),\ \bar{w}(z)) + (u'(x,y,z,t),\ v'(x,y,z,t),\ w'(x,y,z,t)), \tag{3.7}$$

$$\rho(x,y,z,t) = \bar{\rho}(z) + \rho'(x,y,z,t), \tag{3.8}$$

$$p(x,y,z,t) = \bar{p}(z) + p'(x,y,z,t). \tag{3.9}$$

We require the reference current to vanish, so that $(u', v', w') = (u, v, w)$. The reference pressure and the reference density are related with each other by hydrostatic balance

$$\frac{d\bar{p}}{dz} = -\bar{\rho} g. \tag{3.10}$$

In order to assure the mutual independence of vertical modes in the equations of motion, we must put aside the nonlinear terms. Moreover, the vertical eddy viscosity and vertical mass diffusion are replaced by those proportional to $1/N^2$ (Krauss, 1966; McCreary, 1981):

$$\tilde{\nu_V} = \frac{C_\nu}{N^2}, \qquad \tilde{\kappa_V} = \frac{C_\kappa}{N^2}, \tag{3.11}$$

where N^2 is the square of the buoyancy frequency for the basic stratification defined by

$$N^2(z) = -\frac{g}{\rho_c}\frac{d\bar{\rho}}{dz}, \tag{3.12}$$

and the two constants C_ν and C_κ are chosen for the overall $\tilde{\nu_V}$ and $\tilde{\kappa_V}$ to agree with ν_V and κ_V, respectively. In addition, the form of vertical diffusion is altered into the adjoint form:

$$\frac{\partial}{\partial z}\left(\kappa_V \frac{\partial \rho}{\partial z}\right) \rightarrow \frac{\partial^2}{\partial z^2}(\tilde{\kappa_V}\rho). \tag{3.13}$$

In some situations, we may conveniently substitute the formation of deep water with a local source or sink of mass q in the equation of continuity

$$\frac{\partial u}{\partial x} + \frac{\partial v}{\partial y} + \frac{\partial w}{\partial z} = q(x,y,z,t). \tag{3.14}$$

Consequently, the primitive equations (3.1)–(3.5) are converted as

$$\frac{\partial u}{\partial t} - fv = -\frac{1}{\rho_c}\frac{\partial p'}{\partial x} + \frac{\partial}{\partial z}\left(\tilde{\nu_V}\frac{\partial u}{\partial z}\right) + \nu_H \nabla_H^2 u + F^x, \tag{3.15}$$

$$\frac{\partial v}{\partial t} + fu = -\frac{1}{\rho_c}\frac{\partial p'}{\partial y} + \frac{\partial}{\partial z}\left(\tilde{\nu_V}\frac{\partial v}{\partial z}\right) + \nu_H \nabla_H^2 v + F^y, \tag{3.16}$$

$$0 = -\frac{\partial p'}{\partial z} - g\rho', \tag{3.17}$$

$$\frac{\partial u}{\partial x} + \frac{\partial v}{\partial y} + \frac{\partial w}{\partial z} = q, \tag{3.18}$$

$$\frac{\partial \rho'}{\partial t} - \frac{\rho_c N^2}{g} w = \frac{\partial^2}{\partial z^2}(\tilde{\kappa_V} \rho') + \kappa_H \nabla_H^2 \rho' + Q, \tag{3.19}$$

where the unknowns to be solved are u, v, w, ρ', and p'. The modifications of the basic equations mentioned above yield the residual terms F^x, F^y, and Q, which are to be dealt with as secondary terms or external forcing:

$$F^x(x,y,z,t) \equiv -u\frac{\partial u}{\partial x} - v\frac{\partial u}{\partial y} - w\frac{\partial u}{\partial z} + \frac{\partial}{\partial z}\left(\nu_V \frac{\partial u}{\partial z}\right) - \frac{\partial}{\partial z}\left(\tilde{\nu_V}\frac{\partial u}{\partial z}\right), \tag{3.20}$$

$$F^y(x,y,z,t) \equiv -u\frac{\partial v}{\partial x} - v\frac{\partial v}{\partial y} - w\frac{\partial v}{\partial z} + \frac{\partial}{\partial z}\left(\nu_V \frac{\partial v}{\partial z}\right) - \frac{\partial}{\partial z}\left(\tilde{\nu_V}\frac{\partial v}{\partial z}\right), \tag{3.21}$$

$$Q(x,y,z,t) \equiv -u\frac{\partial \rho'}{\partial x} - v\frac{\partial \rho'}{\partial y} - w\frac{\partial \rho'}{\partial z} + \frac{\partial}{\partial z}\left\{(\kappa_V + \kappa_{ca})\frac{\partial \rho}{\partial z}\right\} - \frac{\partial^2}{\partial z^2}(\tilde{\kappa_V}\rho'). \tag{3.22}$$

Among the residual terms, the linear ones concerning the vertical viscosity and vertical diffusion can be neglected when the stratification is approximately linear ($N \sim$ const). Nonlinear terms included in F^x, F^y, and Q may be estimated partly by successive calculation.

As the surface boundary conditions, we specify both the wind stress and the surface density in addition to the usual kinetic and dynamic conditions at the sea surface:

$$w = \frac{\partial \eta}{\partial t}, \qquad p' = \rho_c g \eta, \qquad \tilde{\nu_V}\frac{\partial}{\partial z}(u,v) = \frac{1}{\rho_c}(\tau^x, \tau^y), \qquad \rho' = \rho'_s \qquad \text{at } z = 0, \tag{3.23}$$

where η denotes the surface elevation, (τ^x, τ^y) are the (eastward, northward) components of wind stress, and ρ'_s is the specified distribution of ρ' at the surface, respectively. Note that fixed density is required at the boundary in the present formulation of vertical modes. In the same way we find appropriate boundary conditions at the bottom to be

$$w = 0, \qquad \tilde{\nu_V}\frac{\partial}{\partial z}(u,v) = (0,0), \qquad \rho' = 0 \qquad \text{at } z = -D, \tag{3.24}$$

where we have disregarded the horizontal variation of density there, which is effectively zero in most situations. On the side boundaries, the horizontal velocity must vanish and no density flux across the boundary is allowed:

$$(u,v) = (0,0), \qquad \frac{\partial \rho}{\partial n} = 0, \tag{3.25}$$

where $\partial/\partial n$ denotes the derivative normal to the boundaries.

Conversion from the physical domain and the modal domain is made through an integral transform based on a set of orthonormal basis functions. For example let us consider velocity u. The nth vertical mode is given by

$$u_n(x,y,t) = \frac{1}{D}\int_{-D}^{0} u(x,y,z,t)\hat{u}_n(z)\,dz, \tag{3.26}$$

where $\hat{u}_n$ denotes the normalized basis function of the nth mode (n=0,1,2,$\cdots$). Conversely, the vertical modes are synthesized to give the field variable:

$$u(x,y,z,t) = \sum_{n=0}^{\infty} u_n(x,y,t)\hat{u}_n(z). \tag{3.27}$$

We may write (3.26) and (3.27) as

$$u_n = \mathcal{T}[u] \qquad \text{and} \qquad u = \mathcal{T}^{-1}[\{u_n\}], \tag{3.28}$$

where $\mathcal{T}$ and $\mathcal{T}^{-1}$ symbolically stand for the transformation from the physical domain to the modal domain and *vice versa*, respectively. The definitions of $\mathcal{T}$ for other variables are shown in Appendix A.

The basis functions of different variables are related with that of p as

$$(\hat{u}_n, \hat{v}_n, \hat{w}_n, \hat{\rho}_n, \hat{q}_n, \hat{F}^x_n, \hat{F}^y_n, \hat{Q}_n) = \left(\hat{p}_n, \hat{p}_n, -\frac{c_n^2}{D}\left(\frac{1}{N^2}\frac{d\hat{p}_n}{dz}\right), -\frac{c_n^2}{g}\frac{d\hat{p}_n}{dz}, \hat{p}_n, \hat{p}_n, \hat{p}_n, -\frac{c_n^2}{g}\frac{d\hat{p}_n}{dz}\right). \tag{3.29}$$

Here $1/c_n^2$ and $\hat{p}_n(z)$ are the nth eigenvalue and the associated eigenfunction of the Sturm-Liouville equation

$$-\frac{d}{dz}\left\{\frac{1}{N^2}\left(\frac{d}{dz}\hat{p}_n\right)\right\} = \left(\frac{1}{c_n^2}\right)\hat{p}_n, \tag{3.30}$$

with the boundary conditions

$$\frac{\hat{p}_n}{N^2} = -\frac{c_n^2}{gN^2}\frac{d\hat{p}_n}{dz} = 0 \qquad (\text{at } z = -D,\ 0). \tag{3.31}$$

We choose real $\hat{p}_n$ so that $\hat{p}_n(0)$ is positive and that the orthonormal condition holds:

$$\frac{1}{D}\int_{-D}^{0} \hat{p}_n\hat{p}_m dz = \begin{cases} 0 & m \neq n, \\ 1 & m = n. \end{cases} \tag{3.32}$$

In particular, for the simple case of constant N, the eigenfunctions turn out to be trigonometric functions:

$$\hat{p}_n = \sqrt{2}\cos\left(\frac{n\pi}{D}z\right), \quad c_n = \frac{ND}{n\pi} \quad (n = 1,2,\cdots), \tag{3.33}$$

$$\hat{p}_n = 1, \quad 1/c_n = 0 \quad (n = 0), \tag{3.34}$$

so that the decomposition of p into vertical modes is none other than the Fourier cosine transform.

A note is to be added here about the dimension of the modes. For instance, the mode variable u_n has the same dimensions as the corresponding physical variable u, while its basis function $\hat{u}_n$ has no dimension. This is the case for the other variables. The formulas including mode variables therefore should read with an appropriate dimensional number of unity multiplied implicitly when necessary.

Governing equations for each vertical mode are derived by applying the transform $\mathcal{T}$ to the modified three-dimensional equations (3.15)–(3.19). As for baroclinic modes ($n \geq 1$), multiplying (3.15), (3.16), and (3.18) by $\hat{p}_n/D$, multiplying (3.17) and (3.19) by $g^2\hat{\rho}_n/\rho_c N^2 c_n^2$, and integrating them over z from $-D$ to 0, respectively, we have

$$\frac{\partial u_n}{\partial t} - fv_n = -g_n\frac{\partial \eta_n}{\partial x} - R_n u_n + \nu_H \nabla_H^2 u_n + \tilde{F}_n^x, \tag{3.35}$$

$$\frac{\partial v_n}{\partial t} + fu_n = -g_n\frac{\partial \eta_n}{\partial y} - R_n v_n + \nu_H \nabla_H^2 v_n + \tilde{F}_n^y, \tag{3.36}$$

$$\frac{\partial \eta_n}{\partial t} + D\left(\frac{\partial u_n}{\partial x} + \frac{\partial v_n}{\partial y}\right) = -\lambda_n \eta_n + \kappa_H \nabla_H^2 \eta_n + D\tilde{q}_n, \tag{3.37}$$

$$w_n = \left\{\frac{\partial}{\partial t} + \lambda_n - \kappa_H \nabla_H^2\right\}\eta_n - D(\tilde{q}_n - q_n), \tag{3.38}$$

where

$$g_n = \frac{c_n^2}{D}, \qquad \eta_n = \frac{p_n}{g_n}, \qquad R_n = \frac{C_\nu}{c_n^2}, \qquad \lambda_n = \frac{C_\kappa}{c_n^2}, \tag{3.39}$$

and forcing or additive terms:

$$\tilde{F}_n^x = \frac{\tau^x}{\rho_c}\hat{p}_n(0) + F_n^x, \qquad \tilde{F}_n^y = \frac{\tau^y}{\rho_c}\hat{p}_n(0) + F_n^y, \tag{3.40}$$

$$D\tilde{q}_n = Dq_n - \left[\frac{g}{g_n}\hat{p}_n \bar{\kappa_V}\left(\frac{\rho'}{\rho_c}\right)\right]_{-D}^{0} + DQ_n. \tag{3.41}$$

We note that mechanical or thermal boundary condition at the sea surface is split into a kind of external forcing to each vertical mode.

Finally the side boundary conditions become

$$(u_n, v_n) = (0, 0), \qquad \frac{\partial \eta_n}{\partial n} = 0. \tag{3.42}$$

As regards the barotropic mode ($n = 0$) for which $1/c_n^2$ is zero, the basic equations have slightly different forms:

$$\frac{\partial u_0}{\partial t} - fv_0 = -g\frac{\partial \eta_0}{\partial x} + \nu_H \nabla_H^2 u_0 + \tilde{F}_0^x, \tag{3.43}$$

$$\frac{\partial v_0}{\partial t} + fu_0 = -g\frac{\partial \eta_0}{\partial y} + \nu_H \nabla_H^2 v_0 + \tilde{F}_0^y, \tag{3.44}$$

$$\hat{p}_0(0)\frac{\partial \eta_0}{\partial t} + D\left(\frac{\partial u_0}{\partial x} + \frac{\partial v_0}{\partial y}\right) = D\tilde{q}_0, \tag{3.45}$$

where $\eta_0 = p_0/g$ and

$$D\tilde{q}_n = Dq_n - \sum_{n=1}^{\infty}\frac{g_n}{g}\frac{\partial \eta_n}{\partial t}\hat{p}_n(0). \tag{3.46}$$

Note that the equations governing the barotropic modes are independent of either the vertical viscosity, the vertical diffusivity, or the horizontal diffusivity. In consequence, η_0 needs no boundary condition.

They are the same diffusive reduced-gravity equations as those used in Chapter 2. The additional term of the horizontal diffusion of the interface distinguishes them from the other similar ones in Talley (1979), Kawase (1987), or Kubota and Ono (1992).

When the forcing term $D\bar{q}_n$ is steady and uniform, we find the steady response to be

$$u_n = v_n = w_n = 0, \qquad \lambda_n \eta_n = D\bar{q}_n. \tag{3.47}$$

This indicates that only the perturbed stratification is altered in response to the forcing that is independent of the horizontal coordinates. Since no current is induced, we discard this kind of forcing, assuming that this is absorbed into the formation process of the basic stratification.

It is to be noted that, within this framework, time integration is possible with nonlinear terms incorporated. For example, we have

$$F_n^x = \mathcal{T}\left[F^x\left(\{u, v, w, \rho', p'\}\right)\right] = \mathcal{T}\left[F^x\left(\{\mathcal{T}^{-1}[\{u_n\}], \mathcal{T}^{-1}[\{v_n\}], \cdots\}\right)\right], \tag{3.48}$$

as is usual for the pseudo-spectral algorithm.

3.3 SOLUTION BY A DIRECT METHOD

In studying thermohaline circulation with the multi-mode model, the steady response is to be calculated for a number of vertical modes from the lowest to higher ones. If we follow an ordinary method of time integration, however, it demands a great deal of time for computation. One reason is that the diffusive time scale for adjustment can be very large for lower (baroclinic) modes which have small diffusivities; a typical value of $1/\lambda_1$ is 10^5 days. The other reason is related with narrower boundary layers along the western and northern (southern) coasts associated with higher modes (see Chapter 2). These boundary layers are resolved only by a small size of grid, which requires a small time step for the CFL condition for numerical stability to be satisfied. As a result, the numbers of total mesh points and total time steps are increased. We therefore develop a *direct method* by which to efficiently solve the steady diffusive reduced-gravity equations in a way similar to a factorization method (Peyret and Taylor, 1983).

3.3.1 *Formulation and algorithm*

The basic equations and the boundary conditions have been presented in the previous section. The rectangular basin is discretized into $N_x \times N_y$ grid boxes for zonal and meridional directions, respectively (Fig. 3.1). Arakawa's C-grid (Mesinger and Arakawa, 1976) is adopted for the grid configuration because the scheme satisfies the mass conservation automatically.

For the meridionally jth row of grid boxes, let us define a column vector $\boldsymbol{x}_j$ by

$$\boldsymbol{x}_j \equiv {}^t(\, u_{1,j}, u_{2,j}, \cdots, u_{N_x-1,j},\ v_{1,j}, v_{2,j}, \cdots, v_{N_x,j},\ \eta_{1,j}, \eta_{2,j}, \cdots, \eta_{N_x,j}\,), \tag{3.49}$$

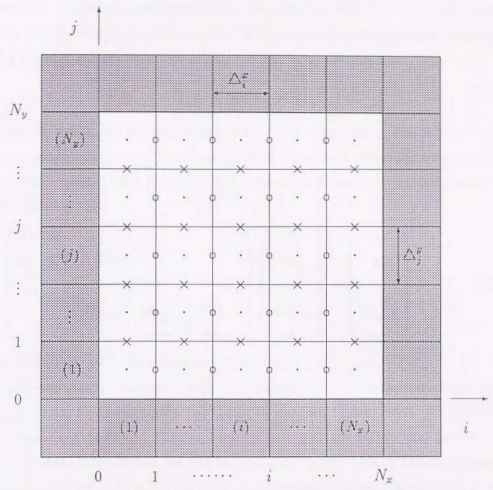

Fig. 3.1: Layout of the grid points used in the numerical calculation. Symbols ·, ∘, and × are placed at the locations where η_n, u_n, and v_n are defined, respectively.

where t indicates the transpose and the element $u_{i,j}$, for example, denotes the u at the u-point of the (i,j)th box. In this section, the suffix indicating the mode number is omitted for brevity. The discretized form of equations (3.35)–(3.37) are written in a recursive form

$$\boldsymbol{P}_j \boldsymbol{x}_{j+1} + \boldsymbol{Q}_j \boldsymbol{x}_j + \boldsymbol{R}_j \boldsymbol{x}_{j-1} = \boldsymbol{q}_j, \tag{3.50}$$

where $\boldsymbol{P}_j$, $\boldsymbol{Q}_j$, and $\boldsymbol{R}_j$ are square matrices of the $(3N_x - 1)$th order, and $\boldsymbol{q}_j$ is a column vector of $(3N_x - 1)$ components consisting of non-homogeneous terms such as forcing terms and the boundary values, respectively. The details of these vectors and matrices are summarized in Appendix B. Formally we have

$$\begin{pmatrix} \boldsymbol{Q}_1 & \boldsymbol{P}_1 & & & \\ \boldsymbol{R}_2 & \boldsymbol{Q}_2 & \boldsymbol{P}_2 & & \\ & \ddots & \ddots & \ddots & \\ & & \boldsymbol{R}_{N_y-1} & \boldsymbol{Q}_{N_y-1} & \boldsymbol{P}_{N_y-1} \\ & & & \boldsymbol{R}_{N_y} & \boldsymbol{Q}_{N_y} \end{pmatrix} \begin{pmatrix} \boldsymbol{x}_1 \\ \boldsymbol{x}_2 \\ \vdots \\ \boldsymbol{x}_{N_y-1} \\ \boldsymbol{x}_{N_y} \end{pmatrix} = \begin{pmatrix} \boldsymbol{q}_1 \\ \boldsymbol{q}_2 \\ \vdots \\ \boldsymbol{q}_{N_y-1} \\ \boldsymbol{q}_{N_y} \end{pmatrix}, \tag{3.51}$$

where the order of the matrix on the left hand side is $(3N_x - 1)N_y \times (3N_x - 1)N_y$.

As is usual for an algebraic equation with a tridiagonal matrix, a factorization technique is available to solve (3.51) for the unknown $\{\boldsymbol{x}_j\}$ (e.g., Peyret and Taylor, 1993). An important generalization is necessary, however. That is, we need to substitute vectors and matrices for scalar numbers used in the factorization method to solve quasi-geostrophic or Poisson equations (Peyret and Taylor, 1983; Masuda and Uehara, personal communication). Besides, the C-grid configuration requires a particular formulation to cope with the boundary conditions.

Following the factorization method, we relate $\boldsymbol{x}_j$ and $\boldsymbol{x}_{j+1}$ by

$$\boldsymbol{x}_j = \boldsymbol{a}_j + \boldsymbol{B}_j \boldsymbol{x}_{j+1}, \tag{3.52}$$

with an unknown vector $\boldsymbol{a}_j$ and an unknown matrix $\boldsymbol{B}_j$. Substitution of (3.52) into (3.50) yields another relation between $\boldsymbol{x}_j$ and $\boldsymbol{x}_{j+1}$:

$$\boldsymbol{x}_j = \left(\boldsymbol{Q}_j + \boldsymbol{R}_j \boldsymbol{B}_{j-1}\right)^{-1} \left(\boldsymbol{q}_j - \boldsymbol{R}_j \boldsymbol{a}_{j-1}\right) - \left(\boldsymbol{Q}_j + \boldsymbol{R}_j \boldsymbol{B}_{j-1}\right)^{-1} \boldsymbol{P}_j \, \boldsymbol{x}_{j+1}. \tag{3.53}$$

Comparing (3.52) and (3.53), we have

$$\boldsymbol{a}_j = \left(\boldsymbol{Q}_j + \boldsymbol{R}_j \boldsymbol{B}_{j-1}\right)^{-1} \left(\boldsymbol{q}_j - \boldsymbol{R}_j \boldsymbol{a}_{j-1}\right), \tag{3.54}$$

$$\boldsymbol{B}_j = -\left(\boldsymbol{Q}_j + \boldsymbol{R}_j \boldsymbol{B}_{j-1}\right)^{-1} \boldsymbol{P}_j, \tag{3.55}$$

for $j = 2, 3, \cdots, N_y - 1$, and

$$\boldsymbol{a}_1 = \boldsymbol{Q}_1^{-1} \boldsymbol{q}_1, \tag{3.56}$$

$$\boldsymbol{B}_1 = -\boldsymbol{Q}_1^{-1} \boldsymbol{P}_1, \tag{3.57}$$

for j=1. As $\boldsymbol{a}_1$ and $\boldsymbol{B}_1$ are determined by (3.56) and (3.57), we can deduce $\boldsymbol{a}_j$ and $\boldsymbol{B}_j$ for all j using (3.54) and (3.55). Once $\boldsymbol{a}_j$ and $\boldsymbol{B}_j$ are known, it is easy to find $\boldsymbol{x}_{N_y}$ as

$$\boldsymbol{x}_{N_y} = \left(\boldsymbol{Q}_{N_y} + \boldsymbol{R}_{N_y}\boldsymbol{B}_{N_y-1}\right)^{-1}(\boldsymbol{q}_{N_y} - \boldsymbol{R}_{N_y}\boldsymbol{a}_{N_y-1}). \tag{3.58}$$

Then, coming down from $\boldsymbol{x}_{N_y}$, we succesively determine $\boldsymbol{x}_{N_y-1}$, $\boldsymbol{x}_{N_y-2}$, ... by the backward use of (3.52).

3.3.2 *Comparison with the time integration method*

Properties and performance of the direct method would be best argued on an example. For this purpose the first baroclinic mode of a steady state thermohaline circulation is computed in two ways: the direct method and the conventional procedure of time integration. The abyssal circulation we consider is rather simple: it is driven by a horizontally uniform northward inflow at the inlet located at the southwestern corner of a flat rectangular ocean on a β-plane over both hemispheres. This is a simplified form of the thermohaline circulation in the Pacific Ocean, which is driven by the cold water supplied from the Antarctic Ocean while it produces no deep water in the northern hemisphere (Warren, 1983). We also assume a linear stratification for simplicity, so that the eigenfunctions are trigonometric ones. Table 3.1 shows the parameters used in the calculation. In this subsection, we assume that the inflow has the same vertical profile as the first mode, $v_f(z)$=$\hat{v}_1(z)$, so that only the first mode is generated.

Figure 3.2 is the result obtained by the direct method with the resolution of 64 × 128 grids: (a) contours of $-\eta_1$ together with the current $(-u_1, -v_1)$ indicated by arrows, and (b) contours of vertical velocity $-w_1$. Note that we have added the negative sign, or $(-1)^n$ in general, to make the variables relevant to the abyssal layer. (We have chosen the sign of the eigenfunction to give a positive value at the surface.) We observe characteristic patterns: (1) the Stommel-Arons scheme of currents in the interior region (Stommel and Arons, 1960), (2) westward intensified meander near the equator, and (3) an ordered distribution of upwelling and downwelling along the western boundary and in the interior region near the inlet. The reader may refer to Chapter 2 for their dynamics. We confirmed that the same equilibrium state was obtained by a long-term integration as well, but it took more than about 3000 days for the temporal change of the total kinetic energy to be negligible, and 300000 days for η_1 to reach the steady state because the diffusion time scale is $1/\lambda_1 \sim 100000$ days.

Table 3.2 compares the time in seconds necessary for computation on the same workstation (HP9000/730) between the direct method and the method of time integration, in the latter of which time integration was made over 10000 days with the time step fixed at a quarter of the critical value of the CFL condition. We see that the direct method is more efficient than the conventional procedure of time integration. As regards the precision, the steady solution

Table 3.1: Parameters used in the experiments carried out in sections 3.3 and 3.4.

Symbol	Value	Definition
X_w	3000 km	Zonal width of the basin
Y_w	6000 km	Meridional width of the basin
Y_N	3000 km	Distance between the northern coast and the equator
D	4000 m	Depth of the basin
ν_H	2×10^7 cm^2 s^{-1}	Horizontal eddy viscosity
ν_V	2 cm^2 s^{-1}	Vertical eddy viscosity
κ_H	2×10^7 cm^2 s^{-1}	Horizontal mass diffusion
κ_V	2 cm^2 s^{-1}	Vertical mass diffusion
β	2.3×10^{-13} cm^{-1} s^{-1}	Meridional derivative of the Coriolis parameter
Δx_f	188 km	Width of the inlet at the southern coast
N^2	3.045×10^{-6} s^{-2}	Square of the buoyancy frequency
g	980.6 cm s^{-2}	Acceleration of gravity
c_1	222.2 cm s^{-1}	Phase speed of the long gravity wave for the first mode

Table 3.2: Comparison of computation time in seconds required by the direct method (dm) and by the conventional method of time integration (ti) on a workstation (HP9000/730) for different numbers of grids. Time integration was made as long as 10000 days, the time step being a quarter of the critical value required by the CFL condition.

$N_x \times N_y$	dm	ti	$N_x \times N_y$	dm	ti	$N_x \times N_y$	dm	ti
32×64	8	522	64×64	64	2362	96×64	343	5892
32×96	12	1238	64×96	95	3893	96×96	527	9339
32×128	16	2388	64×128	128	5400	96×128	711	12572
32×192	23	6014	64×192	206	12632	96×192	1079	19288

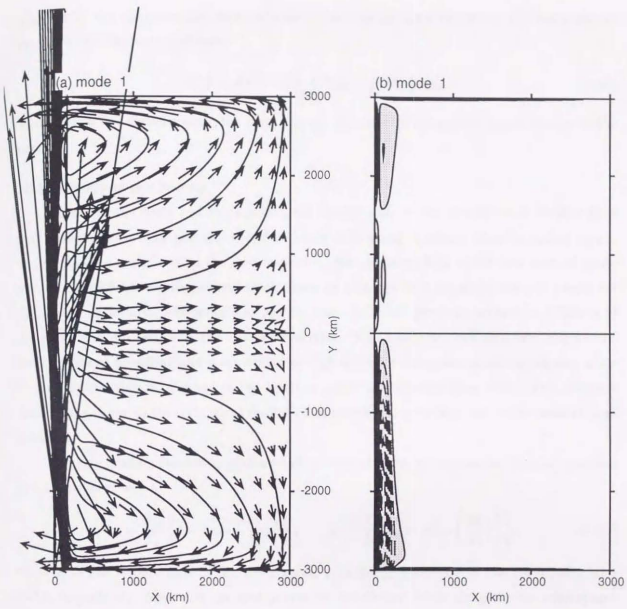

Fig. 3.2: The circulation of the first mode calculated by the direct method, which is driven by the abyssal inflow at the southern coast: (a) Velocity vector $(-u_1, -v_1)$ and contours of $-\eta_1$ corresponding to the interfacial displacement of the reduced-gravity model, and (b) contours of vertical velocity $-w_1$. The negative signs of the field variables are multiplied to show the flow pattern in the abyssal layer. The current speed is proportional to the length of a vector arrow, where the speed corresponding to an arrow as long as the zonal width of the basin in the figure is 4.0×10^{-1}cm s^{-1}. The contour intervals are (a) 4.10×10^{2}cm and (b) 1.93×10^{-4}cm s^{-1}. The contours the absolute value of which are larger than (a) 50% and (b) 1% of the maxima are omitted. Dotted region denotes negative values. The number of the grids for zonal and meridional directions are N_x=96 and N_y=192, respectively. The zonal line at the center latitude shows the equator.

obtained by the direct method was confirmed to satisfy the mass balance in the basin almost exactly within the round-off error:

$$H \oint u_\perp ds = -\lambda \int_S \eta dx dy + \int_S D\tilde{q}\, dx dy, \tag{3.59}$$

where ds is a line element along the coast and $u_\perp$ the velocity component perpendicular to the coast.

3.3.3 *Nonuniform grid spacing*

Close to the coast and the equator, the spatial scale of the circulation is smaller than that in the interior. The grid size therefore needs to be small to resolve these boundary layers. To examine the sensitivity to the grid resolution, the upwelling field of the first vertical mode was calculated for two different grid resolutions: 32×64 and 48×96, where the grid points are distributed uniformly. The conditions are the same as in the previous subsection (Table 3.1) except for the grid size. In the coarser resolution (Fig. 3.3a), we find alternating spike-like distributions of upwelling and downwelling at high latitudes along the zonal boundaries, while no such distribution is observed in the result of the finer resolution (Fig. 3.3b). This spurious downwelling is due to the insufficient resolution of boundary layers adjacent to the coast at high latitudes.

To gain a better resolution with a small number of grids, we rearranged the grid locations in a *nonuniform* way as

$$x_i = \frac{X_w}{N_x}\left\{1 - a\cos\left(\frac{2\pi}{N_x} i\right)\right\}, \qquad y_j = \frac{Y_w}{N_y}\left\{1 - a\cos\left(\frac{4\pi}{N_y} j\right)\right\}, \tag{3.60}$$

where x_i is the x-coordinate of the ith u point, y_j is the y-coordinate of the jth v point, and a=0.5, respectively. Note that the grid points are distributed dense along the boundaries and along the equator. As the abrupt change of the grid size degrades the accuracy of the difference equation (Fiadeiro and Veronis, 1977), the grid size was designed to vary smoothly. The result obtained with (32×64) grid points is shown in Fig. 3.3(c). Though the number of the grids is the same as that in Fig. 3.3(a), spurious spikes disappear and the downwelling field is found to be essentially the same as that of Fig. 3.3(b). Thus it turns out possible to attain a better resolution by means of nonuniform grid spacing, even without increasing the total number of the grid points. This is a great advantage of the direct method in comparison with the conventional method of time integration; computation time does not depend on the smallest grid size in the former method, whereas it does in the latter method on account of numerical stability.

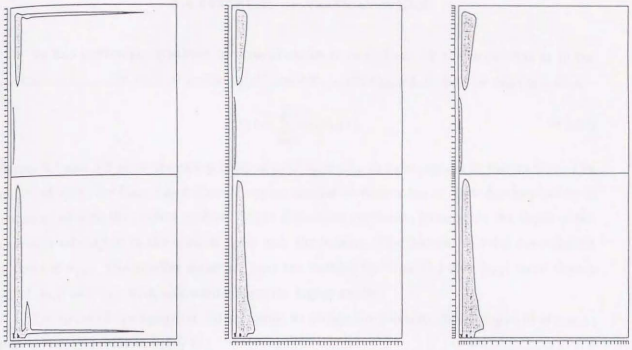

Fig. 3.3: The vertical velocity field for different configurations of the grids: (a) 32×64 uniform grids, (b) 48×96 uniform grids, and (c) 32×64 non-uniform grids. The other parameters are the same as those of Fig. 3.2. See the text for the definition of the non-uniform grid spacing. Dotted region denotes negative values and tickmarks show the spacing of the grid boxes.

3.4 SYNTHESIS OF VERTICAL MODES

In this section the synthesis of vertical modes is carried out for the circulation as in the previous section. The vertical profile $v_f(z)$, however, is generalized to take an arbitrary form

$$v_f(z) = \sum_{n=0}^{\infty} v_{f,n} \hat{v}_n(z). \tag{3.61}$$

Figures 3.4 and 3.5 show the two profiles of $v_f(z)$ and $v_{f,n}$ to be examined in this section. The profiles of $v_f(z)$ for Case I and Case II appear similar to each other in that the deep inflow is compensated with the surface outflow. Slight differences are found, however, in the depth of the maximum velocity or in the vertical shear near the bottom. The features of $v_f(z)$ are reflected on those of $v_{f,n}$. The smaller structure near the bottom for Case II yields $|v_{f,2}|$ more than a half of $|v_{f,1}|$ and $v_{f,n}$ with alternating signs for higher modes.

By virtue of the linearized formulation, we obtain the solution, for example, of $u(x, y, z)$ to an arbitrary profile of $v_f(z)$ as

$$u(x, y, z) = \sum_{n=0}^{\infty} v_{f,n} \hat{u}_n(x, y) \hat{u}_n(z). \tag{3.62}$$

Here $\hat{u}_n(z)$ is the basis function expressed by a cosine function (3.33), and $\hat{u}_n(x, y)$ represents the *basic response* of the u_n when $v_f(z) = \hat{v}_n(z)$. This formula implies that the three-dimensional structure is understood when we know $\{v_{f,n}\}$ and $\hat{u}_n(x, y)$. We therefore see first how the basic responses vary with the mode number, before proceeding to the procedure of mode analysis.

3.4.1 *The basic response of each mode*

Figures 3.2, 3.6, 3.7, and 3.8 show the basic responses for the first, second, fourth, and seventh mode, respectively: (a) the interfacial displacement $(-1)^n \hat{\eta}_n(x, y)$ and the velocity vector $(-1)^n(\hat{u}_n(x, y), \hat{v}_n(x, y))$ and (b) vertical velocity $(-1)^n \hat{w}_n$, where each variable is multiplied by $(-1)^n$ to express the field in the bottom layer.

We see that higher modes respond differently from the first mode in several ways. The southern hemisphere is dominated by an equatorward western boundary current which is extremely wide at high latitudes. Deep water downwells and flows westward in this broad area of the equatorward current. The stagnation point of the western boundary current retreats northward, whereas it is located at the middle latitude of the northern basin for the first mode. In the interior region of the northern hemisphere, current remains eastward and poleward, but generates only a feeble signal. In general, upwelling and current become weaker and tends to be concentrated along the coastal boundaries or the equator to make a narrow jet, as the diffusivity increases with the mode number.

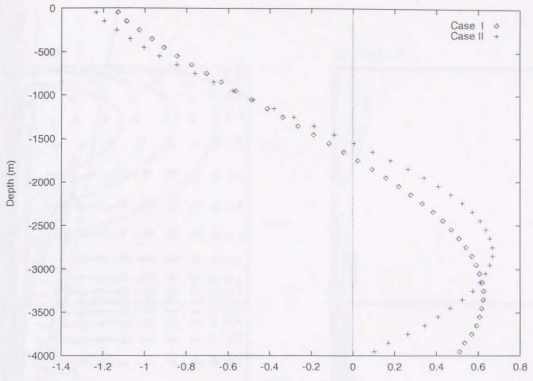

Fig. 3.4: Vertical profiles of the inflow $v_f(z)$ at the southern inlet region for Case I and Case II.

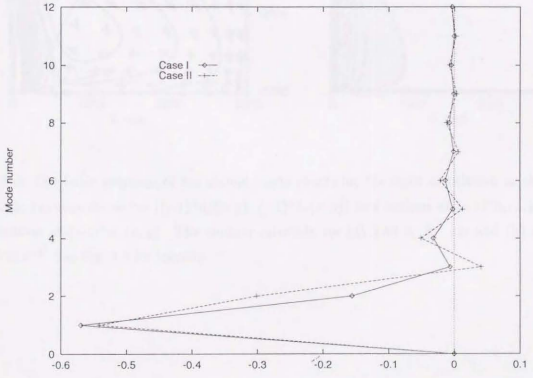

Fig. 3.5: The modes $v_{f,n}$ against the mode number for the two vertical profiles shown in Fig. 3.4.

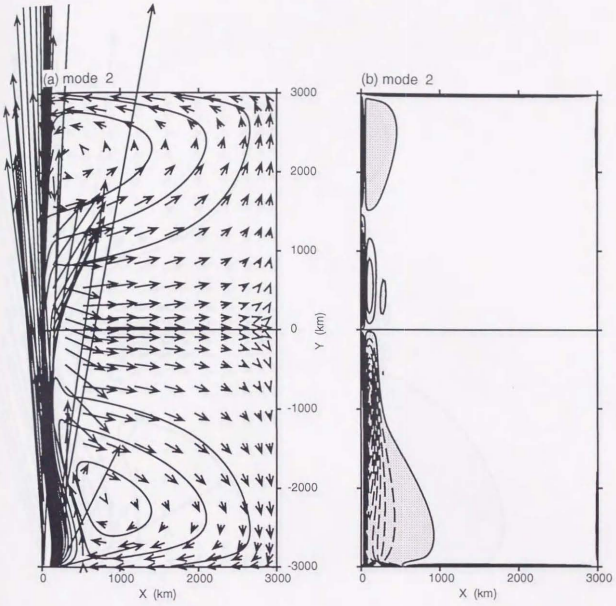

Fig. 3.6: The basic response of the second mode (n=2) for the same circulation as those in Fig. 3.2: (a) velocity vector ($(-1)^n \hat{u}_n(x,y)$, $(-1)^n \hat{v}_n(x,y)$) and contour of $(-1)^n \hat{\eta}_n(x,y)$, and (b) contour of $(-1)^n \hat{w}_n(x,y)$. The contour intervals are (a) 1.56 × 10^3 cm and (b) 2.04 × 10^{-4}cm s^{-1}. See Fig. 3.2 for legends.

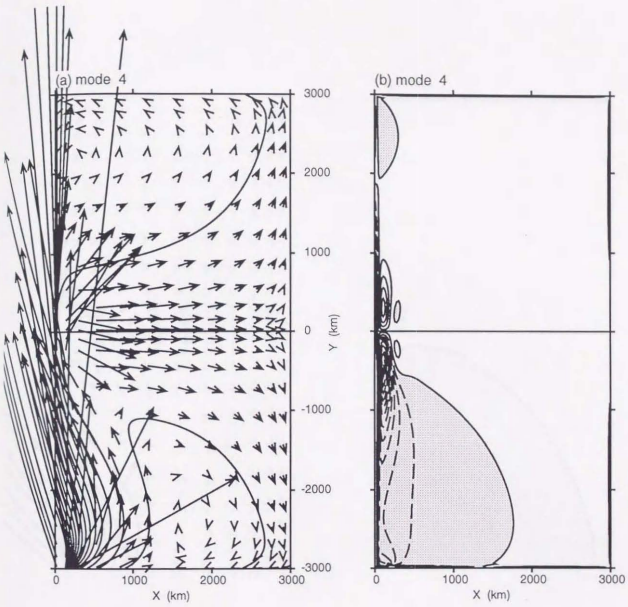

Fig. 3.7: The same as Fig. 3.6 except that $n = 4$. The contour intervals are (a) 6.90×10^3cm and (b) 2.37×10^{-4}cm s^{-1}. See Fig. 3.2 for legends.

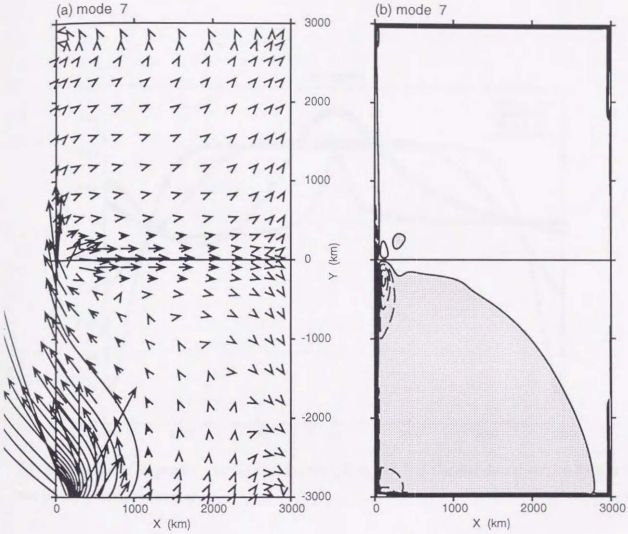

Fig. 3.8: The same as Fig. 3.6 except that $n = 7$. The contour intervals are (a) 1.51×10^4cm and (b) 2.02×10^{-4}cm s^{-1}. See Fig. 3.2 for legends.

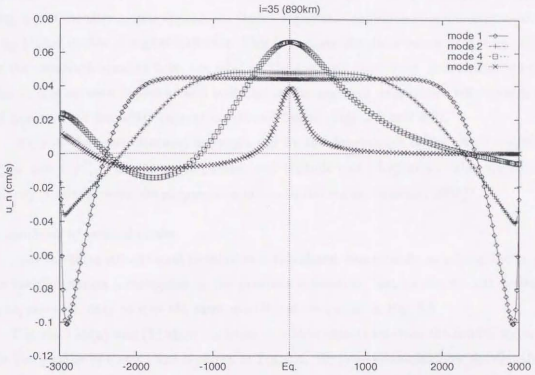

Fig. 3.9: The basic response $(-1)^n \hat{u}_n(x, y)$ for n=1, 2, 4, and 7 at the meridional section 890km east of the western boundary.

Characteristics of the basic responses of modes are observed more clearly in Fig. 3.9, which displays the meridional distribution of the zonal velocity $(-1)^n \hat{u}_n$ for the same modes as above along the section 890km east of the western boundary. We see that the first mode follows the Stommel-Arons scheme, in which a uniform interior eastward flow is accompanied by westward narrow counter currents along the southern and northern boundaries. As the mode number increases, this interior eastward flow tends to be confined within low latitudes, keeping a meridionally symmetric profile there. Significant meridional asymmetry is observed only for higher modes at higher latitudes. This is because the disturbance decays equatorward along the western boundary from the inlet on the southern boundary. A westward current of the fourth and seventh modes at mid latitudes in the southern hemisphere corresponds to the broad equatorward boundary current mentioned before (Figs. 3.7 and 3.8).

Many of the above features are explained by the dependence of the effective diffusivity $f^2/c_n^2\kappa_H$ and $f^2/c_n^2\lambda_n$ on the mode number and latitude (see Chapter 2). Also the equatorial singularity is related with the propagation of equatorial waves (Kawase, 1987).

3.4.2 *Synthesis of vertical modes*

Now the three-dimensional circulation is calculated immediately as a weighted synthesis of the basic responses investigated in the previous subsection. Let us restrict our preliminary analysis, however, only to u at the same meridional section as in Fig. 3.9.

Figures 3.10(a) and (b) show contours of u thus calculated from the modes up to n=18 for the two profiles of Cases I and II shown in Fig. 3.4. We briefly examine how the distributions of u are realized from the viewpoint of the multi-mode model. Dominated by the first baroclinic mode, both circulations have rather uniform eastward flow in deep layers and the opposite flow in surface layers. The counter boundary currents are found along the northern and southern coasts at all depths. Higher modes contribute to break the vertical antisymmetry due to the first mode. The second mode enhances (reduces) the surface westward (deep eastward) current and induces an eastward flow near the mid-depth of 2000m, at which lie the node of the first mode and an antinode of the second mode. In consequence, u vanishes at the depth of 1760m (1520m) and takes a maximum velocity at the depth of 2480m (3120m) for Case I (II) of larger (smaller) $|v_{f,2}|/|v_{f,1}|$. Other higher modes may have substantial influences on u in some regions, though each of them is quite small in magnitude. Such an example is found in the poleward ascending of the depth of the maximum u around the equator. The rapid decay of higher modes away from the equator is responsible for it.

We have seen that even these simplest circulations governed by the linearized dynamics can produce a complicated three-dimensional structure and that a slight change of the driving force, represented by the profile of the inflow here, may significantly alter the resulting circu-

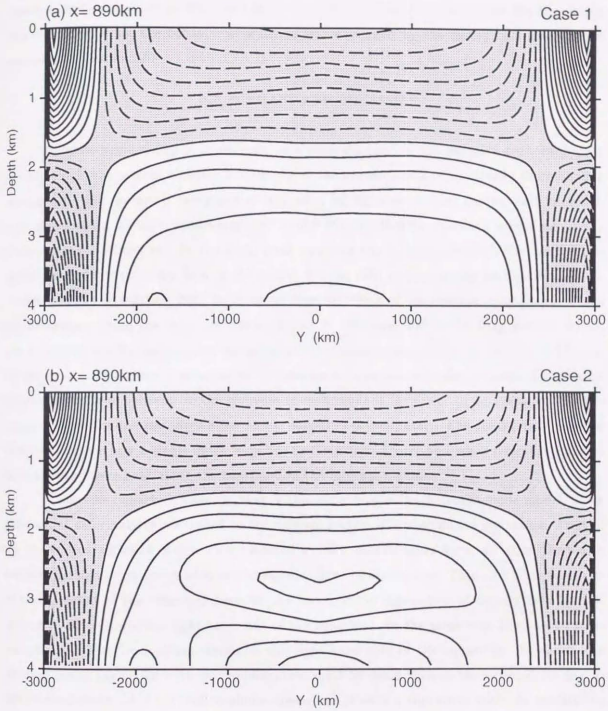

Fig. 3.10: Contours of zonal velocity at the meridional section 890km east of the western boundary obtained from the superposition of modes 1 to 18 for (a) Case 1 and (b) Case 2, respectively. Dotted region denotes the westward current. The maximum/minimum values and the contour intervals in the unit of cm s^{-1} are (a) 9.05×10^{-2}/-7.50×10^{-2}, 6.03×10^{-3} and (b) 9.36×10^{-2}/-6.55×10^{-2}, 6.24×10^{-3}, respectively.

lations in some regions. It has been shown, however, many characteristics of and differences between the two circulations examined here can be understood if we decompose the circulation into diffusive modes, the behavior of which is well explained by the theory of a single mode described in Chapter 2.

3.5 SUMMARY AND DISCUSSION

A multi-mode model is introduced as a generalization of the diffusive reduced-gravity model, which was used in Chapter 2 for studying the gravest mode of the steady thermohaline circulation. The former is composed of a number of diffusive vertical modes, each of which corresponds to a diffusive reduced-gravity model with coefficients specified according to the mode number. In contrast to the multi-level model or the ordinary OGCM, the multi-mode model views the circulation field in the modal domain with respect to the vertical dimension. It expands the circulation field in terms of eigenfunctions of the vertical coordinate, which are determined from the basic stratification just in the same way as for long gravity waves. For a vertical mode, independent variables are the horizontal coordinates (x,y), not (x,y,z). Moreover, a vertical mode is governed by shallow-water equations with the diffusion of interfacial displacement. The behavior or the response of each mode is far easier to understand than the original three-dimensional circulation as an output of a computer. The reader may refer to Chapter 2 to see how a single mode responds to the external force and what structure appears in boundary layers both along the coast and in the internal region.

It must be remarked, however, that in this simplification to the multi-mode model, a few substantial deformations are added to the original system of the primitive equations. First of all, the vertical diffusion of density is modified to have an unfamiliar form, although there also remains ambiguity on the validity of the familiar form of dissipation. This alteration forces us to take account of the difference between the two forms of dissipation of density as a kind of forcing to the system (the right-hand side of the equation). In the same way, the linearization necessarily shifts the nonlinear terms to the right-hand side of the equations. In short, the residual terms associated with this modification must be dealt with as the external forcing to the vertical mode. If the system is almost linear and if we are concerned with the qualitative understanding of the ocean general circulation, however, those apparent forcing may partly be dealt with in an iterative way.

The steady solutions to higher modes are difficult to obtain if we rely on an ordinary method of time integration. This is because higher modes have narrower widths of boundary layers, which requires a finer spatial resolution and in turn demands a smaller time step for the CFL condition to be satisfied. It therefore is inefficient or inadequate to use the ordinary

method in order to obtain the response of higher modes. On the other hand, the time constant for lower modes becomes as large as $O(10^5$ days) so that it takes enormous computation time to obtain the steady state precisely. In order for the multi-mode model to be available, however, it is indispensable to efficiently compute the response of the lowest to higher modes. We thus develop a direct method for the steady solution of the diffusive vertical mode. The underlying idea is the same as the factorization method (Peyret and Taylor, 1983) with an important difference that each element of the matrix for the appropriate equation is a matrix itself in the present problem, while it is a number in cases such as Masuda and Uehara (personal communication) for the quasi-geostrophic dynamics.

This method is then applied to the calculation of the thermohaline circulation in an ocean similar to the Pacific, which is driven by the inflow of the deep water near the southwestern boundary in the southern hemisphere. The direct method is confirmed to be efficient and precise in comparison with the conventional procedure of time integration to obtain the steady state. Also the same circulation is used to illustrate how multiple vertical modes are synthesized to build up the three-dimensional structure. First, characteristic responses of the lowest to higher modes are argued in terms of the dynamics of a single mode. Then, higher modes are shown to modify the circulation dominated by the first mode. In particular, it turns out that even an apparently slight difference of driving force may cause a significant alteration of the circulation near the equator or the western boundary.

In this article, we concentrate ourselves on the conceptual and numerical preparation, which themselves we believe are of scientific and technical significance. Hence the situations tested here are idealistic ones, such as the linear stratification or horizontally uniform inflows in a flat rectangular basin. In Chapter 4, we will apply the multi-mode model and the direct method for solving the steady state of the diffusive vertical mode to thermohaline circulation. A new viewpoint and interpretation based on the diffusive vertical mode will be addressed there in more detail, by comparing the multi-mode synthesis with the experiment carried out with a multi-level model (ordinary OGCM).

REFERENCES

Bryan, K., 1969: A numerical method for the study of the circulation of the World Ocean. *J. Comput. Phys.*, **4**, 347–376.

Fiadeiro, M. E. and Veronis, G., 1977: On weighted-mean schemes for the finite-difference approximation to the advection-diffusion equation. *Tellus*, **29**, 512–522.

Kawase, M., 1987: Establishment of mass-driven abyssal circulation. *J. Phys. Oceanogr.*, **17**, 2294–2317.

Krauss, W., 1966: Interne Wellen. Methoden und Ergebnisse der Theroetischen Ozeanographie, Band II. Gebrüder Borntraeger, 248pp.

Kubota, M., and H. Ono, 1992: Abyssal circulation model of the Philippine Sea. *Deep-Sea Res.*, **39**, 1439–1452.

Masuda, A., and G. Mizuta, 1995: A study on the effects of bottom topography on deep circulation with a diffusive reduced-gravity model. *J. Phys. Oceanogr.*, **25**, 374–390.

McCreary, J. P., 1981: A linear stratified model of the Equatorial Undercurrent. *Phil. Trans. R. Soc. Lond.*, **A298**, 603–635.

Mesinger, F., and A. Arakawa, 1976: Numerical methods used in atmospheric models. GARP publication series, 17, 64pp.

Pedlosky, J., 1992: The Baroclinic Structure of the Abyssal Circulation. *J. Phys. Oceanogr.*, **22**, 652–659.

Peyret, R., and Taylor, T. D., 1983: Computational Methods for Fluid Flow. Springer-Verlag, 358pp.

Stommel, H. and A. B. Arons, 1960: On the abyssal circulation of a world ocean—II. An idealized model of the circulation pattern and amplitude in oceanic basins. *Deep-Sea Res.*, **6**, 217–244.

Talley, L., 1979: Steady two-layer source-sink flow. 1979 Summer Study Program in Geophysical Fluid Dynamics at the Woods Hole Oceanographic Institution: Notes on Polar Oceanography, Vol. 2, Woods Hole Oceanogr. Inst., 97–118.

Wajsowicz, R. C., and A. E. Gill, 1986: Adjustment of the Ocean under Buoyancy Forces. Part I: The Role of Kelvin Waves. *J. Phys. Oceanogr.*, **16**, 2097–2114.

Warren, B. A., 1983: Why is no deep water found in the North Pacific? *J. Mar. Res.*, **41**, 327–347.

APPENDIX 3.A TRANSFORM FROM PHYSICAL VARIABLES TO MODE VARIABLES

$$p_n = \frac{\int_{-D}^{0} \hat{p}_n (p'/\rho_c) dz}{\int_{-D}^{0} \hat{p}_n \hat{p}_n dz} = \frac{1}{D} \int_{-D}^{0} \hat{p}_n (p'/\rho_c) dz, \tag{3.A.1}$$

$$u_n = \frac{\int_{-D}^{0} \hat{u}_n u dz}{\int_{-D}^{0} \hat{u}_n \hat{u}_n dz} = \frac{1}{D} \int_{-D}^{0} \hat{u}_n u dz = \frac{1}{D} \int_{-D}^{0} \hat{p}_n u dz, \tag{3.A.2}$$

$$v_n = \frac{\int_{-D}^{0} \hat{v}_n v dz}{\int_{-D}^{0} \hat{v}_n \hat{v}_n dz} = \frac{1}{D} \int_{-D}^{0} \hat{v}_n v dz = \frac{1}{D} \int_{-D}^{0} \hat{p}_n v dz, \tag{3.A.3}$$

$$\begin{aligned} w_n &= \frac{\int_{-D}^{0} N^2 \hat{w}_n w dz}{\int_{-D}^{0} N^2 \hat{w}_n \hat{w}_n dz} = \frac{\int_{-D}^{0} N^2 \hat{w}_n w dz}{c_n^4 / D^2 \left\{ [\hat{p}_n / N^2 \cdot d\hat{p}_n / dz]_{-D}^{0} + 1/c_n^2 \int_{-D}^{0} \hat{p}_n \hat{p}_n dz \right\}} \\ &= -\int_{-D}^{0} \frac{d\hat{p}_n}{dz} w dz = \frac{g}{c_n^2} \int_{-D}^{0} \hat{p}_n w dz, \end{aligned} \tag{3.A.4}$$

$$\begin{aligned} \rho_n &= \frac{\int_{-D}^{0} \frac{1}{N^2} \hat{p}_n (\rho'/\rho_c) dz}{\int_{-D}^{0} \frac{1}{N^2} \hat{p}_n \hat{p}_n dz} = \frac{g^2}{c_n^2 D} \int_{-D}^{0} \frac{\hat{p}_n}{N^2} (\rho'/\rho_c) dz \\ &= -\frac{g}{D} \int_{-D}^{0} \frac{1}{N^2} \frac{d\hat{p}}{dz} (\rho'/\rho_c) dz = \frac{1}{\rho_c D} \int_{-D}^{0} \frac{1}{N^2} \frac{d\bar{p}}{dz} \frac{\partial p'}{\partial z} dz \\ &= \frac{1}{D} \left[\frac{1}{N^2} \frac{d\hat{p}_n}{dz} (p'/\rho_c) \right]_{-D}^{0} + \frac{1}{c_n^2 D} \int_{-D}^{0} \hat{p}_n (p'/\rho_c) dz = \frac{1}{c_n^2} p_n, \end{aligned} \tag{3.A.5}$$

$$q_n = \frac{\int_{-D}^{0} \hat{q}_n q dz}{\int_{-D}^{0} \hat{q}_n \hat{q}_n dz} = \frac{1}{D} \int_{-D}^{0} \hat{u}_n q dz = \frac{1}{D} \int_{-D}^{0} \hat{p}_n q dz, \tag{3.A.6}$$

$$F_n^x = \frac{\int_{-D}^{0} \hat{F}_n^x F^x dz}{\int_{-D}^{0} \hat{F}_n^x \hat{F}_n^x dz} = \frac{1}{D} \int_{-D}^{0} \hat{F}_n^x F^x dz = \frac{1}{D} \int_{-D}^{0} \hat{p}_n F^x dz, \tag{3.A.7}$$

$$F_n^y = \frac{\int_{-D}^{0} \hat{F}_n^y F^y dz}{\int_{-D}^{0} \hat{F}_n^y \hat{F}_n^y dz} = \frac{1}{D} \int_{-D}^{0} \hat{F}_n^y F^y dz = \frac{1}{D} \int_{-D}^{0} \hat{p}_n F^y dz, \tag{3.A.8}$$

$$Q_n = \frac{\int_{-D}^{0} \frac{1}{N^2} \hat{Q}_n (Q/\rho_c) dz}{\int_{-D}^{0} \frac{1}{N^2} \hat{Q}_n \hat{Q}_n dz} = \frac{g^2}{c_n^2 D} \int_{-D}^{0} \frac{\hat{\rho}_n}{N^2} \frac{Q}{\rho_c} dz. \tag{3.A.9}$$

APPENDIX 3.B DEFINITIONS OF MATRICES $\boldsymbol{P}_j$, $\boldsymbol{Q}_j$, $\boldsymbol{R}_j$, AND VECTOR $\boldsymbol{q}_j$

We first define the grid spacing $\triangle_i^x$ and $\triangle_j^y$ as in Fig. 3.1 for $1 \le i \le N_x$ and $1 \le j \le N_y$, respectively. For the convenience of notation, we put

$$\triangle_0^x = \triangle_{N_x+1}^x = \triangle_0^y = \triangle_{N_y+1}^y = 0, \tag{3.A.10}$$

$$\triangle_i^{x*} = \begin{cases} \triangle_1^x & (i=0), \\ \triangle_i^x & (1 \le i \le N_x), \\ \triangle_{N_x}^x & (i=N_x+1), \end{cases} \tag{3.A.11}$$

and

$$\triangle_j^{y*} = \begin{cases} \triangle_1^y & (j=0), \\ \triangle_j^y & (1 \le j \le N_y), \\ \triangle_{N_y}^y & (j=N_y+1). \end{cases} \tag{3.A.12}$$

Then the other auxiliary parameters, vectors, and matrices are defined as follows:

scalar parameters are

$$\begin{cases} \alpha_i^x = \dfrac{\Delta_{i+1}^x}{\Delta_i^x + \Delta_{i+1}^x}, & \beta_i^x = \dfrac{2}{\Delta_i^x + \Delta_{i+1}^x}, \\ \alpha_j^y = \dfrac{\Delta_{j+1}^y}{\Delta_j^y + \Delta_{j+1}^y}, & \beta_j^y = \dfrac{2}{\Delta_j^y + \Delta_{j+1}^y}, \end{cases} \tag{3.A.13}$$

$$\begin{cases} a_i^{x+} = \dfrac{2}{\Delta_{i+1}^x(\Delta_i^x + \Delta_{i+1}^x)}, & a_i^{x0} = -\dfrac{2}{\Delta_i^x \Delta_{i+1}^x}, & a_i^{x-} = \dfrac{2}{\Delta_i^x(\Delta_i^x + \Delta_{i+1}^x)}, \\ a_j^{y+} = \dfrac{2}{\Delta_j^y(\Delta_j^y + \Delta_{j+1}^y)}, & a_j^{y0} = -\left(a_j^{y+} + a_j^{y-}\right), & a_j^{y-} = \dfrac{2}{\Delta_j^y(\Delta_{j-1}^y + \Delta_j^y)}, \end{cases} \tag{3.A.14}$$

$$\begin{cases} b_i^{x+} = \dfrac{2}{\Delta_i^x(\Delta_i^x + \Delta_{i+1}^x)}, & b_i^{x0} = -\left(b_i^{x+} + b_i^{x-}\right), & b_i^{x-} = \dfrac{2}{\Delta_i^x(\Delta_{i-1}^x + \Delta_i^x)}, \\ b_j^{y+} = \dfrac{2}{\Delta_{j+1}^y(\Delta_j^y + \Delta_{j+1}^y)}, & b_j^{y0} = -\dfrac{2}{\Delta_j^y \Delta_{j+1}^y}, & b_j^{y-} = \dfrac{2}{\Delta_j^y(\Delta_j^y + \Delta_{j+1}^y)}, \end{cases} \tag{3.A.15}$$

$$\begin{cases} c_i^{x+} = \dfrac{2}{\Delta_i^{x*}(\Delta_i^{x*} + \Delta_{i+1}^{x*})}, & c_i^{x0} = -\left(b_i^{x+} + b_i^{x-}\right), & c_i^{x-} = \dfrac{2}{\Delta_i^{x*}(\Delta_{i-1}^{x*} + \Delta_i^{x*})}, \\ c_j^{y+} = \dfrac{2}{\Delta_{j+1}^{y*}(\Delta_j^{y*} + \Delta_{j+1}^{y*})}, & c_j^{y0} = -\dfrac{2}{\Delta_j^{y*} \Delta_{j+1}^{y*}}, & c_j^{y-} = \dfrac{2}{\Delta_j^{y*}(\Delta_j^{y*} + \Delta_{j+1}^{y*})}, \end{cases} \tag{3.A.16}$$

where $1 \leq i \leq N_x$ and $1 \leq j \leq N_y$;

column vectors are

$$\boldsymbol{u}_b^p = {}^t(a_1^{x-} u_{0,j}, 0, \cdots, 0, a_{N_x-1}^{x+} u_{N_x,j}), \tag{3.A.17}$$

$$\boldsymbol{v}_b = {}^t(b_1^{x-} v_{0,j}, 0, \cdots, 0, b_{N_x}^{x+} v_{N_x,j}), \tag{3.A.18}$$

$$\boldsymbol{u}_b^0 = {}^t(\alpha_j^y u_{0,j}/2, 0, \cdots, 0, \alpha_j^y u_{N_x,j}), \tag{3.A.19}$$

$$\boldsymbol{u}_b^+ = {}^t((1-\alpha_j^y) u_{0,j+1}/2, 0, \cdots, 0, (1-\alpha_j^y) u_{N_x,j+1}/2), \tag{3.A.20}$$

$$\boldsymbol{u}_b^m = {}^t(-u_{0,j}/\Delta_1^x, 0, \cdots, 0, u_{N_x,j}/\Delta_{N_x}^x); \tag{3.A.21}$$

matrices of the order $(N_x - 1) \times (N_x - 1)$ are

$$\boldsymbol{I}_u = \begin{pmatrix} 1 & & \\ & \ddots & \\ & & 1 \end{pmatrix}, \tag{3.A.22}$$

$$\boldsymbol{L}_u = \begin{pmatrix} a_1^{x0} & a_1^{x+} & & & \\ a_2^{x-} & a_2^{x0} & a_2^{x+} & & \\ & \ddots & \ddots & \ddots & \\ & & a_{N_x-2}^{x-} & a_{N_x-2}^{x0} & a_{N_x-2}^{x+} \\ & & & a_{N_x-1}^{x-} & a_{N_x-1}^{x0} \end{pmatrix}; \tag{3.A.23}$$

matrices of the order $(N_x-1)\times N_x$ are

$$\boldsymbol{A}_u = \begin{pmatrix} \alpha_1^x & 1-\alpha_1^x & & & \\ & \alpha_2^x & 1-\alpha_2^x & & \\ & & \ddots & \ddots & \\ & & & \alpha_{N_x-1}^x & 1-\alpha_{N_x-1}^x \end{pmatrix}, \tag{3.A.24}$$

$$\boldsymbol{G}_u = \begin{pmatrix} -\beta_1^x & \beta_1^x & & & \\ & -\beta_2^x & \beta_2^x & & \\ & & \ddots & \ddots & \\ & & & -\beta_{N_x-1}^x & \beta_{N_x-1}^x \end{pmatrix}; \tag{3.A.25}$$

matrices of the order $N_x\times(N_x-1)$ are

$$\boldsymbol{A}_v = \begin{pmatrix} 1 & & & \\ 1 & 1 & & \\ & \ddots & \ddots & \\ & & 1 & 1 \\ & & & 1 \end{pmatrix}, \tag{3.A.26}$$

$$\boldsymbol{G}_e = \begin{pmatrix} 1/\triangle_1^x & & & \\ -1/\triangle_2^x & 1/\triangle_2^x & & \\ & \ddots & \ddots & \\ & & -1/\triangle_{N_x-1}^x & 1/\triangle_{N_x-1}^x \\ & & & -1/\triangle_{N_x}^x \end{pmatrix}; \tag{3.A.27}$$

and matrices of the order $N_x\times N_x$ are

$$\boldsymbol{I}_v = \begin{pmatrix} 1 & & & & \\ & 1 & & & \\ & & 1 & & \\ & & & 1 & \\ & & & & 1 \end{pmatrix}, \tag{3.A.28}$$

$$\boldsymbol{L}_v = \begin{pmatrix} b_1^{x0} & b_1^{x+} & & & \\ b_2^{x-} & b_2^{x0} & b_2^{x+} & & \\ & \ddots & \ddots & \ddots & \\ & & b_{N_x-1}^{x-} & b_{N_x-1}^{x0} & b_{N_x-1}^{x+} \\ & & & b_{N_x}^{x-} & b_{N_x}^{x0} \end{pmatrix}, \tag{3.A.29}$$

$$\boldsymbol{L}_e = \begin{pmatrix} (c_1^{x-}+c_1^{x0}) & c_1^{x+} & & & \\ b_2^{x-} & b_2^{x0} & b_2^{x+} & & \\ & \ddots & \ddots & \ddots & \\ & & b_{N_x-1}^{x-} & b_{N_x-1}^{x0} & b_{N_x-1}^{x+} \\ & & & c_{N_x}^{x-} & (c_{N_x}^{x0}+c_{N_x}^{x+}) \end{pmatrix}. \tag{3.A.30}$$

Finally, we have

$$
\begin{cases}
\boldsymbol{P}_1 = \begin{pmatrix} -\nu_H a_j^{y+}\boldsymbol{I}_u & 0 & 0 \\ f_j^v \frac{1-\sigma_j^y}{2}\boldsymbol{A}_v & -\nu_H b_j^{y+}\boldsymbol{I}_v & g_n\beta_j^y\boldsymbol{I}_v \\ 0 & 0 & -\kappa_H c_j^{y+}\boldsymbol{I}_v \end{pmatrix} \\
\boldsymbol{Q}_1 = \begin{pmatrix} (*1) & -\frac{f_j^u}{2}\boldsymbol{A}_u & g_n\boldsymbol{G}_u \\ f_j^v\frac{\sigma_j^y}{2}\boldsymbol{A}_v & (*2) & -g_n\beta_j^y\boldsymbol{I}_v \\ H\boldsymbol{G}_e & \frac{H}{\Delta_j^y}\boldsymbol{I}_v & (*4) \end{pmatrix} \qquad (j=1), \quad \text{(3.A.31)} \\
\boldsymbol{q}_1 = \begin{pmatrix} \boldsymbol{F}_j^x + \nu_H \boldsymbol{u}_b^{y-} + (\nu_H a_j^{y-}\boldsymbol{u}_0) + \frac{f_j^u}{2}\boldsymbol{A}_u\boldsymbol{v}_0 \\ \boldsymbol{F}_j^y - f_j^v(\boldsymbol{u}_b^0 + \boldsymbol{u}_b^+) + (\nu_H\boldsymbol{v}_b) + \nu_H b_j^{y-}\boldsymbol{v}_0 \\ \boldsymbol{Q}_j - H\boldsymbol{u}_b^m + \frac{H}{\Delta_j^y}\boldsymbol{v}_0 \end{pmatrix}
\end{cases}
$$

$$
\begin{cases}
\boldsymbol{P}_j = \begin{pmatrix} -\nu_H a_j^{y+}\boldsymbol{I}_u & 0 & 0 \\ f_j^v \frac{1-\sigma_j^y}{2}\boldsymbol{A}_v & -\nu_H b_j^{y+}\boldsymbol{I}_v & g_n\beta_j^y\boldsymbol{I}_v \\ 0 & 0 & -\kappa_H a_j^{y+}\boldsymbol{I}_v \end{pmatrix} \\
\boldsymbol{Q}_j = \begin{pmatrix} (*1) & -\frac{f_j^u}{2}\boldsymbol{A}_u & g_n\boldsymbol{G}_u \\ f_j^v\frac{\sigma_j^y}{2}\boldsymbol{A}_v & (*2) & -g_n\beta_j^y\boldsymbol{I}_v \\ H\boldsymbol{G}_e & \frac{H}{\Delta_j^y}\boldsymbol{I}_v & (*3) \end{pmatrix} \qquad (j=2,\cdots,N_y-1), \quad \text{(3.A.32)} \\
\boldsymbol{R}_j = \begin{pmatrix} -\nu_H a_j^{y-}\boldsymbol{I}_u & -\frac{f_j^u}{2}\boldsymbol{A}_u & 0 \\ 0 & -\nu_H b_j^{y-}\boldsymbol{I}_v & 0 \\ 0 & -\frac{H}{\Delta_j^y}\boldsymbol{I}_v & -\kappa_H a_j^{y-}\boldsymbol{I}_v \end{pmatrix} \\
\boldsymbol{q}_j = \begin{pmatrix} \boldsymbol{F}_j^x + \nu_H \boldsymbol{u}_b^{y0} \\ \boldsymbol{F}_j^y - f_j^v(\boldsymbol{u}_b^0 + \boldsymbol{u}_b^+) + (\nu_H\boldsymbol{v}_b) \\ \boldsymbol{Q}_j - H\boldsymbol{u}_b^m \end{pmatrix}
\end{cases}
$$

$$
\begin{cases}
\boldsymbol{Q}_{N_y} = \begin{pmatrix} (*1) & -\frac{f_j^u}{2}\boldsymbol{A}_u & g_n\boldsymbol{G}_u \\ 0 & \boldsymbol{I}_v & 0 \\ H\boldsymbol{G}_e & \frac{H}{\Delta_j^y}\boldsymbol{I}_v & (*5) \end{pmatrix} \\
\boldsymbol{R}_{N_y} = \begin{pmatrix} -\nu_H a_j^{y-}\boldsymbol{I}_u & -\frac{f_j^u}{2}\boldsymbol{A}_u & 0 \\ 0 & 0 & 0 \\ 0 & -\frac{H}{\Delta_j^y}\boldsymbol{I}_v & -\kappa_H c_j^{y-}\boldsymbol{I}_v \end{pmatrix} \qquad (j=N_y), \qquad \text{(3.A.33)} \\
\boldsymbol{q}_{N_y} = \begin{pmatrix} \boldsymbol{F}_j^x + \nu_H \boldsymbol{u}_b^{y0} + (\nu_H a_j^{y+}\boldsymbol{u}_{j+1}) \\ \boldsymbol{v}_j \\ \boldsymbol{Q}_j - H\boldsymbol{u}_b^m \end{pmatrix}
\end{cases}
$$

where

$$
(*1) \;=\; \left(R_n - \nu_H a_j^{y0}\right)\boldsymbol{I}_u - \nu_H \boldsymbol{L}_u,
$$

$$
\begin{aligned}
(*2) &= \left(R_n - \nu_H b_j^{y0}\right) I_v - \nu_H L_v, \\
(*3) &= \left(\lambda_n - \kappa_H a_j^{y0}\right) I_v - \kappa_H L_e, \\
(*4) &= \left(\lambda_n - \kappa_H c_j^{y0}\right) I_v - \kappa_H L_e - \kappa_H c_j^{y-} I_v, \\
(*5) &= \left(\lambda_n - \kappa_H c_j^{y0}\right) I_v - \kappa_H L_e - \kappa_H c_j^{y+} I_v.
\end{aligned}
$$

Chapter 4

A view of thermohaline circulation based on the expansion in terms of diffusive vertical modes

Abstract

The three-dimensional structure of thermohaline circulations in two idealized situations was investigated with a multi-mode model (MMM) which expands the circulation field in terms of *diffusive* vertical modes and solves the steady response of each mode by a direct method developed in Chapter 3. The modes thus calculated are synthesized to yield the steady circulation to be compared with that achieved through time-integration with an ordinary multi-level model (MLM).

In the first experiment the ocean is driven by surface cooling localized near the center of the basin. The circulation realized by the MLM turned out to be reproduced well by the MMM synthesis where the response of modes to a simplified cooling *modeled* on convective adjustment was calculated. Moreover the response of each diffusive mode is explained well in terms of the dynamics of a single mode (Chapter 2). Thus, the three-dimensional structure of the circulation is understood as a composite of such diffusive vertical modes. The second circulation examined is driven by meridional differential cooling over the whole sea surface, yielding such a complicated three-dimensional field that simple decomposition into diffusive modes was of little use for dynamical interpretation. Nevertheless the result is understood well by resolving the circulation into component circulations each of which is driven by the thermal forcing in the region specified for the component: atmosphere-cooled convection in the northern basin, boundary-forced downwelling along the eastern boundary, and upwelling and downwelling along and near the western boundary. By virtue of the localization of the forcing, each component circulation is still explained as the synthesis of diffusive modes as well as in the first experiment. In particular, the MLM experiment was shown in good agreement with the MMM synthesis of the response to the distributed cooling near and along the northern boundary, where active convection takes place and boundary-forced sinking prevails. Thus, the circulation in the second experiment resembles that in the southern or southeastern basin in the first experiment.

4.1 INTRODUCTION

In recent years, ocean general circulation has been simulated in a vast amount of numerical experiments based on primitive OGCMs (ocean general circulation models) or multi-level models (abbreviated to MLMs); for example see Cox and Bryan (1984), Bryan (1987), or Semtner and Chervin (1992). The circulations thus computed, however, are never easy to interpret or to anticipate. This is probably because the MLM, straightforward and powerful, involves so many factors of the real ocean that each element physics tends to be masked. Moreover, the MLM provides little about the integrated dynamics, since the MLM describes the relations among *local* derivatives. Accordingly it is difficult to understand the fundamental mechanism that maintains the ocean general circulation only by means of the MLM.

We therefore have attempted a different approach: a diffusive reduced-gravity model describing a single vertical mode (Chapter 2), and a multi-mode model (abbreviated to an MMM) or the expansion of the three-dimensional field of circulation in terms of diffusive vertical modes (Chapter 3). In this framework, spatial field variables are transformed into vertical-mode variables to obtain equations that are similar to shallow-water equations. Because our vertical modes incorporate the diffusion of density, they are referred to as *diffusive* vertical modes. The governing equations of diffusive vertical modes turned out much more tractable and informative for dynamical argument.

Since the analysis of a single mode is the very basis for studying the dynamics from the viewpoint of the multi-mode model, let us outline below the principal results of Chapter 2, in which a single mode—the first baroclinic mode—was investigated to find how drastically the diffusion of density changes the distribution of upwelling and downwelling not only in coastal boundary layers but also in internal regions. This study succeeded in clarifying the apparently strange distribution of upwelling and downwelling in the abyssal layer, which distribution has been reported in primitive MLM experiments since early 1970s (Holland, 1971).

In Chapter 2, the *diffusive stretching* or the diffusion of the thickness term in potential vorticity was introduced for the analysis of a single mode. This notion, closely related with the diffusion of density, proved quite important in understanding the slow dynamics of the stratified ocean. The western boundary layer is classified into those of the *viscous* regime and the *diffusive* regime. In the former regime, viscosity determines the width of the boundary layer, which is accompanied by recirculation just as the Munk layer. In contrast, the latter regime is dominated by horizontal diffusion of density to have wider boundary layers without recirculation. Similar regimes are found also in the internal boundary layer. The effective magnitude of density diffusion relative to the β effect increases with the Coriolis parameter, but decreases with increasing phase speed c of long gravity waves for the corresponding mode. These

notions were applied successfully to a surface current as well. In his numerical experiment, Yoon (1992) explained the seasonal variation of characteristic features of the East Korean Current as the alternation of the two regimes of the western boundary layer; the current flows narrow accompanied by recirculation in summer but it becomes much wider without recirculation in winter when c is small owing to weaker stratification. Also effects of variable topography on the abyssal circulation were investigated in the framework of the diffusive single mode by Masuda and Mizuta (1995), who showed how the diffusion of mass and the horizontal viscosity control the current above a *geostrophic* island, over which geostrophic contours close on themselves.

Thus even the study of a single mode greatly helps us understand the mechanism of thermohaline circulation. The three-dimensional structure, however, cannot be made clear by a single mode, but must be analyzed by the synthesis of many vertical modes. That is, we need to advance one step further toward the multi-mode model (MMM). In this paper we intend to understand the dynamics of thermohaline circulation from the viewpoint of the MMM. For that purpose, we first carry out ordinary numerical experiments based on a multi-level model (MLM) for two kinds of simple but typical thermohaline forcing: surface cooling localized near the center of the basin and meridional differential cooling over the whole area. The experiments provide us with *truths* of the model ocean described in OGCM codes. Next, the MMM computes the steady responses of vertical diffusive modes (i.e., in the modal domain) by use of the direct method developed in Chapter 3. The vertical modes are then synthesized to give the circulation in the physical domain. The results of the MMM are compared with the three-dimensional structure realized in the MLM experiments. It is to be noted that the present linearized MMM does not calculate nonlinear processes such as the basic stratification or the formation of deep water. Instead the MMM assumes them or deals with them as data from the MLM experiment. The specified purpose of the MMM is to understand the fundamental dynamics of thermohaline circulation with those processes provided as a black box or external conditions.

The next section outlines formulation, experimental conditions for the MLM, and analyzing procedures for the MMM. The third section examines the thermohaline circulation driven by surface cooling localized near the center of the basin. The subject of the section is how the three-dimensional response to surface localized cooling is understood as the synthesis of many vertical modes. The fourth section analyzes the second example of thermohaline circulation which is driven by the meridional differential cooling on the sea surface. The circulation is far more complicated than the first because effective forcing is not concentrated but distributed thin and wide. The fourth section is intended to show how the response to spatially distributed forcing is decomposed into responses to forcing of various physical origins and geographical locations. A summary and discussion are given in the last section.

4.2 FORMULATIONS AND EXPERIMENTAL PROCEDURES

Simpler situations are preferred for our purpose of understanding the fundamental mechanism of thermohaline circulation. The Boussinesq and hydrostatic assumptions are made first. We disregard the contribution of salinity to density and assume a linear relation between the perturbed temperature and the perturbed density. In addition we consider a rectangular flat ocean on a β-plane where local Cartesian coordinates are available. Moreover only the steady slow circulation is discussed to avoid the complication due to mesoscale eddies. Accordingly coarse horizontal grids are adopted along with rather large values for viscosity and diffusivity. Finally we restrict ourselves to purely thermohaline circulation which is driven only by the surface body cooling.

4.2.1 *Basic equations for the MLM experiment*

Under the conditions mentioned above, the primitive equations are written as

$$\frac{\partial u}{\partial t} + u\frac{\partial u}{\partial x} + v\frac{\partial u}{\partial y} + w\frac{\partial u}{\partial z} - fv = -\frac{1}{\rho_c}\frac{\partial p}{\partial x} + \frac{\partial}{\partial z}\left(\nu_V \frac{\partial u}{\partial z}\right) + \nabla_H \cdot (\nu_H \nabla_H u), \tag{4.1}$$

$$\frac{\partial v}{\partial t} + u\frac{\partial v}{\partial x} + v\frac{\partial v}{\partial y} + w\frac{\partial v}{\partial z} + fu = -\frac{1}{\rho_c}\frac{\partial p}{\partial y} + \frac{\partial}{\partial z}\left(\nu_V \frac{\partial v}{\partial z}\right) + \nabla_H \cdot (\nu_H \nabla_H v), \tag{4.2}$$

$$0 = -\frac{\partial p}{\partial z} - g\rho, \tag{4.3}$$

$$\frac{\partial u}{\partial x} + \frac{\partial v}{\partial y} + \frac{\partial w}{\partial z} = 0, \tag{4.4}$$

$$\frac{\partial \rho}{\partial t} + u\frac{\partial \rho}{\partial x} + v\frac{\partial \rho}{\partial y} + w\frac{\partial \rho}{\partial z} = \frac{\partial}{\partial z}\left\{(\kappa_{ca} + \kappa_V)\frac{\partial \rho}{\partial z}\right\} + \nabla_H \cdot (\kappa_H \nabla_H \rho) + Q_{body}, \tag{4.5}$$

where (x, y, z) are the (eastward, northward, upward) coordinates with origins at the (western boundary, equator, surface), (u, v, w) the corresponding velocity components, t time, ∇_H the horizontal gradient operator, p pressure, ρ density, ρ_c the characteristic density, Q_{body} the body cooling, g the acceleration due to gravity, $f = \beta y$ the Coriolis parameter with a constant β, (ν_H, ν_V) the (horizontal, vertical) viscosity of momentum, and (κ_H, κ_V) the (horizontal, vertical) diffusion of density. Unstable stratification in numerical experiments is resolved by convective adjustment, which is represented symbolically by

$$\kappa_{ca} = \begin{cases} \infty & (\frac{\partial \rho}{\partial z} > 0) \\ 0 & (\text{otherwise}) \end{cases} \tag{4.6}$$

in the equation of density.

On side boundaries both current and density flux must vanish:

$$(u, v) = (0, 0), \qquad \frac{\partial \rho}{\partial n} = 0, \tag{4.7}$$

where $\partial/\partial n$ denotes the derivative along the outward normal. At the sea surface, we put a rigid lid, disregard the wind stress, and allow no diffusion of density. The similar conditions hold at the bottom. Accordingly we have

$$w = 0, \qquad \frac{\partial(u,v)}{\partial z} = (0,0), \qquad \frac{\partial \rho}{\partial z} = 0 \tag{4.8}$$

either at the surface or at the bottom.

The only external force driving the circulation comes from the surface cooling of Haney type. This parametrization defines the body cooling by

$$Q_{body} = \begin{cases} -\alpha\,(\rho - \rho_{ref}) & (\text{ in the top layer }) \\ 0 & (\text{ otherwise }), \end{cases} \tag{4.9}$$

where $\rho_{ref}(x,y)$ is the reference density at the sea surface to be specified in each experiment and $1/\alpha$ denotes the relaxation time for the surface cooling.

4.2.2 *Experimental conditions*

Two experiments are presented here: Experiment I drives the ocean by surface cooling concentrated at the center of the basin, while Experiment II by meridional differential cooling on the sea surface. For both cases the model basin is in the northern hemisphere with a constant depth D = 4000 m and zonal and meridional widths $X = Y$ = 3000 km. The entire area is divided into 64 × 64 uniform grids. The resolution of the grid size $\triangle x = \triangle y$ = 46.9 km is sufficient for the viscous western boundary layer, but not for narrow coastal boundary layers or for the radius of deformation of higher modes at high latitudes. The total depth is divided into 40 uneven grid boxes to give fairly fine vertical resolution to make smooth the transform between the MLM and MMM variables (see Table 4.1).

We put basic parameters of the MLM as ρ_c = 1.0 g cm^{-3}, g= 9.806×10^{2}cm s^{-2}, β = 2.3×10^{-13}cm^{-1}s^{-1}, ν_H = 5.0×10^{7}cm^2 s^{-1}, ν_V = 2.0 cm^2 s^{-1}, κ_H = 5.0×10^{7}cm^2 s^{-1}, and κ_V = 2.0 cm^2 s^{-1}; rather large values of ν and κ were chosen for preferred linearity and steadiness. The experiments were carried out with a multi-level model like that of Cox (1984). Each experiment was started from rest for the initial density which is uniform horizontally, but increases linearly from ρ = 1.025 g cm^{-3} at the surface to 1.028 g cm^{-3} at the bottom. In Experiments I and II, time integration was carried out over 1037 and 2024 years, respectively, after which the circulation was judged to have achieved a (quasi-)steady state; the criterion of convergence was that the rate of temporal change of the horizontal mean density is smaller than 1 × 10^{-15} g cm^{-3} s^{-1} at any depth. The circulation fields analyzed in the later sections correspond to those at the final data mentioned above. To accelerate the convergence we applied the method of Bryan (1984) for the initial 1025 or 1964 years in Experiment I or Experiment II, respectively.

grid number	$\triangle z$
1	10 m
2	20 m
3	40 m
4	50 m
5	60 m
6–14	80 m
15	100 m
16–40	120 m

Table 4.1: The sizes of the vertical grids used in Experiments I and II.

4.2.3 *Conversion between the MLM and MMM variables*

For consistency a brief sketch is given below how field variables are decomposed into variables of vertical modes and *vice versa*; see Chapter 3 for details. For example, the zonal current u is transformed to its nth vertical mode u_n through

$$u_n(x,y,t) = \frac{1}{D}\int_{-D}^{0} u(x,y,z,t)\hat{u}_n(z)dz. \tag{4.10}$$

As is usual for vertical modes of gravity waves, the *normalized* basis function $u_n(z)$ satisfies

$$-\frac{d}{dz}\left(\frac{1}{N^2}\frac{d\hat{u}_n}{dz}\right) = \frac{1}{c_n^2}\hat{u}_n, \tag{4.11}$$

and

$$\frac{d\hat{u}_n}{dz} = 0 \qquad \text{at} \quad z = 0 \ \text{ and } -D, \tag{4.12}$$

where $N(z)$ is the buoyancy frequency. The square root of the eigenvalue denotes the inverse of the phase speed c_n of the nth-mode gravity waves. Conversely, modes are synthesized to give the physical variable as

$$u(x,y,z,t) = \sum_{n=0}^{\infty} u_n(x,y,t)\hat{u}_n(z). \tag{4.13}$$

In order to apply the above transforms between the physical domain and the modal domain, the basic stratification $\bar{\rho}(z)$ must be specified. We defined $\bar{\rho}(z)$ as the horizontal average of density at the final (quasi-)steady state realized in Experiment I. In Experiment II, however, strongly nonlinear processes such as coastal upwelling (downwelling) or deep-water formation by convection deviate the stratification near the coastal boundary much from that in the interior region. We therefore defined $\bar{\rho}(z)$ as the average over the interior area that is more than 650 km away from the western boundary, 514 km distant from the southern boundary, and 797 km offshore from the other coasts. After calculating $N^2(z)$ from $\bar{\rho}(z)$, we calculated the basis eigenfunctions numerically.

4.2.4 *MMM procedures*

To calculate the three-dimensional circulation in the MMM sense, each diffusive mode must be solved with assigned *forcing* F_n^x, F_n^y, and Dq_n, which appear on the right-hand side of the governing equations of the nth mode

$$\frac{\partial u_n}{\partial t} - fv_n = -g_n\frac{\partial \eta_n}{\partial x} - R_n u_n + \nu_H\nabla_H^2 u_n + F_n^x, \tag{4.14}$$

$$\frac{\partial v_n}{\partial t} + fu_n = -g_n\frac{\partial \eta_n}{\partial y} - R_n v_n + \nu_H\nabla_H^2 v_n + F_n^y, \tag{4.15}$$

$$\frac{\partial \eta_n}{\partial t} + D\left(\frac{\partial u_n}{\partial x} + \frac{\partial v_n}{\partial y}\right) = -\lambda_n\eta_n + \kappa_H\nabla_H^2\eta_n + Dq_n; \tag{4.16}$$

refer to Chapter 3 for details of notations, definitions, and derivations. The forcing terms are transforms of the residual terms F^x, F^y, and Q of the primitive equations:

$$F^x(x,y,z,t) = -u\frac{\partial u}{\partial x} - v\frac{\partial u}{\partial y} - w\frac{\partial u}{\partial z} + \frac{\partial}{\partial z}\left(\nu_V \frac{\partial u}{\partial z}\right) - \frac{\partial}{\partial z}\left(\tilde{\nu_V}\frac{\partial u}{\partial z}\right), \tag{4.17}$$

$$F^y(x,y,z,t) = -u\frac{\partial v}{\partial x} - v\frac{\partial v}{\partial y} - w\frac{\partial v}{\partial z} + \frac{\partial}{\partial z}\left(\nu_V \frac{\partial v}{\partial z}\right) - \frac{\partial}{\partial z}\left(\tilde{\nu_V}\frac{\partial v}{\partial z}\right), \tag{4.18}$$

$$Q(x,y,z,t) = -u\frac{\partial \rho}{\partial x} - v\frac{\partial \rho}{\partial y} - w\frac{\partial(\rho-\bar{\rho})}{\partial z} \tag{4.19}$$

$$+\frac{\partial}{\partial z}\left\{(\kappa_{ca}+\kappa_V)\frac{\partial \rho}{\partial z}\right\} - \frac{\partial^2}{\partial z^2}\left(\tilde{\kappa_V}\rho\right) + Q_{body}, \tag{4.20}$$

where $\tilde{\nu_V} = C_\nu/N^2$ and $\tilde{\kappa_V} = C_\kappa/N^2$ are the modified forms of vertical viscosity and diffusion. The two constants C_ν and C_κ are to be adjusted to the basic stratification of the MLM experiment: we put $C_\nu = C_\kappa = 1.53\times10^{-6}\mathrm{cm}^2\ \mathrm{s}^{-3}$ and $C_\nu = C_\kappa = 6.14\times10^{-7}\mathrm{cm}^2\ \mathrm{s}^{-3}$ in Experiments I and II, respectively.

It is the linearized formulation and rather artificial forms of $\tilde{\nu_V}$ and $\tilde{\kappa_V}$ that yield the residual terms: nonlinear advection of momentum, surface cooling, advective cooling, convective cooling, and the differences in the expression of vertical diffusion of momentum and density between the MLM and MMM. They are contributed to mainly by nonlinear processes such as convective adjustment or intense vertical motion adjacent to the coastal boundary. In principle those residual terms should be determined consistently with the circulation itself within the MMM. If the circulation is weak enough, it may be possible to estimate nonlinear terms of F^x, F^y, and Q in a successive way starting with an appropriate initial guess. Within the present framework of the linearized MMM, however, we deal with all the residual terms as the external data to be assigned based on the MLM experiment.

Fortunately it is possible to justify some simplification about the estimation of forcing to each mode. In particular we may disregard the residual term of momentum (F^x, F^y). It was confirmed that the thermohaline circulations for Experiments I and II were reproduced quite well by only the thermodynamical forcing Q. This is physically because the momentum forcing is insignificant for thermohaline circulation of the basin scale; it is the distribution of density that maintains thermohaline circulation. The modeling and estimation of thermal forcing are argued later in each experiment.

Once the forcing terms are specified, it is easy to calculate the responses of diffusive modes by use of the direct method shown in Chapter 3. The three-dimensional circulation is then reconstructed from the steady solutions of modes through the formulas in the previous subsection.

4.3 EXPERIMENT I—SURFACE COOLING LOCALIZED NEAR THE CENTER OF THE BASIN

The circulation driven by localized cooling is a basis on which to understand the circulation driven by continuous distributions of forcing. Therefore we first examine the response to the surface cooling localized near the center of a mid-latitude basin, the southern coast of which is 500 km north of the equator, whence there is no singularity of vanishing Coriolis parameter. The appropriate cooling of Haney type was specified by the relaxation time $1/\alpha = 20$ days and the distribution of reference density

$$\rho_{ref} = \rho_{base} + \triangle\rho_{ref} \exp\left\{-\frac{r^2}{{r_c}^2}\right\}, \tag{4.21}$$

where $\rho_{base} = 1.026$ g cm^{-3}, $\triangle\rho_{ref} = 0.003$ g cm^{-3}, r denotes the horizontal distance from the center of the basin, and $r_c = 80$ km is a characteristic radius of the cooled area.

4.3.1 *Experimental results in physical and modal domains*

First, Fig. 4.1 shows the profiles of the mean density $\bar{\rho}(z)$ together with the corresponding eigenfunctions $\hat{u}_n(z)$ for the lowest four baroclinic modes. Nearly linear stratification yields almost sinusoidal eigenfunctions. It is to be remarked that convection does not reach the bottom of the ocean so that the data analyzed below do not represent the *exactly* steady state, but a *quasi*-steady state, where deep water is still warming very slowly by weak conduction.

Figure 4.2 shows the current vector (u, v) and the deviation of pressure p' from its horizontal mean at four depths that represent the surface, intermediate, deep, and abyssal layers: (a) 5 m, (b) 860 m, (c) 1660 m, and (d) 3580 m. In contour maps here and henceforth, positive and negative values are indicated by solid and dashed lines, respectively, and regions of negative values are stippled. See legends of Fig. 4.2 for more details.

We see that the surface cooling drives thermal convection near the center of the basin to generate a circular cyclonic gyre in the surface layer. A feeble counter current is found at the southeast corner of the basin. At the depth of 860 m, the circulation is reversed to an anticyclonic one. Close to the western boundary, however, water still flows equatorward cyclonically as in the upper layer. It is the low pressure associated with this equatorward current that hinders the westward extension of the central high. In the deep layer, the anticyclonic circulation extends toward the western boundary layer, where the current now flows poleward weakly. A cyclonic poleward current begins to appear at the southeastern corner. Further below in the abyssal layer, we see further westward elongation of the central anticyclonic gyre along with the fully developed though weak western boundary current. Equivalently, the eastern cyclonic gyre expands its area both northwestward and southwestward, surrounding the central high and its westward extension. In particular, at lower latitudes, the cyclonic circulation reaches the western boundary, so that abyssal water flows eastward along the southern boundary.

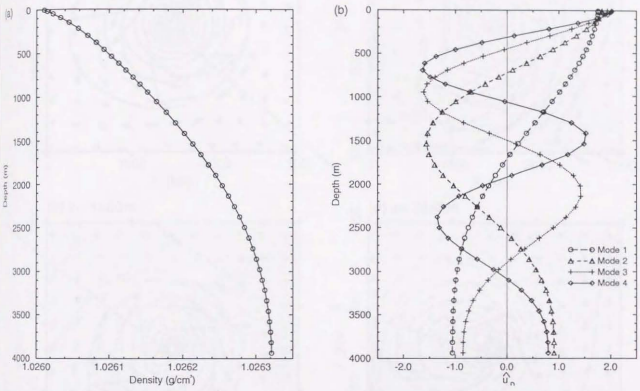

Fig. 4.1: Profiles of (a) the basic stratification $\bar{\rho}(z)$ for Experiment I and (b) the associated eigenfunctions $\hat{u}_n(z)$ for the lowest baroclinic modes $n = 1$ to 4.

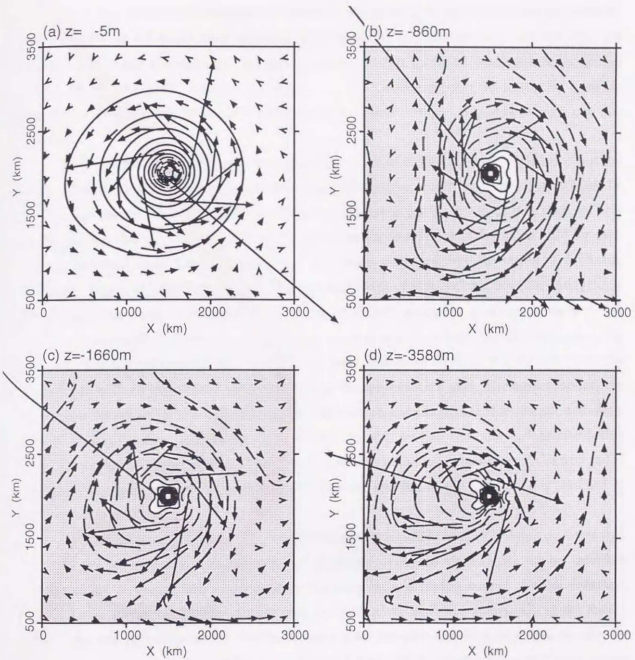

Fig. 4.2: Contours of the deviation of pressure p' from its horizontal mean and vector arrows representing the horizontal current (u, v) for Experiment I at four depths representing the surface, intermediate, deep, and abyssal layers: (a) 5 m, (b) 860 m, (c) 1660 m, and (d) 3580 m. Positive and negative contours are indicated by solid and dashed lines, respectively, while regions of negative values are stippled. Contour intervals (abbreviated to CIs) are (a) 1.62×10^{2}dyn cm^{-2}, (b) 1.40×10^{1}dyn cm^{-2}, (c) 1.01×10^{1}dyn cm^{-2}, and (d) 7.37 dyn cm^{-2}, respectively. Velocity scales (abbreviated to VSs) are (a) 1.73 cm s^{-1}, (b) 1.38×10^{-1}cm s^{-1}, (c) 9.12×10^{-2}cm s^{-1}, and (d) 8.32×10^{-2}cm s^{-1}, respectively, where the velocity scale is defined as the current speed whose vector arrow is as long as the width of the frame. Overrunning arrows are scissored off.

Even this simplest thermohaline circulation generates a complicated three-dimensional structure. Figure 4.2 raises more questions than answers. For instance one may ask why the abyssal anticyclonic circulation is elongated westward with poleward countercurrents in the eastern part of the basin, whereas the surface layer is dominated over by a circular cyclonic gyre in the almost entire basin. It is not clear what causes different response at high and low latitudes.

To investigate these problems, we expand the circulation field in terms of diffusive vertical modes. It suffices to discuss the lowest four baroclinic modes, which occupy about 80% of the total kinetic energy. The experimental results of (u, v) and p' are transformed into their vertical modes (u_n, v_n) and η_n (Fig. 4.3), where the sign is chosen to represent the surface field for each mode. The lowest mode has a cyclonic gyre that extends westward from the center of the basin, to a larger degree at lower latitudes. To the east and south of this cyclonic flow, an anticyclonic circulation is observed accompanied by a westward current along the southern boundary. We also find a notable equatorward current along the western boundary. As the mode number increases, the central cyclonic gyre becomes broader and more circular to dominate over the whole basin with an exceptional countercurrent in the southeastern part. For higher modes, the central low decays so rapidly before it reaches the western boundary that the western boundary current cannot develop. Comparing Fig. 4.3 with Fig. 4.2, we find that the surface circulation is similar to that of higher modes, while the abyssal circulation resembles that of the first mode except for the opposite sign; note that the surface current due to the first mode is reversed in the abyssal layer.

The prevalence of higher modes in the surface layer is simply because cooling concentrated near the surface generates the same sign of responses of modes there. The modes interfere constructively at the surface to accumulate the same sign of higher modes. To the contrary, odd and even modes cancel one another near the bottom to leave the dominance of the lowest mode. The interpretation can be confirmed easily, if we compare the circulation due to only the first mode and that due to the other modes; Figs. 4.4(a) and (b) display those two circulations in the surface and abyssal layers, respectively.

The above argument exemplifies how to reconstruct and understand the three-dimensional structure of thermohaline circulation through the synthesis of diffusive modes. The remaining question is how we can understand the response of each mode. Before proceeding to that problem, however, let us have a little more detailed analysis into this fundamental thermohaline circulation in the next subsection.

4.3.2 *Further analysis of the circulation*

For closer examination we prefer contours of meridional velocity v, because v is known

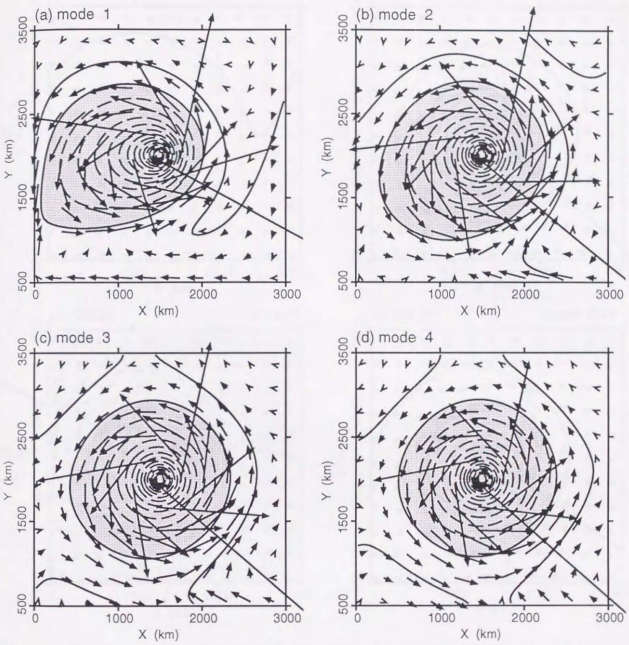

Fig. 4.3: Contours of the deviation of interfacial displacement η_n' from its horizontal average and vector arrows representing the horizontal current (u_n, v_n) for the (a) first, (b) second, (c) third, and (d) fourth modes. The sign is chosen so that the figures represent the surface field of each mode. CIs are (a) 3.16×10^2cm, (b) 1.60×10^3cm, (c) 3.46×10^3cm, and (d) 5.20×10^3cm, respectively. For any mode, VS is 9.49×10^{-2}cm s^{-1}. See Fig. 4.2 for legends.

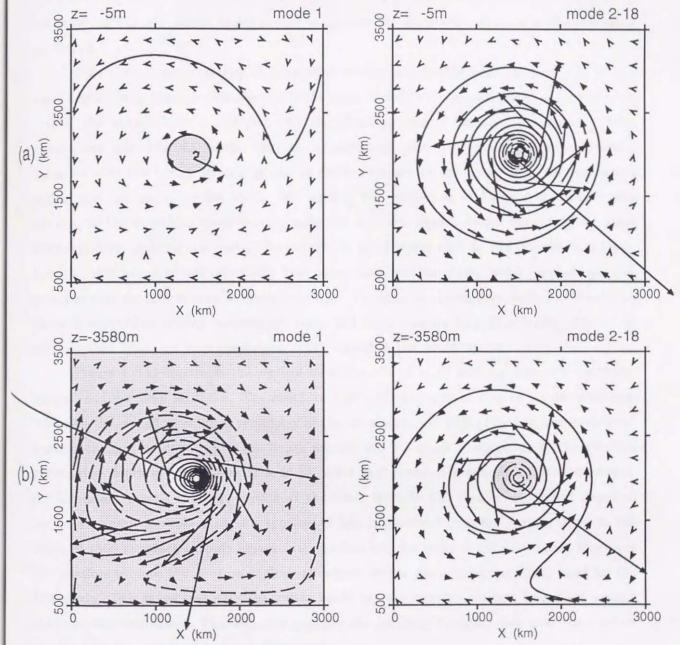

Fig. 4.4: Comparison of the circulation for Experiment I due to the lowest mode (left), and that due to the synthesis of the other higher modes $n = 2$ to 18 (right), in (a) the surface layer (5m) and (b) the abyssal layer (3580 m). Vector arrows represent the horizontal current (u, v) and contours are for the deviation of pressure p' from its horizontal average. The lowest mode dominates the abyssal layer, while the pattern of higher modes prevails in the surface layer. CIs are (a) 1.30×10^{2}dyn cm^{-2} and (b) 1.20×10^{1}dyn cm^{-2}. VSs are (a) 1.6 cm s^{-1} and (b) 1.0×10^{-1} cm s^{-1}. See Fig. 4.2 for legends.

to play a crucial role in determining the thermohaline circulation through the vorticity balance (Stommel and Arons, 1960). At the same depths as in Fig. 4.2, contours of meridional velocity are shown in Fig. 4.5, which makes it easy to confirm the description about v in the preceding subsection.

Figure 4.6 draws contours of horizontal convergence $\partial w/\partial z$ multiplied by f/β at the same depths as in Fig. 4.5. We see that wide areas of downwelling (shrinking) are distributed even in the abyssal layer in contrast with the classic picture of Stommel and Arons (1960). Comparison with Fig. 4.5 verifies that the advection of planetary vorticity is approximately balanced with the vortex stretching except either adjacent to the coast or in the convective region near the center of the basin. We confirm the prediction in Chapter 2 that vertical velocity, or the stretching more exactly, takes the opposite signs between the inner and outer boundary layer close to the western boundary. In some layers such as the intermediate layer, however, that rule does not necessarily hold along some portion of the western boundary. This is ascribed to the interference of multiple modes. Though not shown here, each mode exhibits opposite signs of stretching between the inner and outer western boundary layers. This is an example that dynamics becomes simpler when viewed in the modal space.

Figure 4.7(a) illustrates the vertical structure of v at zonal sections along the southern, central, and northern latitudes. The southern and northern sections display similar contours, reflecting the overall meridional symmetry of the circulation. At either latitude, the meridional velocity changes its direction at the depth around 500 m, which corresponds to the effective penetration depth of convection. It is to be noted that contours gradually descend westward. An inspection reveals that the section at the lower latitude has smaller downward slopes of contours. Near the western coast a southward flow is observed from the surface down to the depth of 1500 m, which roughly agrees with the depth of the node of the first mode. Moreover it is possible to show this southward flow is confined within the western boundary layer for the first mode. This is because only the lowest mode has a noticeable western boundary current in the present conditions. This behavior explains the southward counter flow near the western boundary in the intermediate layer (Fig. 4.2b).

Figure 4.8 shows v at meridional sections along the western, midwestern, mideastern, and eastern longitudes. Evidently contours are almost symmetric with respect to the forced latitude. In the midwestern region, surface layers have equatorward currents associated with the cyclonic gyre, while intermediate to deep layers have poleward flows. The equatorward current in the deeper layer is the continuation of the mideastern equatorward flow at intermediate levels. Likewise the poleward current in the abyssal layer is connected with the eastern deep or abyssal layer. From the midwestern section toward the western section, contours descend and go away from the cooled latitude. In short, contours expands westward, in particular at higher

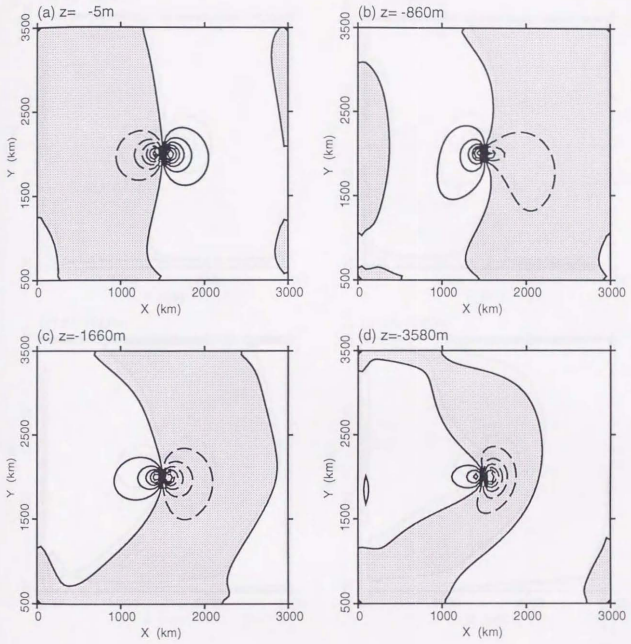

Fig. 4.5: Contours of the meridional velocity v for Experiment I at the same depths as in Fig. 4.2. CIs are (a) 2.38×10^{-1} cm s^{-1}, (b) 1.92×10^{-2} cm s^{-1}, (c) 1.16×10^{-2} cm s^{-1}, and (d) 1.10×10^{-2} cm s^{-1}, respectively. See Fig. 4.2 for legends.

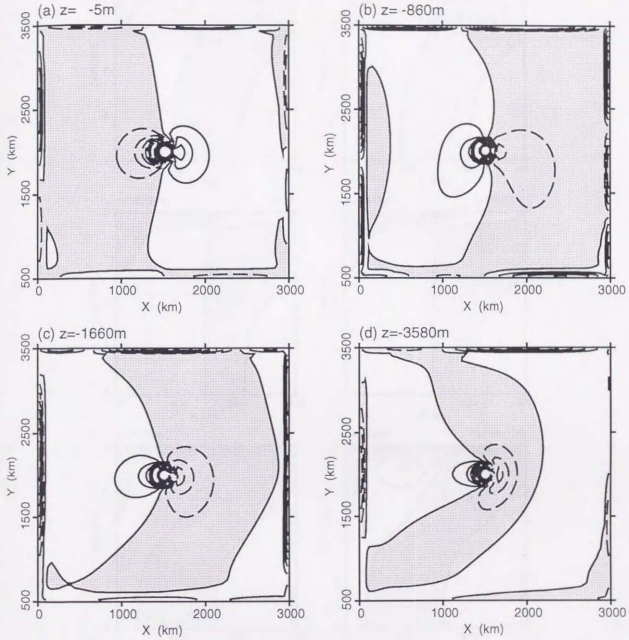

Fig. 4.6: Contours of horizontal convergence multiplied by f/β at the same depths as in Fig. 4.5. Comparison with Fig. 4.5 verifies that the stretching of a vortex column balances the advection of the planetary vorticity as a whole except near the boundary layers and in the directly cooled region. At each depth, CI is the same as in Fig. 4.5. See Fig. 4.2 for legends.

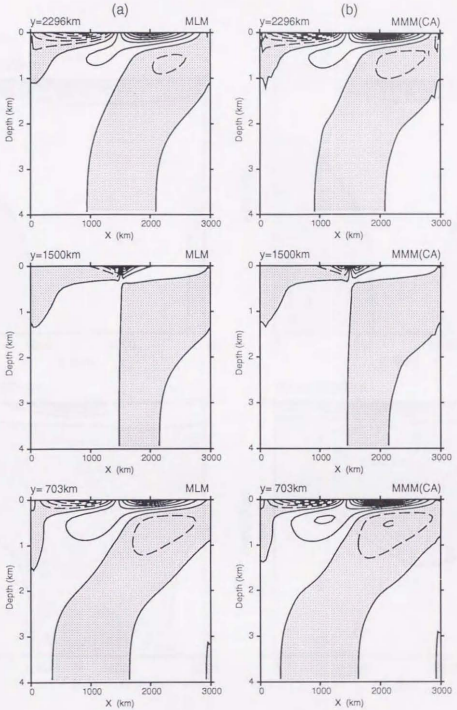

Fig. 4.7: Contours of v for Experiment I at three zonal sections representing the southern, central and northern latitudes from bottom to top; 703 km, 1500 km, and 2296 km north of the southern boundary: (a) the MLM experiment and (b) the MMM synthesis to the *modeled* Q_{ca}. The MLM experiment is reproduced quite well by the MMM synthesis which is calculated to the modeled convective cooling Q_{ca}. CIs are 1.13×10^{-2}cm s^{-1}, 2.38×10^{-1}cm s^{-1}, and 5.62×10^{-3}cm s^{-1}, respectively.

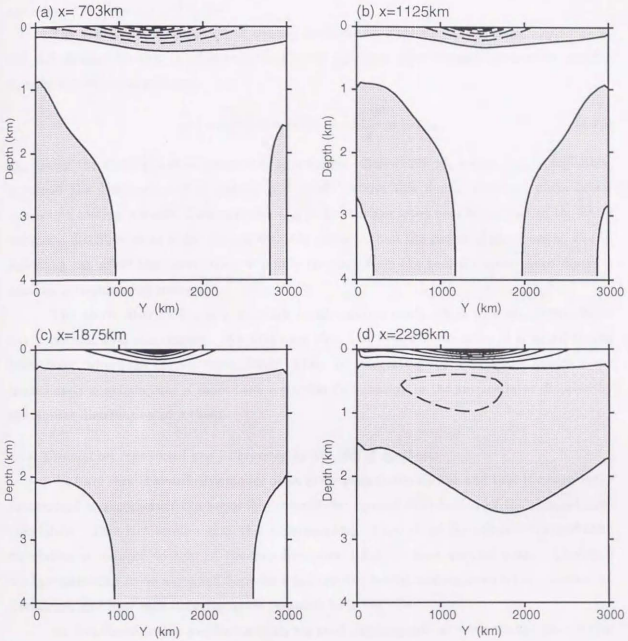

Fig. 4.8: Contours of v for Experiment I at four meridional sections representing the western, mid-western, mid-eastern, and eastern longitudes: (a) 703 km, (b) 1125 km, (c) 1875 km, and (d) 2296 km east of the western boundary. CIs are (a) 1.90×10^{-2}cm s^{-1}, (b) 5.78×10^{-2}cm s^{-1}, (c) 6.07×10^{-2}cm s^{-1}, and (d) 1.65×10^{-2}cm s^{-1}, respectively. See Fig. 4.2 for legends.

latitudes. Along the mideastern section, the surface and intermediate layers have poleward and equatorward flows, respectively, just opposite to those in the midwestern basin. The poleward flow in the lowest layers means the prevalence of the first mode at depths, in accordance with the scheme of Stommel and Arons.

The horizontal distribution of density is shown in Fig. 4.9 at the same depths as in Fig. 4.2. It must be born in mind that the Poisson equation approximately governs the density distribution of the experiment:

$$\frac{\partial}{\partial z}\left(\kappa_V \frac{\partial \rho}{\partial z}\right) + \kappa_H \nabla_H^2 \rho = -\frac{\rho_c N^2}{g} w - Q_{ca}, \tag{4.22}$$

Q_{ca} being the cooling due to convective adjustment. Below 500 m, where Q_{ca} is negligible, ρ follows the distribution of w though it is weak. Above this depth, however, much larger convective cooling prevails. Concentrated Q_{ca} in the surface layer near the center of the basin induces a distribution of ρ that decays with the distance from the center of Q_{ca}; cooling due to upwelling can affect the distribution of ρ only far away from the cooled region. Accordingly ρ assumes a circular distribution.

The above distribution of ρ provides an alternative explanation why the surface layer has a circular cyclonic current. We first note that the pressure variation p' is small in the lower layer, where the current flows slowly. Then, by integrating the hydrostatic equation, we immediately conclude that p' must have a circular distribution in the surface layer dictated by the similar distribution of ρ there.

4.3.4 *Circulation reproduced and interpreted by the MMM synthesis*

We have seen that diffusive modes often allow plainer description and that they are easily synthesized to reconstruct the seemingly complicated spatial distribution of the thermohaline circulation. This fact implies that the understanding of the three-dimensional thermohaline circulation is reduced to that of the two-dimensional field of each vertical mode. Therefore the last questions to be answered here are what distribution of cooling substantially drives the circulation and how each diffusive mode responds to it.

As mentioned in the previous section we need not take into account for the momentum forcing. Among various terms of the remaining thermodynamical forcing, the difference in the expression of vertical diffusions contributes little, because it is nearly uniform horizontally so that it changes the mean density field but barely affects the current field. The surface cooling almost follows the specified reference density, whence it is to be evaluated fairly well. Though relatively insignificant at other locations, the very surface cooling near the center of the basin drives the circulation. However, the effects of this forcing in that area can be represented rather by the convective cooling as its agent. The advective cooling is difficult to estimate because

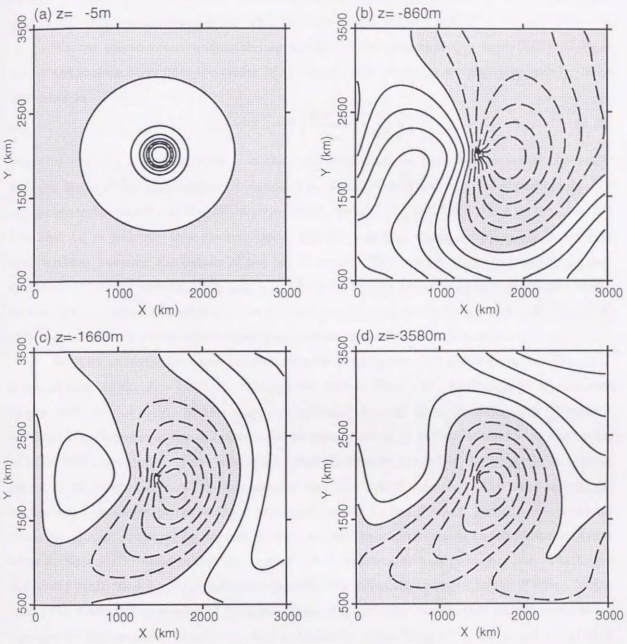

Fig. 4.9: Contours of the deviation of density ρ' from the horizontal mean for Experiment I at the same depths as in Fig. 4.2. CIs are (a) 1.37×10^{-5}g cm^{-3}, (b) 1.14×10^{-7}g cm^{-3}, (c) 6.45×10^{-8}g cm^{-3}, and (d) 1.85×10^{-9}g cm^{-3}, respectively. See Fig. 4.2 for legends.

we have to know both current and density. Fortunately this term was confirmed small for the slow circulation of Experiment I. After all, convective cooling Q_{ca} turned out to be the most essential; it is larger than the other terms of thermodynamical forcing by the order of three or more. In fact, the MMM synthesis to the forcing of Q_{ca} estimated from the MLM results yielded a circulation almost identical with that due to the MLM itself.

We can advance our understanding further, if we note that Q_{ca} is virtually confined within the surface layer near the center of the basin. For simplicity we may idealize Q_{ca} to be expressed as

$$Q_{ca} = A_{ca} \cdot H \left(\frac{z + z_{ca}}{z_{ca}} - \frac{r^2}{r_{ca}^2} \right), \tag{4.23}$$

where H denotes a step function, r is the horizontal distance from the center of the basin, and the zeros of the argument of H defines the region of convection to be a paraboloid. To approximate the results of the MLM experiment, we put A_{ca} =1.3×10^{-11}cm s^{-1}, r_{ca} = 164 km, and z_{ca} = 540 m. In a crudest sense, this form of Q_{ca} would be plausible to imagine even without knowing the details of the MLM results. This model of convective cooling was transformed into its vertical mode $Q_{ca,n}$, to which the steady response of each mode was solved by the direct method (Chapter 3). We see that the vertical mode thus calculated (Fig. 4.10) agrees quite well with that decomposed from the experimental field (Fig. 4.3).

Next let us investigate how the concentrated cooling modeled above generates the circulation of each mode (Fig. 4.10). To this end we further idealize the forcing to be a point *sink* at the center of the basin. At this stage it is relevant to recall three conclusions of Chapter 2, in which the response of the diffusive reduced-gravity mode to the point *source* at the center of basin was investigated. First, negligibly small dissipation simplifies the response to a point source as the combination of (1) the central strong high driven directly by the point source, (2) its westward extension to the western boundary current by the β effect, and (3) an overall cyclonic circulation surrounding the central high; the last item corresponds to the Stommel-Arons scheme. Second, diffusion makes the central circulation weaker and more circular. Third, the diffusivity multiplied by f^2/c_n^2 measures the effective diffusivity relative to the β effect, which causes the westward elongation of the gyre. Then, it is sufficient to note that diffusive effects are stronger for higher modes (smaller c_n) and at higher latitudes (larger f^2). Thus each circulation in Fig. 4.10 turned out to be interpreted as the response to the localized sink at the center of the basin.

Finally the responses of the modes n = 1 to 18 to the *modeled* Q_{ca} mentioned above were synthesized to yield (u, v) and p' in Fig. 4.11, which are nearly identical with the MLM experimental results shown in Fig. 4.2. Also contours of v thus calculated at three zonal sections shown in Fig. 4.7(b) are compared quite favorably with those in Fig. 4.7(a) obtained from the

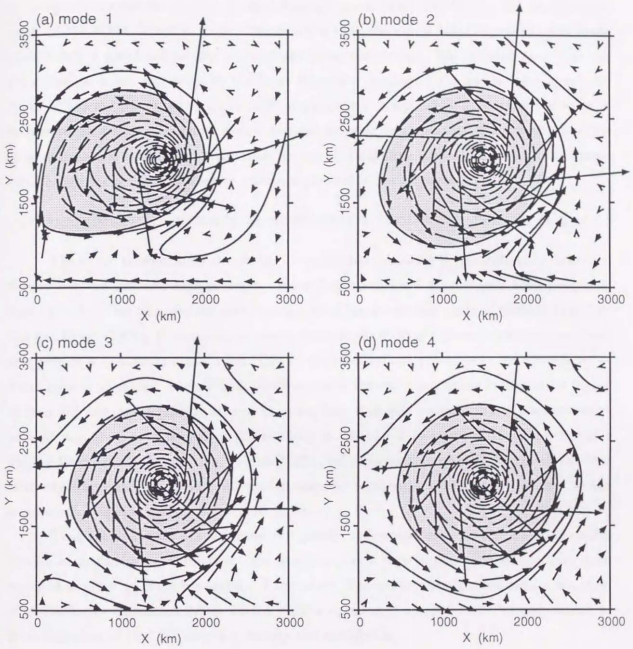

Fig. 4.10: The same as Fig. 4.3 except that each mode is calculated as the response to the modeled convective cooling concentrated near the center of the basin in the upper 500 m or so. CIs are (a) 3.01×10^{2}cm, (b) 1.54×10^{3}cm, (c) 3.34×10^{3}cm, and (d) 5.01×10^{3}cm, respectively. For any mode, VS is 9.49×10^{-2}cm s^{-1}.

MLM.

It is not surprising that the MMM synthesis reproduces the steady circulation achieved by the MLM experiment, if every detailed forcing is given to the MMM from the experimental result of the MLM. What is to be emphasized is that the above MMM synthesis was made against only a simplified forcing *modeled* on convective cooling. We thus conclude that the circulation is driven primarily by the local convective cooling in the upper layer above the depth of 500 m. Also the overall circulation has proved independent of detailed processes of deep-water formation. Therefore it now becomes possible to understand dynamically how the three-dimensional structure is maintained for the thermohaline circulation of this experiment, even though the realized field seems quite complicated in the physical domain.

4.4 EXPERIMENT II—MERIDIONAL DIFFERENTIAL COOLING ON THE SEA SURFACE

The ocean thermohaline circulation is maintained primarily by the difference in surface density between low and high latitudes. Accordingly numerical experiments have frequently been carried out for this fundamental situation since the pioneering works of Holland (1971) or Gill and Bryan (1971). Previous experiments, however, have often reported strange phenomena that require a dynamical explanation. One of the most serious problems is the appearance of broad regions of abyssal downwelling, which seems in contradiction to the fundamental theory of Stommel and Arons (1960). It is to be noted that it is only recently that a comprehensive account was given to this curious downwelling in Chapter 2 in terms of the dynamics of a single diffusive mode. In addition, Veronis (1975), referring to Holland (1971), pointed out that relatively warm and light water downwells near the northeastern boundary, contrary to the intuition that sinking surface water must be heavy.

Thus the dynamics has still remained poorly understood even for this simplest configuration of thermohaline circulation; that is also a reason why similar experiments have been repeated so often by many researchers. Experiment II therefore examines the typical situation of thermohaline circulation driven by the surface warming at tropical latitudes and cooling at polar latitudes, so that the reference density was specified as

$$\rho_{ref} = \rho_{base} - \triangle\rho_{ref} \cos\left(\frac{\pi y}{Y}\right), \tag{4.24}$$

where $\rho_{base} = 1.025$ g cm^{-3} and $\triangle\rho_{ref} = 0.004$ g cm^{-3}; the reference density ρ_{ref} is zonally uniform but increases gradually from the equator towards polar latitudes. The relaxation time $1/\alpha$ for the surface cooling was set at 100 days. In this case the southern coast of the model basin is located at the equator, where symmetric boundary conditions were applied. The circulation in fact corresponds to that in a meridionally symmetric basin which lies in both hemispheres.

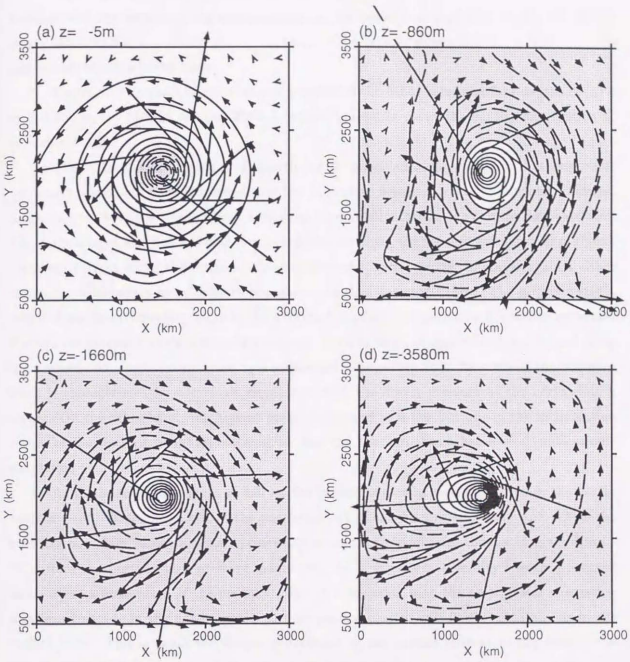

Fig. 4.11: The same as Fig. 4.2 except that the circulation is the synthesis of the responses of the modes $n = 1$ to 18 to the modeled convective cooling concentrated near the center of the basin in the upper 500 m or so. CIs are (a) 1.40×10^{2}dyn cm^{-2}, (b) 1.29×10^{1}dyn cm^{-2}, (c) 8.31 dyn cm^{-2}, and (d) 5.67 dyn cm^{-2}, respectively. VSs are (a) 1.26 cm s^{-1}, (b) 1.14×10^{-1} cm s^{-1}, (c) 7.10×10^{-2} cm s^{-1}, and (d) 6.94×10^{-2} cm s^{-1}, respectively.

4.4.1 *Experimental results in physical and modal domains*

Figure 4.12 shows the profile of the basic stratification obtained from the MLM results together with the corresponding eigenfunctions for the lowest four baroclinic modes. Relatively strong stratification is confined within the upper 500m or so, below which lies a fairly uniform and weakly stratified deep layer.

Figure 4.13 displays the current and pressure of the MLM results at four depths of (a) 5 m, (b) 460 m, (c) 1420 m, and (d) 3580 m, while Figure 4.14 shows the density distribution at the same depths.

The surface layer is controlled directly by the specified density ρ_{ref}, so that isopycnals are nearly zonal and crowded around central latitudes, where ρ_{ref} has the largest gradient. According to this density distribution thermal-wind relation steers the surface flow eastward. The surface layer also has a strong northward current along the western boundary and a weak westward current along the equator. Flowing eastward, surface water impinges against either the northern boundary or the eastern boundary, and then downwells there. The surface water is supplied partly by upwelling close to the western boundary and partly by horizontal advection through the poleward western boundary current. A warm water tongue extends northward along the western boundary, accompanied by a southward weak return flow. As a whole, the northern basin is characterized by a cyclonic circulation with the lowest pressure at the northwestern corner. On the other hand, the highest pressure is found at a low latitude in the recirculation region of the western boundary current, so that the southern basin has a weak anticyclonic circulation.

At the intermediate depth of 460 m, the current is mostly reversed except in the northwestern part. Water flows out of the northern part of the eastern boundary and enters the northern boundary, circulating anticyclonically around a pressure ridge that extends southwestward from the northeastern pressure maximum. As is expected, a density trough is located close to but a little south of the pressure ridge, in association with the anticyclonic circulation mentioned above. In the northwestern part we see the current still flow cyclonically as in the surface layer. This is again the deeper penetration of the surface current to the west of the cooled region as in Experiment I. It is worth while to note that the circulation in the intermediate layer is obtained approximately, if we translate the surface circulation poleward with a larger extent in the eastern part.

The deep layer at 1420 m has the maximum pressure at the northeastern corner, around which flows an anticyclonic circulation. This circulation is bounded to the south by a cyclonic circulation around a zonal pressure trough at low latitude. Farther south, a weak anticyclonic circulation appears along the equator. The lightest water in the deep layer is found at the northeastern corner, farther north than that at the intermediate depth. The heaviest water on

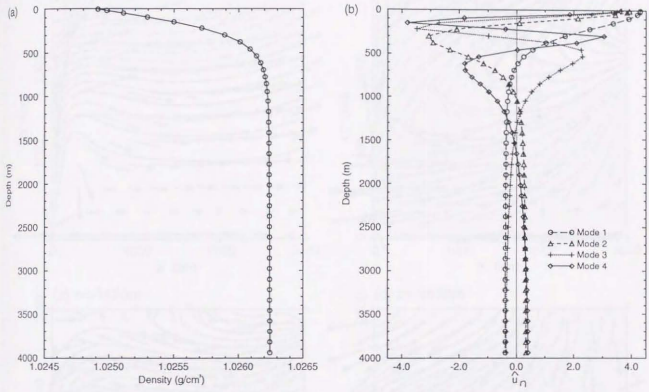

Fig. 4.12: Profiles of (a) the basic stratification $\bar{\rho}(z)$ for Experiment II and (b) the associated eigenfunctions $\hat{u}_n(z)$ for the lowest baroclinic modes $n = 1$ to 4.

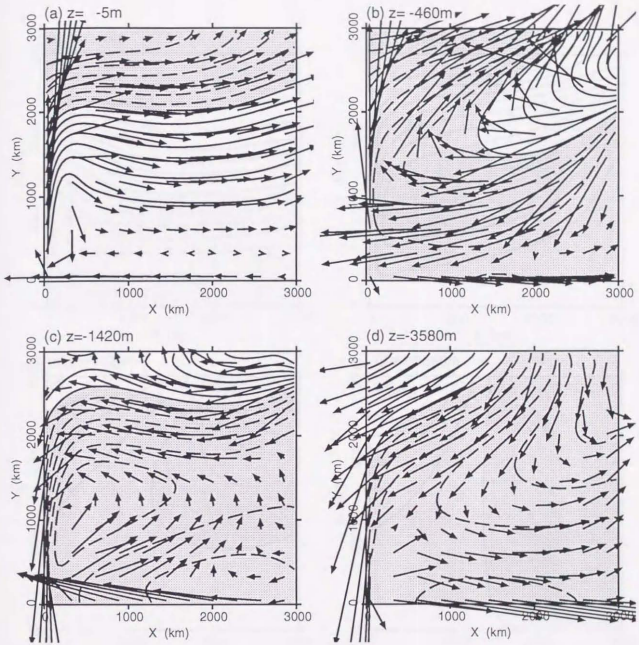

Fig. 4.13: Contours of p' and the current vector (u, v) for Experiment II at the depths of (a) 5 m, (b) 460 m, (c) 1420 m, and (d) 3580 m. CIs are (a) 2.81×10^3dyn cm^{-2}, (b) 5.68×10^2dyn cm^{-2}, (c) 1.78×10^2dyn cm^{-2}, and (d) 3.77×10^2dyn cm^{-2}, respectively. VIs are (a) 2.88×10^1 cm s^{-1}, (b) 1.92 cm s^{-1}, (c) 1.69 cm s^{-1}, and (d) 1.89 cm s^{-1}, respectively. See Fig. 4.2 for legends.

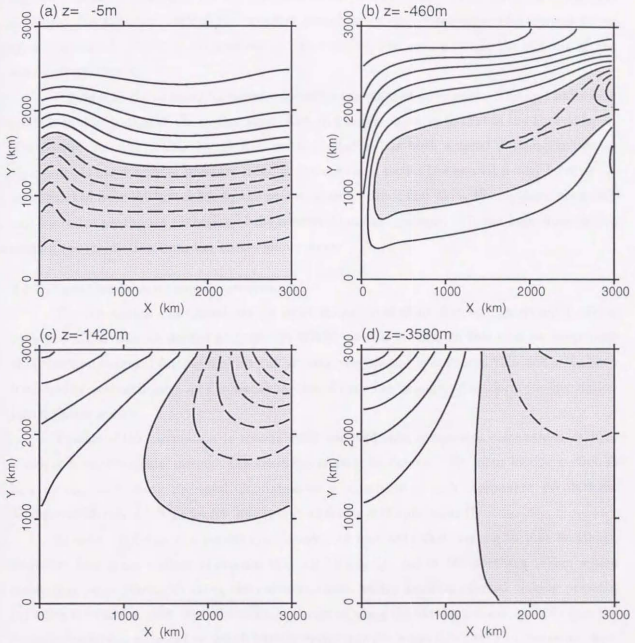

Fig. 4.14: Contours of ρ' for Experiment II at the same depths as in Fig. 4.13. CIs are (a) 1.92×10^{-4}g cm^{-3}, (b) 2.37×10^{-5}g cm^{-3}, (c) 4.75×10^{-6}g cm^{-3}, and (d) 1.48×10^{-6}g cm^{-3}, respectively. See Fig. 4.2 for legends.

the other hand is formed at the northwestern corner, where convection reaches the bottom.

The abyssal layer assumes a pattern just opposite to that in the intermediate layer. That is, a pressure trough originates near the northeastern corner and extends southwestward. The highest pressure is located at the northwestern corner, around which an anticyclonic circulation develops. To the southeast of the pressure trough a cyclonic circulation of Stommel-Arons type is observed. Water is the heaviest at the northwestern corner, while the lightest at the northeastern corner.

Figure 4.15 shows lower baroclinic modes for the realized circulation. The first baroclinic mode is similar to that of the surface layer, and, in a sense, opposite to that of the abyssal layer. The second mode is similar to the first mode in that it has both a zonal pressure trough at high latitudes and a zonal pressure ridge in the southern part. The second mode, however, is distinguished from the first mode by the westward anticyclonic flow along the northern boundary and a notable northward extension of the western boundary current. It is not easy, however, to explain the circulation from the modes shown here.

4.4.2 *Resolution into component circulations*

The circulation has turned out far more complicated than that in Experiment I, either from the MLM view at depths or from the MMM view in modes. In this case we must note that thermodynamical forcing has various physical origins and is scattered thin and wide both horizontally and vertically. As a consequence it is of little use to merely transform the circulation into diffusive modes.

Therefore the circulation is conveniently resolved into *component circulations* each of which is easy to explain through the synthesis of vertical modes. The focus in this section is how we can understand the total circulation as a composite of such component circulations. Modal consideration is still useful, but rather auxiliary in Experiment II.

In order to define component circulations, we first note that, among various locations, there are four main regions of intense thermal forcing Q: (a) in the northern region where convection takes place, (b) along the northern coast, where boundary-forced sinking prevails, (c) along the eastern coast with the similar process as along the northern coast, and (d) near the western boundary, adjacent to which surface water upwells while downwells in the outer layer in association with the poleward western boundary current. (see Fig. 4.16 for the definitions of the regions). Although cooled rather weakly per unit volume, the first region is wide in area, so that its total effective cooling is larger than that of the other principal regions, which have severe cooling (heating) in a small volume along the boundary down to deep levels. Thermal forcing outside the above regions such as the surface heating of the southern basin contributes rather little to the maintenance of the circulation of the basin scale.

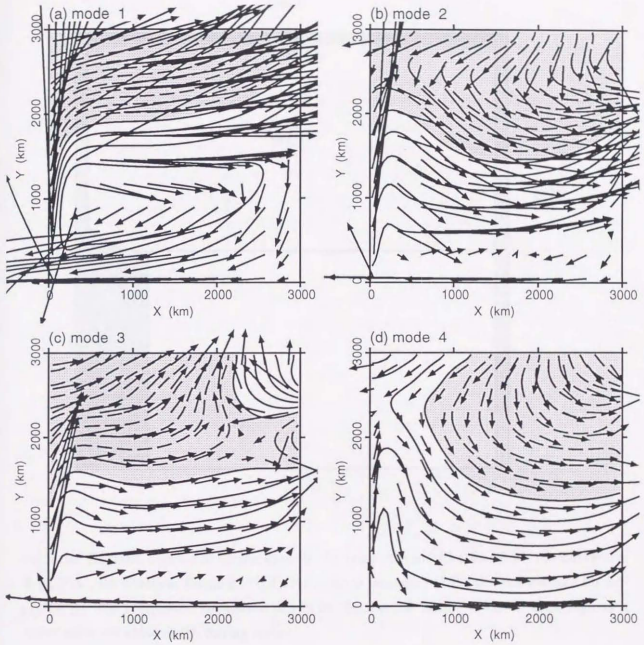

Fig. 4.15: Contours of η_n' and the current vector (u_n, v_n) for Experiment II. CIs are 9.11×10^3cm, 2.07×10^4cm, 2.36×10^4cm, and 3.76×10^4cm for the first, second, third, and fourth modes, respectively. VSs are 9.48×10^{-1} cm s^{-1} irrespective of the mode. See Fig. 4.2 for legends.

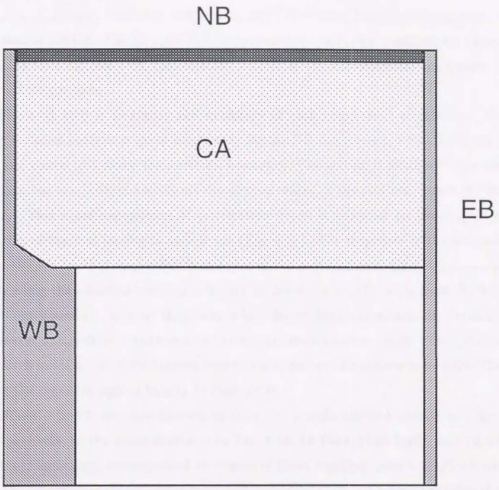

Fig. 4.16: Regional division of thermodynamical forcing into contributions from the Convective Area (CA), the Northern Boundary (NB), the Eastern Boundary (EB), and the Western Boundary (WB). The component circulation driven by the thermal forcing in one of these regions is called after the name of the forcing region.

According to this *regional* division of Q, let us define the component circulations as those driven by the total thermal forcing that is present in the respective region. Also we call them by the name of the region of forcing: (a) convective-area component, (b) northern-boundary component, (c) eastern-boundary component, and (d) western-boundary component, which are abbreviated to the CA, NB, EB, and WB components, respectively. Summed up, those principal components thus defined were confirmed to reproduce the experimental circulation quite well, though not shown here.

The next step is to clarify the dynamics of each component circulation. For brevity, however, detailed analysis is given below only for the NB component, which is driven mainly by sinking and convection along the northern boundary. Convection is shallow in the eastern part while it reaches the bottom and forms the abyssal water at the western corner of the northern boundary. This zonal dependence of penetration depth is reflected on the non-uniform zonal distribution of thermal forcing to each mode (Fig. 4.17). The responses of the modes are shown in Fig. 4.18. We see that each mode is the sum of the patterns due to point sources distributed unevenly along the northern boundary. Higher modes decay rapidly away from the forcing along the northern boundary, so that they have a broader cyclonic circulation in the northern area and a weaker anticyclonic circulation in the southeastern passive region. The peculiar pattern of the fourth mode at the northeastern corner is ascribed to the shallow convection there, which produces the opposite sign of forcing to that mode.

Modes 1 to 25 were synthesized to show the circulation and density in Figs. 4.19 and 4.20, respectively, at the same depths as in Fig. 4.13. In the surface layer, we find a low along the northern boundary accompanied by eastward flows together with a southern anticyclonic cell. At the intermediate level, water flows anticyclonically around a pressure ridge that extends southwestward from the northern part of the eastern boundary in the intermediate layer. The deep layer has a cyclonic circulation near the southern part of the western boundary layer, while a high is located along the northern boundary. The abyssal layer is just opposite to the intermediate layer; a cyclonic circulation surrounds a pressure trough that extends southwestward from the northern part of the eastern boundary. Along with the distribution of density at four depths, all these features have striking resemblance to the experimental results themselves (Figs. 4.13 and 14).

The NB component presents a typical circulation due to a zonally oriented non-uniform line source equivalent to an ensemble of point-sources aligned along the northern boundary. By virtue of the simple localization of forcing term, it is now easy to explain how modes respond to the line source, how the response differs among different modes, and what the circulation becomes like when modes are synthesized. We omit further analysis, which proceeds just as in Experiment I.

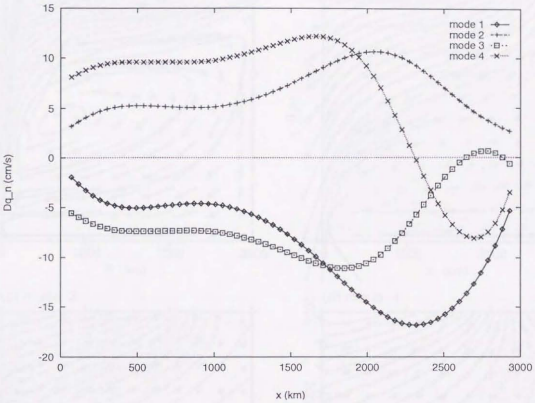

Fig. 4.17: The distributions of the thermal forcing Dq_n (n = 1 to 4) for the NB component against the eastward coordinate x along the northern boundary.

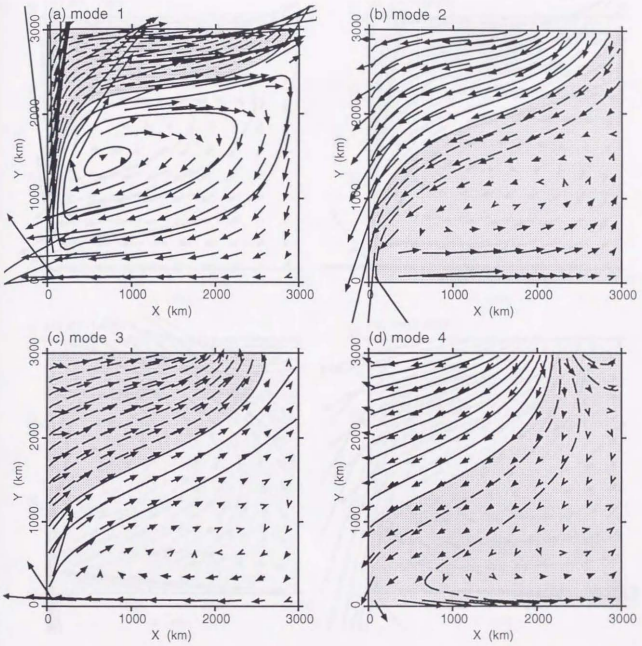

Fig. 4.18: The same as Fig. 4.15 except for the NB component. CIs are (a) 3.29×10^3cm, (b) 6.62×10^3cm, (c) 1.01×10^4cm, and (d) 1.29×10^4cm, respectively. For any mode, VS is 9.49×10^{-1}cm s^{-1}.

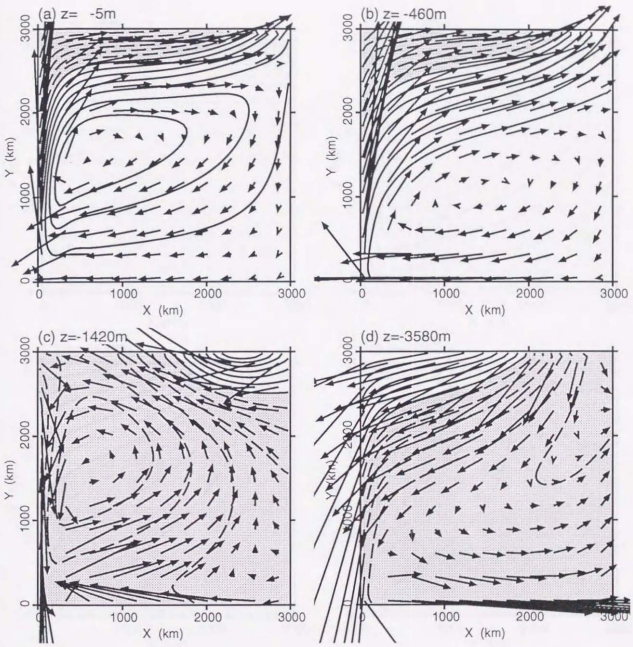

Fig. 4.19: The same as Fig. 4.13 except for the NB component calculated as the synthesis of the modes $n = 1$ to 25. CIs are (a) 5.57×10^{2}dyn cm^{-2}, (b) 2.61×10^{2}dyn cm^{-2}, (c) 9.37×10^{1}dyn cm^{-2}, and (d) 1.48×10^{2}dyn cm^{-2}, respectively. VSs are (a) 6.92 cm s^{-1}, (b) 2.27 cm s^{-1}, (c) 6.76×10^{-1} cm s^{-1}, and (d) 8.56×10^{-1} cm s^{-1}, respectively.

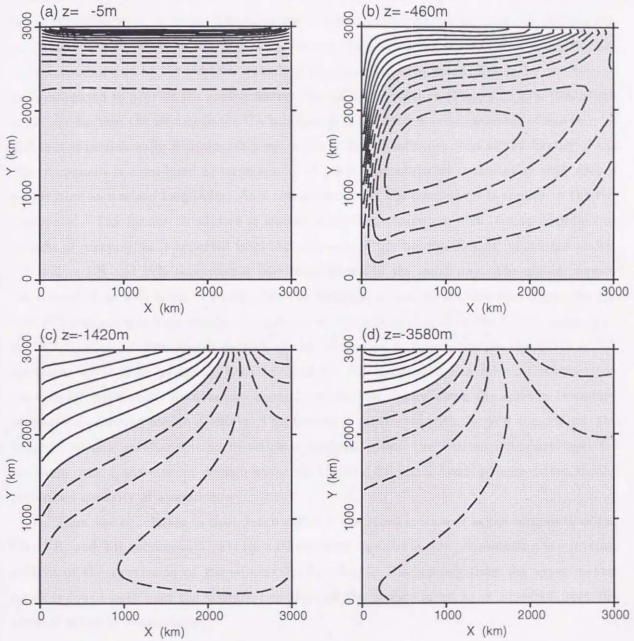

Fig. 4.20: The same as Fig. 4.14 except for the NB component calculated as the synthesis of the modes $n = 1$ to 25. CIs are (a) 1.46×10^{-5}g cm^{-3}, (b) 6.85×10^{-6}g cm^{-3}, (c) 1.55×10^{-6}g cm^{-3}, and (d) 4.99×10^{-7}g cm^{-3}, respectively.

Some characteristics of the NB component are taken over by the CA component, which is driven predominantly by convective cooling distributed widely in the northern basin. Controlled by the zonally uniform reference density, the penetration depth of convection increases from zero at the center latitude toward the northern boundary because the atmospheric cooling is enhanced with latitude. Therefore the distributions of the forcing to modes of the CA component become like those in Fig. 4.21, though the CA forcing somewhat includes the advective cooling due to the western boundary current. Diffusive modes driven by the forcing are synthesized to provide the spatial distribution of the circulation (Figs. 4.22-23). It is worth while to note that the forcing to the CA component is considered as an ensemble of line sources distributed meridionally with deeper penetration at higher latitudes, just as the forcing of the NB component is considered as an ensemble of point sources distributed zonally with deeper penetration at western longitudes. As a consequence, the CA component is similar to the NB component. The former circulation is shifted southward somewhat with laminated ridges or troughs of pressure, as is expected from the difference of the thermal forcing mentioned above.

The EB and WB components were investigated in the same way. The similar figures are presented as well (Figs. 4.24-29), but the analysis is omitted for brevity. Since the EB and WB components have smaller magnitudes of thermal forcing than the CA component or the NB component, the overall pattern of the circulation is determined by the CA and NB components. It is to be noted, however, that the EB component has substantial effects on the interior circulation, because the anomaly of the circulation along the eastern boundary propagates westward due to β effects. This feature is contrasted with the WB component, the influence of any peculiar forcing to which is confined within the western boundary layer for the same reason; the interior domain obeys the classical Stommel-Arons scheme driven by the prescribed quantity of upwelling.

Thus, the circulation in the interior region is described quite well as the composite of the CA, NB, and EB components. Figure 4.30 confirms this conjecture, reproducing the interior pattern of the circulation of Experiment II (Fig. 4.13). Discrepancy from the experimental result is found only near the western boundary of the surface layer, as is expected from the absence of the WB component.

In conclusion the circulation in Experiment II is interpreted as the composite of the component circulations CA, NB, EB, and WB. In turn, each component circulation is well understood through the synthesis of diffusive modes. The circulation is driven by an ensemble of thermal forcing distributed along and near the northern boundary with deeper forcing in the northwestern part. It will be intriguing to consider what would occur when we concentrate the distributed cooling around the northwestern corner. Then it is not difficult to envisage

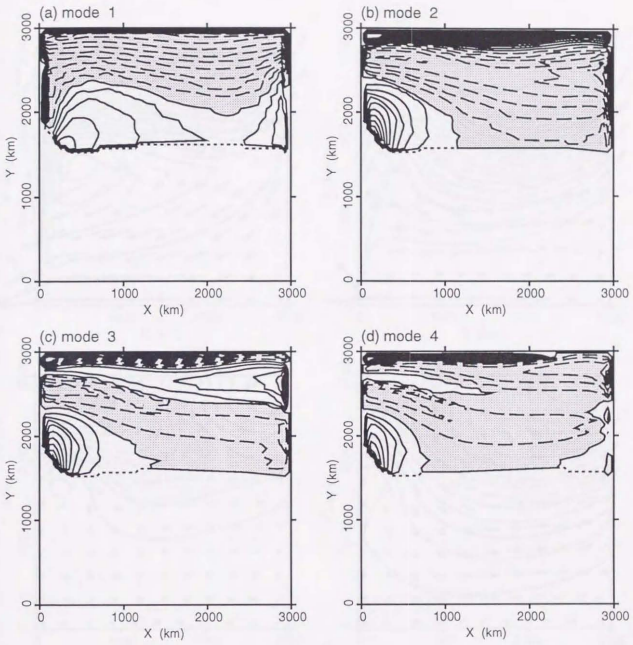

Fig. 4.21: The horizontal distributions of the thermal forcing Dq_n (n = 1 to 4) for the CA component. CIs are (a) 1.51×10^{-4}cm s^{-1}, (b) 3.00×10^{-4}cm s^{-1}, (c) 5.23×10^{-4}cm s^{-1}, and (d) 7.83×10^{-4}cm s^{-1}, respectively. The dotted line borders the area in concern, which is defined in Fig. 4.16. See Fig. 4.2 for legends.

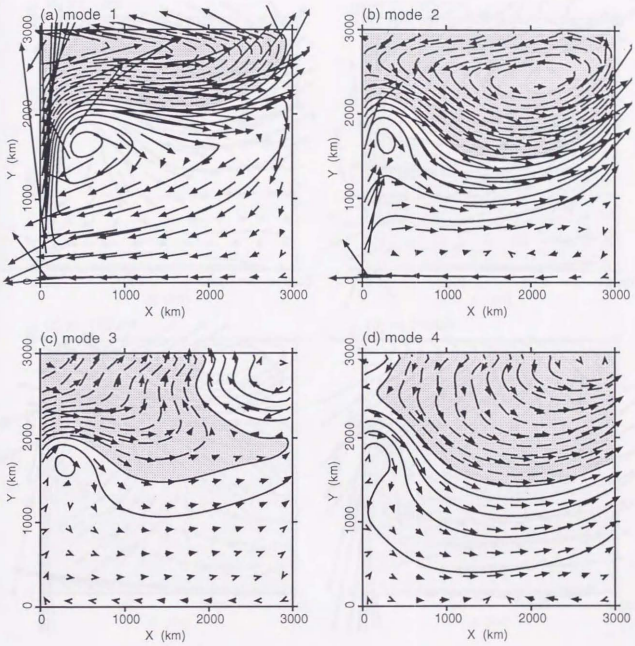

Fig. 4.22: The same as Fig. 4.18 except for the CA component. CIs are (a) 2.45×10^3cm, (b) 5.90×10^3cm, (c) 9.69×10^3cm, and (d) 1.43×10^4cm, respectively. For any mode, VS is 9.49×10^{-1}cm s^{-1}.

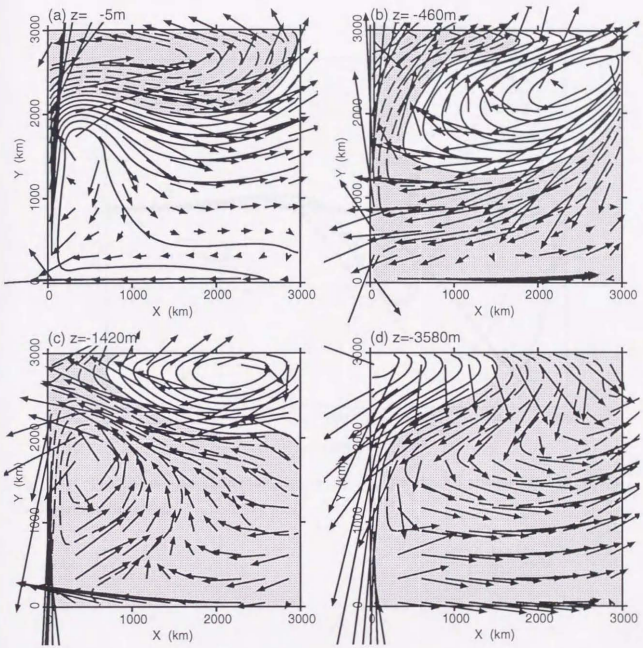

Fig. 4.23: The same as Fig. 4.19 except for the CA component. CIs are (a) 9.56×10^{2}dyn cm^{-2}, (b) 1.50×10^{2}dyn cm^{-2}, (c) 7.17×10^{1}dyn cm^{-2}, and (d) 1.07×10^{2}dyn cm^{-2}, respectively. VSs are (a) 6.68 cm s^{-1}, (b) 8.60×10^{-1} cm s^{-1}, (c) 4.60×10^{-1} cm s^{-1}, and (d) 5.12×10^{-1} cm s^{-1}, respectively.

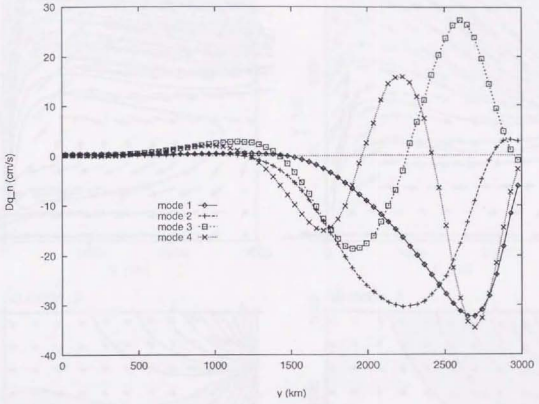

Fig. 4.24: The distribution of the thermal forcing Dq_n for the EB component against the northward coordinate y.

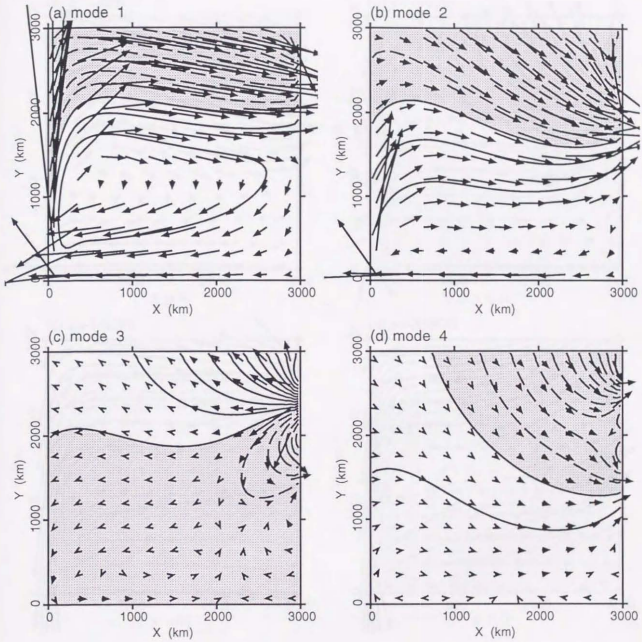

Fig. 4.25: The same as Fig. 4.18 except for the EB component. CIs are (a) 3.73×10^{3}cm, (b) 1.37×10^{4}cm, (c) 8.87×10^{3}cm, and (d) 1.61×10^{4}cm, respectively. For any mode, VS is 9.49×10^{-1}cm s^{-1}.

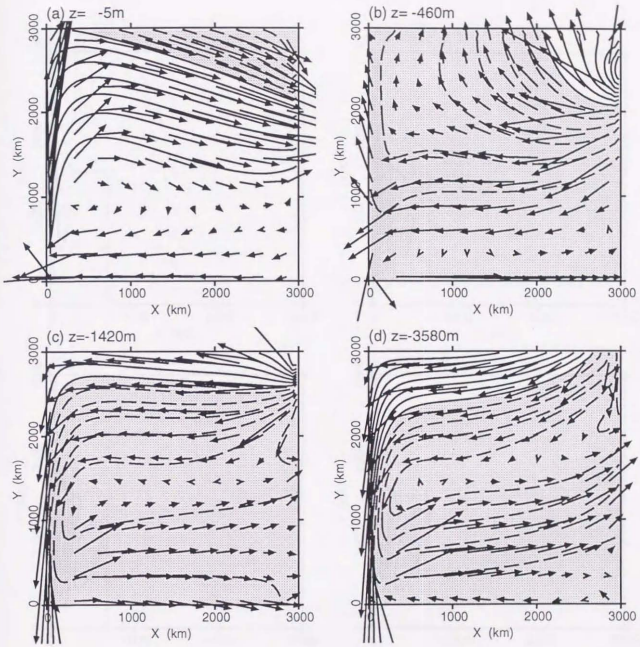

Fig. 4.26: The same as Fig. 4.19 except for the EB component. CIs are (a) 1.14×10^{3}dyn cm^{-2}, (b) 2.53×10^{2}dyn cm^{-2}, (c) 6.22×10^{1}dyn cm^{-2}, and (d) 3.73×10^{1}dyn cm^{-2}, respectively. VSs are (a) 7.08 cm s^{-1}, (b) 1.78 cm s^{-1}, (c) 5.64×10^{-1}cm s^{-1}, and (d) 4.76×10^{-1}cm s^{-1}, respectively.

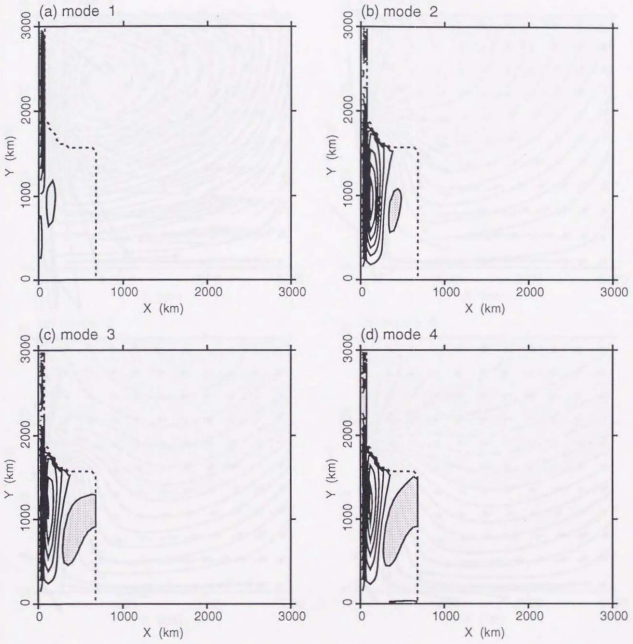

Fig. 4.27: The same as Fig. 4.21 except for the WB component. CIs are (a) 3.02×10^{-3}cm s^{-1}, (b) 1.49×10^{-3}cm s^{-1}, (c) 2.28×10^{-3}cm s^{-1}, and (d) 2.09×10^{-3}cm s^{-1}, respectively.

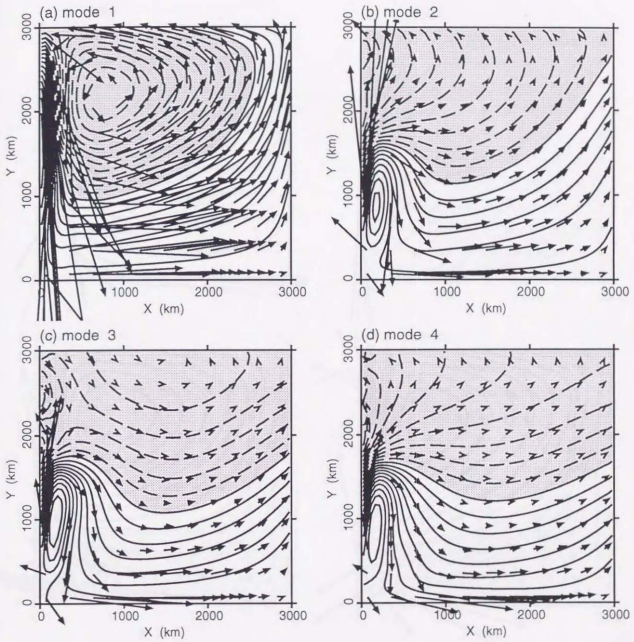

Fig. 4.28: The same as Fig. 4.18 except for the WB component. CIs are (a) 1.48×10^3cm, (b) 2.89×10^3cm, (c) 3.05×10^3cm, and (d) 3.64×10^3cm, respectively. For any mode, VS is 9.49×10^{-1}cm s^{-1}.

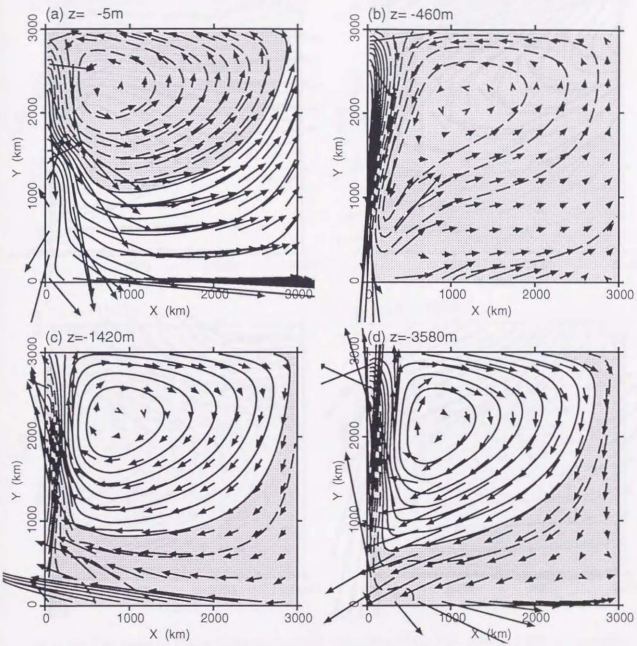

Fig. 4.29: The same as Fig. 4.19 except for the WB component. CIs are (a) 6.43×10^{2}dyn cm^{-2}, (b) 7.60×10^{1}dyn cm^{-2}, (c) 4.20×10^{1}dyn cm^{-2}, and (d) 4.27×10^{1}dyn cm^{-2}, respectively. VSs are (a) 8.76 cm s^{-1}, (b) 1.54 cm s^{-1}, (c) 1.07 cm s^{-1}, and (d) 6.28×10^{-1}cm s^{-1}, respectively.

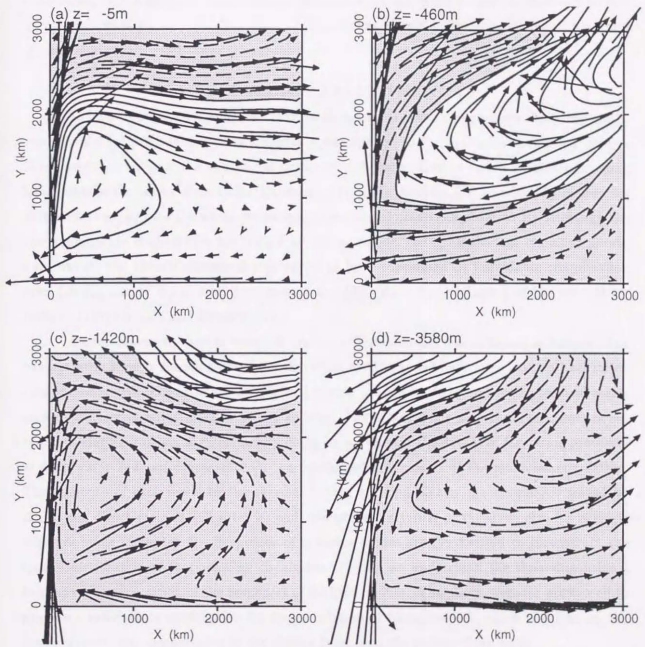

Fig. 4.30: The same as Fig. 4.19 except for the composite of the CA, NB, and EB components. The composite circulation well reproduces the MLM experimental results in Fig. 4.13. CIs are (a) 2.01×10^{3}dyn cm^{-2}, (b) 5.82×10^{2}dyn cm^{-2}, (c) 1.95×10^{2}dyn cm^{-2}, and (d) 2.83×10^{2}dyn cm^{-2}, respectively. VSs are (a) 1.97×10^{1}cm s^{-1}, (b) 2.69 cm s^{-1}, (c) 1.59 cm s^{-1}, and (d) 1.81 cm s^{-1}, respectively.

that the resulting circulation would be like that in the southern or southeastern part of the circulation of Experiment I, which stands for the thermohaline response to localized cooling. Comparing Figs. 4.13 with 4.2 and Figs. 4.14 with 4.9, we can confirm that the idealized picture above explains fairly well the circulation of Experiment II, which seems quite complicated at a glance.

4.5 SUMMARY AND DISCUSSION

To investigate the dynamics of the three-dimensional ocean general circulation, the multi-mode model (MMM) developed in Chapter 3 was applied to thermohaline circulation for two fundamental situations in a square flat ocean on a β-plane. One is driven by surface cooling localized near the center of the basin (Experiment I), while the other is maintained by meridional differential cooling over the whole sea surface as in the real ocean (Experiment II). Although the two experiments studied here are typical as well as simple, the dynamics has remained poorly understood; the three-dimensional structure has been considered of formidable complication even for the steady ocean free from mesoscale eddies since the beginning of the OGCM by Holland (1971) or Gill and Bryan (1971).

A comprehensive view in terms of vertical diffusive modes was obtained as follows. The basic stratification is specified first from the MLM results, which determines the vertical structure of modes. We then estimate the thermal forcing to each mode by converting residual terms such as convective adjustment or strong sinking. The MMM deals with these processes as external forcing that drives each mode. By doing so, we discard the details of formation processes of deep water and can concentrate on the fundamental dynamics of thermohaline circulation. The response of each mode to the thermal forcing (or equivalently mass input) is solved by use of the direct method (Chapter 3) and interpreted in terms of the dynamics for a single diffusive mode (Chapter 2). Responses of diffusive modes are synthesized to reconstruct the spatial distribution of thermohaline circulation. Finally we understand the three-dimensional field as the superposition of the responses of multiple modes. The above scenario works well to provide a satisfactory explanation for the circulation of Experiment I, which is driven by the convective cooling concentrated in the surface layer near the center of the basin.

Experiment II, however, shows a much more complicated circulation, for which simple decomposition into modes is of little use. Nevertheless it is possible to understand how the resulting circulation is maintained. We divided the strong thermal forcing into contributions from different regions of different physical processes: atmosphere-cooled convection in the northern basin, boundary-forced downwelling along the eastern boundary, and upwelling and downwelling along and near the western boundary. According to these principal regions of intense thermal forcing, principal *component circulations* were defined. The circulation in Experiment II is thus

interpreted as the composite of those component circulations. In turn, by virtue of the localization of forcing, each component circulation is interpreted well as the synthesis of multiple diffusive modes as in Experiment I. We can further consider the resulting circulation as the sum of the responses to point sources that are not localized but distributed wide. In an idealized picture of this view, the circulation in Experiment II roughly corresponds to the southern or southeastern part of the circulation of the Experiment I.

Thus a plain interpretation was obtained for the seemingly formidable structure of the three-dimensional thermohaline circulation at least for the cases examined here. We would like to emphasize that vertical modes provide a good perspective even to the three-dimensional structure of thermohaline circulation, which seems quite complicated and refusing simple interpretation if we rely upon only the usual description in the physical domain.

It is to be noted that the present MMM is not closed. First, the basic stratification must be specified or assumed as what is in the actual ocean or in numerical experiments. Besides, in order for the response to be calculated, the forcing must be provided to each vertical mode as data based on observation or experiment. This forcing is mainly due to convective formation of deep water or nonlinear advection of density. These processes are beyond the scope of the linearized MMM, so that the exact forcing to each mode must be determined from the circulation of numerical experiments. If only we admit them as the external data, however, the structure of the circulation becomes comprehensive, as has been emphasized so far; this paper is not aimed to explain the whole dynamical aspects of thermohaline circulation. In particular, we have put aside convective formation of deep water, which is supposed to occur in a confined region in the real ocean. It must be noted, however, that, even for the passive areas where no deep convection takes place, there has been no satisfactory explanation about the mechanism that maintains the spatial structure of thermohaline circulation beyond the theory of Stommel and Arons (1960), who also disregarded the details of deep-water formation.

For further understanding of thermohaline circulation, much remains to be studied. First, the multi-mode model is to be applied to more realistic cases that take into account wind stresses, rugged geographic boundaries, topographic effects, or multiple sources of deep water masses. Second, we should elucidate how purely external conditions determine the basic stratification, the forcing to each mode, the intensity or penetration depth of convective adjustment, and so on. For instance, It is crucial to clarify how deep the surface convection penetrates, depending on the basic stratification and on the strength of the surface cooling. Also detailed explanation must be awaited for the spatial structure of thermohaline circulation, because only a brief overview has been given to it in this paper, which intends to show the validity and usefulness of the multi-mode model. In addition, a nonmodal model is under investigation by which to study thermohaline structure more directly than diffusive modes. Though with limitations, such a model enables a

straightforward interpretation of various conspicuous features of thermohaline circulation which are presented but not fully analyzed in the present paper. For example, westward deepening of the surface of zero meridional velocity in Experiment I or the downwelling of warm water in the northeastern corner in Experiment II. In near future the same thermohaline circulation as here will be reexamined with respect to either its spatial structure or its thermodynamical forcing.

REFERENCES

Bryan, F. O., 1987: On the parameter sensitivity of primitive equation ocean general circulation models. *J. Phys. Oceanogr.*, **17**, 970–985.

Bryan, K., 1984: Acceralating the convergence to equilibrium of ocean-climate models. *J. Phys. Oceanogr.* , **14**, 664–673.

Cox, M. D., 1984: A primitive equation, 3-dimensional model of the ocean. GFDL Ocean Group Tech. Rep. No. 1, GFDL/Princeton University, 142pp.

Cox, M. D., and K. Bryan, 1984: A numerical model of the ventilated thermocline. *J. Phys. Oceanogr.*, **14**, 674–687.

Gill, A. E., and K. Bryan, 1971: Effects of geometry on the circulation of a three-dimensional southern-hemisphere ocean model. *Deep-Sea Res.*, **18**, 685–721.

Holland, W. R., 1971: Ocean tracer distributions. Part I. A preliminary numerical experiment. *Tellus*, **23**, 371–392.

Masuda, A., and G. Mizuta, 1995: A study on the effects of bottom topography on deep circulation with a diffusive reduced-gravity model. *J. Phys. Oceanogr.*, **25**, 374–390.

Semtner, A. J., Jr. and R. M. Chervin, 1992: General Circulation From a Global Eddy-Resolving Model. *J Geophys. Res.*, **97**(C), 5493–5550.

Stommel, H. and A. B. Arons, 1960: On the abyssal circulation of a world ocean—II. An idealized model of the circulation pattern and amplitude in oceanic basins. *Deep-Sea Res.*, **6**, 217–244.

Veronis, G., 1975: The role of models in tracer studies. In: Numerical Models of the Ocean Circulation, Natl. Acad. Sci., Washington, D. C., pp. 133–146.

Yoon, J.-H., 1991: The seasonal variation of the East Korean Warm Current. *Rep. Res. Inst. Appl. Mech., Kyushu Univ.*, **38**, 23–36.

Concluding remarks

The previous chapters from the second to fourth were written originally as articles for journals and the thesis places them in historical order of writing. Thus the chapters can conveniently be read independently from one another. Mutual relations among them, however, might have been less addressed. We therefore start with a short description of logical relations among the chapters. Then a summary is given to each chapter together with some concluding remarks for future research.

First let us abstract the role each chapter plays in the context of the thesis. As has been stressed so far in the thesis, three-dimensional nature of thermohaline circulation has long prevented oceanographers from understanding the dynamics of thermohaline circulation well. This difficulty is partly bypassed in the viewpoint of thermohaline circulation proposed in the thesis as the expansion in terms of diffusive vertical modes. The approach of the thesis therefore consists of the following four steps: (1) the field variables are expanded in terms of diffusive vertical modes to reduce the independent coordinates from three to two, (2) the response and the dynamics of a single mode is investigated thoroughly based on the notion of *diffusive* stretching, (3) the three-dimensional circulation is reproduced by the synthesis of the responses of many vertical modes, and finally (4) the three-dimensional structure of thermohaline circulation is interpreted as the superposition of vertical modes where the response of each mode has already been well understood.

The second step of the four is managed primarily by the second chapter, which clarifies the dynamics of abyssal circulation in particular. On the other hand, the third chapter not only formulates the above framework from the primitive equations of motion, but also prepares the direct method as an efficient solver for the response of a single mode. The contribution of the chapter therefore is to the first and third steps. Finally the fourth chapter applies the multi-mode model to two typical situations of purely thermohaline circulations, which are to be compared with those realized through a standard type of multi-level numerical experiments. Thus the chapter is devoted to the last step among others.

We now summarize the second to fourth chapters with an emphasis on their mutual relations.

Chapter 2

The second chapter introduces the *diffusive* reduced-gravity model, which takes into account both vertical and horizontal diffusion of density. The resulting governing equations are similar to those of the ordinary reduced-gravity model except that interfacial displacement has a term of Newtonian cooling and that of horizontal diffusion. A simple argument shows that this model represents the gravest baroclinic mode of thermohaline circulation. In other words, the diffusive reduced-gravity model is a single mode version of the multi-mode model discussed in the third chapter. By providing a clear interpretation of the behavior of a single mode, the second chapter makes one of the most important bases of the thesis, because the the multi-mode views thermohaline circulation as the synthesis of many vertical modes.

In this analysis of a single mode, horizontal diffusion and viscosity turn out to change the structure of boundary layers and the field of vertical velocity both on f- and β-planes. The dynamics of western boundary layers is classified into the viscous and diffusive regimes. In either regime, horizontal diffusion dominates the distribution of vertical velocity. Downwelling prevails in the western offshore boundary current flowing equatorward, while upwelling is always found in the poleward current. A more intense, opposite vertical motion occurs in a narrower boundary layer adjacent to the western coast. Downwelling is often distributed in a broad interior region, where horizontal diffusion again plays a crucial role in determining both horizontal and vertical velocities. The model explains this downwelling in terms of the diffusion of the thickness term in potential vorticity or the *diffusive* stretching. It is shown that, only when horizontal diffusion is incorporated, the diffusive reduced-gravity model is capable of reproducing the complicated distribution of vertical velocity in the abyssal layer which has often been referred to in various three-dimensional experiments. Also the diffusive reduced-gravity model is suggested to be applicable to the surface layer, extending the Sverdrup-Stommel-Munk theory of the homogeneous ocean to that more suitable for the stratified ocean.

Chapter 3

The diffusive reduced-gravity model has greatly advanced our understanding of the gross features of thermohaline circulation. However, that model represents only the gravest baroclinic mode. The vertical structure of circulation cannot be studied by a single mode, but must be investigated by the synthesis of many vertical modes. The third chapter is devoted therefore to the methodology of the thesis: systematic representation of the three-dimensional field of thermohaline circulation in terms of vertical diffusive modes. That is, the *diffusive* reduced-gravity model of the second chapter for the gravest baroclinic mode is generalized to a multi-mode

model that is composed of a number of diffusive vertical modes. First, the three-dimensional field of ocean general circulation is shown to be expanded in terms of diffusive vertical modes. Then, a direct method is developed to obtain the steady solution of each mode numerically. The direct method turned out accurate and efficient compared with the ordinary procedure to achieve the steady solution by time integration. As an example, that method is applied to the calculation of the thermohaline circulation in an ocean similar to the Pacific, which is driven by the inflow of deep water near the southwestern boundary in the Southern Hemisphere. The three-dimensional structure is obtained as a composite of the responses of diffusive vertical modes. It is shown that a seemingly slight change of vertical distribution of the inflow and outflow at the southwestern inlet may alter the vertical distribution of zonal current near the equator, where thermohaline circulation is rather sensitive to the amplitude of higher vertical modes.

Chapter 4

The fourth chapter combines the dynamics of a single mode argued in the second chapter with the synthesis of multiple modes formulated in the third chapter to study the three-dimensional structure of two examples of thermohaline circulations.

One is a circulation driven by surface cooling localized at the center of a northern basin. Around the cooled locations, a circular cyclonic circulation is induced in surface layers, whereas an anticyclonic circulation elongated westward and accompanied by eastern recirculation is produced in deep layers. It is shown that surface layers are dominated by the circulation pattern of higher modes whereas deep layers have that of lower modes. This circulation turns out almost the same as the response of a stratified ocean to body cooling due to convection concentrated near the center of the basin.

The other is a circulation driven by surface heating at low latitudes and cooling at high latitudes. In surface layers, a low is induced by deep convection near the northern boundary, whereas an anticyclonic circulation is observed in the southern region. Conversely, deep layers have a high in the northwestern part and exhibit a cyclonic circulation elsewhere. The circulation appears quite different from and much more involved than the circulation driven by the localized cooling in the first experiment. Nevertheless the circulation is understood well by resolving it into *component* circulations, each of which is driven by localized forcing so that it is explained as the synthesis of diffusive modes as well as in the first experiment. In particular, the MLM experiment is shown to agree with the MMM synthesis of the responses to distributed point sources or line sources of cooling near and along the northern boundary. Thus the circulation in the second experiment is compared to that in the southern or southeastern half of the first experiment.

In both cases, the multi-mode synthesis reproduces well the thermohaline circulation realized in the multi-level experiments, and the three-dimensional distribution is interpreted well if we consider it as the synthesis of the responses of diffusive vertical modes. The agreement itself is not surprising, since the stratification and the forcing in the multi-mode model are determined from the circulation of the multi-level model. What is to be emphasized is that the multi-mode model provides a plain perspective of the seemingly complicated three-dimensional structure of thermohaline circulation. For instance, curious distribution of downwelling in the abyssal layer is clearly explained in terms of the dynamics of diffusive modes. Also we understand how diffusive modes interfere to build up the three-dimensional structure of thermohaline circulation or how the extremely complicated structure of thermohaline circulation is resolved into simpler ones of component circulations.

As has been discussed in each final section of the chapters from the second to fourth, various problems remain to be studied further in future. Many of them are associated with the primary purpose of the thesis, which is intended to elucidate the fundamental dynamics in idealized models rather than to simulate details of the observed thermohaline circulation. We therefore have disregarded a lot of ingredients that are considered essential in order to represent the reality of the ocean: wind stress, unsteadiness, meso-scale eddies, coastal geography, topography, nonlinearity, adequate parameterization of subgrid scales, the nonlinear equation of state, different surface conditions for temperature and salinity, and so on. It is worthwhile to study further how these realistic though complicating factors modify or alter the dynamics of thermohaline circulation discussed in the thesis. In addition there are other fundamental problems raised or left unargued by the thesis. For instance, we need to get into the detailed process of deep water formation which has been dealt with simply as a black box in the thesis. Also it is desired to search for a non-modal approach that would explain the three-dimensional structure more directly.

Aside from those problems beyond its scope, the thesis has shown that the dynamics of thermohaline circulation becomes quite comprehensive from the viewpoint of the multi-mode model. Also the same framework as in the thesis has already been successfully applied to the study of the effect of topography on thermohaline circulation (Mizuta and Masuda 1995, private communication). The conceptual model presented here therefore, we believe, provides another sort of standard viewpoint through which to understand the dynamics of thermohaline circulation. Diffusive vertical modes and their synthesis give us at least a perspective that could not be obtained *only* by the multi-level description.

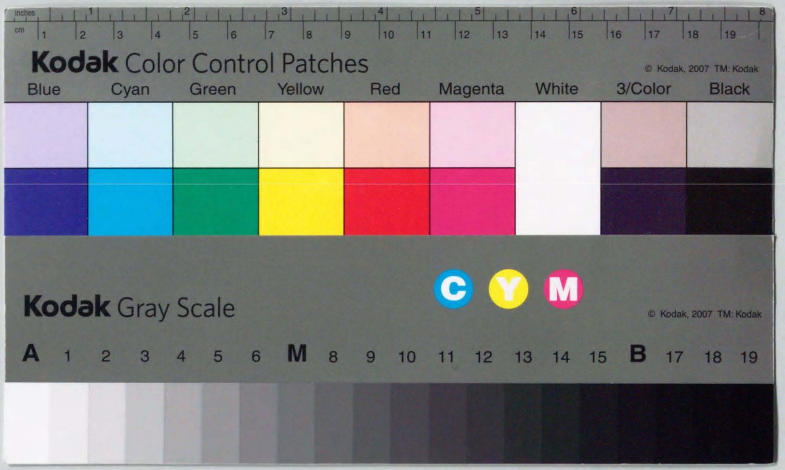
inches
cm
Kodak Color Control Patches
© Kodak, 2007 TM: Kodak
Blue
Cyan
Green
Yellow
Red
Magenta
White
3/Color
Black
Kodak Gray Scale
C
Y
M
© Kodak, 2007 TM: Kodak
A 1 2 3 4 5 6 M 8 9 10 11 12 13 14 15 B 17 18 19